2002

Prototype Micro Sensors for the Detection of Pesticide Residues on Blueberries

Guang Chen

Recommended Citation

Chen, Guang, "Prototype Micro Sensors for the Detection of Pesticide Residues on Blueberries" (2002). *Electronic Theses and Dissertations*. 269.
http://digitalcommons.library.umaine.edu/etd/269

PROTOTYPE MICRO SENSORS FOR THE DETECTION OF PESTICIDE RESIDUES ON BLUEBERRIES

By
Guang Chen
B.S. North China Electric Power University, China, 1988

A THESIS
Submitted in Partial Fulfillment of the
Requirements for the Degree of
Master of Science
(in Electrical Engineering)

The Graduate School
The University of Maine
August, 2002

Advisory Committee:

David Frankel, Senior Research Scientist, Sawyer Research Center, Advisor

John F. Vetelino, Professor of Electrical & Computer Engineering

Mauricio Pereira da Cunha, Assistant Professor of Electrical & Computer Engineering

Rodney J. Bushway, Professor of Food Science & Human Nutrition

PROTOTYPE MICRO SENSORS FOR THE DETECTION OF PESTICIDE RESIDUES ON BLUEBERRIES

By Guang Chen

Thesis Adviser: Dr. David Frankel

An Abstract of the Thesis Presented
in Partial Fulfillment of the Requirements for the
Degree of Master of Science
(in Electrical Engineering)
August 2002

The widespread use of pesticides on commercial food crops can result in short and long term health problems for both farm workers and consumers as well as serious impacts on the environment. Consequently, there is an increasing need to develop low cost portable detection systems that can be used to screen for pesticide residues on food products. Since phosmet ($C_{11}H_{12}NO_4PS_2$) is one of the most commonly used organophosphorous pesticides within the state of Maine, it is selected as the target pesticide to detect in this thesis.

Two sensing techniques were investigated. One is the quartz crystal microbalance (QCM), coated with a polyepichlorohydrin (PECH) film and expose to phosmet in a liquid solution. The second technique uses a chemiresistive sensor, with tungsten trioxide (WO_3) used as the sensing film.

The data obtained from the QCM experiments shows that the PECH coated QCM sensor displays good reproducibility to injections of phosmet solutions concentrations range up to 25 ppm phosmet in de-ionized water. The minimum detectable concentration of phosmet is 1ppm and the sensitivity of the PECH coated QCM is 15ρ2 Hz/ppm. The PECH coated QCM was also shown to detect phosmet in organic blueberry juice.

In order to determine the response of the WO_3 film to phosmet, a positive pressure gas delivery system was built. The resistance of the pure WO_3 film exposed to phosmet vapor in compressed air was measured from room temperature (25°C) to 400°C, while the temperature of phosmet solid was kept at 50°C. The resistance of various gold doped WO_3 film exposed to phosmet vapor in compressed air was also measured while the film temperature was kept at 350°C. The data obtained from SMO experiments shows that gold doped WO_3 films maintained at 350 °C are very sensitive to phosmet gas exposures in a carrier gas of air at 50% humidity. The concentration of phosmet gas within the gas delivery system is not known, but is estimated to be lower than 1ppb. The gold doped WO_3 film is poisoned by sulfur, a break down component of heated phosmet.

The gas chromatography/mass spectrometry (GC/MS) was used to determine the thermally induced break down products of phosmet and also to identify possible interferent molecules from crushed blueberries. The data shows that Phosphordithioic acid, ion 172, which is a main break down component of phosmet, can be used as an indicator to detect phosmet in treated blueberry samples.

The advantage of the polymer coated QCM sensor is that it can be used in both a gas and liquid environment, while the SMO sensor only can be used in a gas environment. Since the concentration of phosmet in liquid phase samples will be higher than when using gas phase detection, polymer coated QCM sensors have much more potential in phosmet detection.

ACKNOWLEDGEMENTS

I am grateful to my advisor Dr. David Frankel and Dr. John F.Vetelino, for providing me with the opportunity to continue my education at UMaine, and also for all of the time and energy they have expended with me during my graduate study. I wish to thank Dr. Chao Zhang for his help in the QCM experiment. At the same time, I also wish to thank my thesis committee members, Dr. Mauricio Pereira da Cunha and Dr. Rodney J. Bushway for all of their time and assistance with this thesis. I also would like to thank Dr. Brian G. Frederick and Dr. Carl Tripp for their help in understanding the chemical theory. Thanks also go to Dr. Brian Perkins, from Food Science Department for his work on the preparation of the blueberry samples, and Therese Anderson, from Environmental Chemistry Laboratory at UMaine for her help on the GC/MS. I also want to thank all the other faculty members in Electrical and Computer Engineering Department and members in the Laboratory of Surface Science and Technology who have given me help during my graduate study at UMaine. Finally I would like to thank my family, especially my wife, Huijuan, for her constant support and care, without which this thesis couldn't have been done. I also extend my thanks to all my friends for their encouragement and assistance.

TABLE OF CONTENTS

ACKNOWLEDGEMENTS..ii

LIST OF TABLES..vi

LIST OF FIGURES..vii

Chapter

1. INTRODUCTION 1

1.1 BACKGROUND... 1

1.2 PREVIOUS WROK 3

1.3 PURPOSE AND OBJECTIVES 7

1.4 ORGANIZATION.. 7

2. THEORY OF OPERATION OF QUARTZ CRYSTAL MICROBALANCE AND SEMICONDUCTING METAL OXIDE MICROSENSORS 9

2.1 QUARTZ CRYSTAL MICROBALANCE.. 9

2.1.1 The configuration of the QCM sensor 9

2.1.2 The Sauerbrey equation and Kanazawa expression.................... 10

2.1.3 The Butterworth-Van Dyke (BVD) electrical circuit 12

2.1.4 The modified Butterworth-Van Dyke (BVD) electrical circuit 16

2.1.5 The response mechanism between analytes and the polymer coating....... 26

2.2 SEMICONDUCTING METAL OXIDE SENSOR 29

2.2.1 The configuration of WO_3 thin film.. 29

2.2.2 Mechanism of interaction between the target gas and the SMO film........ 31

2.2.3 Mechanism of Au catalyst 36

3. EXPERIMENTAL SETUP 39

3.1 THE PHYSICAL AND CHEMICAL PROPERTIES OF THE TARGET PESTICIDE 39

3.2 EXPERIMENTAL SETUP, QCM MEASUREMENTS 40

3.2.1 Sample preparation 40

3.2.2 Coating preparation 42

3.2.3 Liquid phase QCM measurement system 42

3.2.4 Phase shift of quartz crystal in oscillating circuit 43

3.3 EXPERIMENTAL SETUP, SMO MEASUREMENTS 47

3.3.1 Gas delivery system 47

3.3.2 Data acquisition and temperature control system 49

3.4 EXPERIMENTAL SETUP, GC/MS AND PURGE & TRAP CONCENTRATOR 51

4. EXPERIMENTAL RESULTS 57

4.1 EXPERIMENTAL RESULTS BASED ON THE QCM SENSING TECHNIQUE 57

4.1.1 Water based experiments 57

4.1.2 Experiments using blueberry juice 68

4.2 EXPERIMENTAL RESULTS USING SMO SENSING TECHNIQUE 79

4.3 EXPERIMENTAL RESULTS BASED ON GC/MS AND PURGE & TRAP 90

5. SUMMARY, CONCLUSIONS AND FUTURE WORK 102

5.1 SUMMARY 102

5.2 CONCLUSIONS 105

5.3 FUTURE WORK 110

REFERENCES 115

APPENDIX A: DERIVATION OF SAUERBREY EQUATION (EQUATION 1) 121

APPENDIX B: DERIVATION OF KANAZAWA EXPRESSION (EQUATION 3) 124

APPENDIX C: DERIVATION OF THE EXPRESSIONS FOR THE CIRCUIT ELEMENTS OF THE MODIFIED BVD MODEL UNDER SIMULTANEOUS MASS AND LIQUID LOADING (EQUATION 7) 141

APPENDIX D: DERIVATION OF EQUATION C-40a, b 162

BIOGRAPHY OF THE AUTHOR 165

LIST OF TABLES

Table B1: Voigt indices definition 124

Table D1: Calculation result in equation (D-4) and (D-5) 163

LIST OF FIGURES

Figure 1: Configuration of the polymer coated QCM sensors

(a) Cross-section view (b) Top view 10

Figure 2: Shear displacement profiles across the QCM thickness for

the fundamental (N=1) and third (N=3) harmonic resonance 12

Figure 3: Butterworth-Van Dyke equivalent circuit for the unpertubed QCM 13

Figure 4: The admittance of the BVD model as a function of frequency based

on the values of the circuit components on page 14 16

Figure 5: Shear displacement profile and cross sectional view of a QCM

simultaneously loaded on one side by a surface mass layer and a

contacting Newtonian liquid 17

Figure 6: Equivalent circuit for a QCM under mass and liquid loading 19

Figure 7: Adsorption isotherms 28

Figure 8: WO_3 sensor structure 30

Figure 9: Band structure for an n-type metal oxide 32

Figure 10: The double layer near a metal oxide surface 33

Figure 11: An accumulation layer in an n-type metal oxide 33

Figure 12: Spillover model 37

Figure 13: New spillover model 38

Figure 14: Chemical structure of phosmet 40

Figure 15: Apparatus for the preparation of blueberry juice 41

Figure 16: The chemical structure of PECH 42

Figure 17: Frequency measuring system 43

Figure 18: The typical oscillating circuit used to drive a QCM 44

Figure 19: The new equivalent circuit model 46

Figure 20: Gas delivery system.. 48

Figure 21: Flow paths of the 6-way valve 49

Figure 22: Structure of the sample channel 49

Figure 23: Diagram of the data acquisition system 51

Figure 24: Gas chromatography.. 52

Figure 25: Mass spectrometry.. 53

Figure 26: Tekmar 3000 flow path 54

Figure 27: Resonant frequency of the bare QCM following a 50 μl of 3.2% phosmet injection to the water bath containing 66ml of water................. 58

Figure 28: Resonant frequency of the PECH coated QCM following a 50μl methanol injection to the water bath containing 66ml of water................ 58

Figure 29: Changes in resonant frequency of the PECH coated QCM following a series of phosmet injections to the water bath. 60

Figure 30: Net frequency shift as a function of phosmet injections from the data of figure 29... 60

Figure 31: Results of four sets of phosmet injections to the same sensor 62

Figure 32: Results of three series of phosmet injections using the same PECH coated QCM sensor... 62

Figure 33: Changes in resonant frequency of the PECH coated QCM following a series of phosmet injections to the water bath followed by flushing with distilled water 67

Figure 34: Net frequency shift of data from figure 33 as a function of phosmet concentration together with data from figure 31 67

Figure 35: Changes in resonant frequency of the PECH coated QCM following a series of phosmet injections to the organic blueberry juice 70

Figure 36: Net frequency shift as a function of phosmet concentration from the data of figure 35 71

Figure 37: Summary of experimental results of figure 33 and 35 72

Figure 38: Changes in resonant frequency of the PECH coated QCM following flushing with treated and organic blueberry juice 73

Figure 39: Changes in resonant frequency of the PECH coated QCM following a series of flushings with treated blueberry juice 75

Figure 40: Changes in resonant frequency of the bare QCM following a series of flushing with treated blueberry juice 76

Figure 41: Net frequency shift of bare and PECH coated QCMs following flushing with treated blueberry juice 77

Figure 42: Changes in resistance of WO_3 gold doped film following a series of phosmet gas exposures 80

Figure 43: Results from another gold doped WO_3 sensor under the same experimental parameters 80

Figure 44: Net resistance shifts as a function of the number of phosmet gas exposures data from figures 42 and 43 81

Figure 45: Results from poisoned gold doped WO_3 sensor in figure 42 under the same experimental parameters 82

Figure 46: Changes in resistance of a pure WO_3 film following a series of phosmet gas exposures at 200 °C 84

Figure 47: Changes in resistance of a pure WO_3 film following a series of phosmet gas exposures at 250 °C 84

Figure 48: Changes in resistance of a pure WO_3 film following a series of phosmet gas exposures at 300 °C 85

Figure 49: Changes in resistance of a pure WO_3 film following a series of phosmet gas exposures at 350 °C 85

Figure 50: Changes in resistance of a pure WO_3 film following a series of phosmet gas exposures at 400 °C 86

Figure 51: Sensitivity of the same pure WO_3 film versus film temperature 86

Figure 52: Auger spectrum from an untested gold doped WO_3 film 88

Figure 53: Auger spectrum from the gold doped WO_3 following tests shown in figure 42 88

Figure 54: Standard Auger spectrum of sulfur 89

Figure 55: GC/MS spectra from direct injection of a 100ppm phosmet solution 91

Figure 56: The standard mass spectrum of phosmet in the GC/MS database 92

Figure 57: Breakdown components of phosmet 93

Figure 58: GC/MS spectra from pure phosmet headspace at 25 °C 94

Figure 59: GC/MS spectra from pure phosmet headspace at 50 °C 95

Figure 60: GC/MS spectra from pure phosmet headspace at 75 °C 96

Figure 61: GC/MS spectra from pure phosmet headspace at 100 °C 97

Figure 62: Area of ion 172 peak as a function of temperature 99

Figure 63: GC/MS spectra from a headspace of 1ppm blueberry sample using purge & trap concentrator 100

Figure 64: GC/MS spectra from the headspace of an organic blueberry sample using purge & trap concentrator 101

Figure 65: Polymer structure for PECH, SXFA and P4V 112

Figure B1: Stress components acting on the surfaces of an infinitesimal cube........ 126

Figure B2: The coordinate system associated with the quartz disc and used in Appendices B and C 127

Figure B3: The unrotated and rotated coordinate systems........ 129

1 INTRODUCTION

1.1 Background

According to federal law, "...a pesticide is any substance or mixture of substances intended for preventing, destroying, repelling or mitigating any pest. Pesticide is an umbrella term for many types of products, such as insecticides, herbicides, fungicides, rodenticides, nematicides, etc. Pesticides may be natural or man-made." [1]. Organophosphorous pesticides, classified by their chemical structures, are one of the major categories of pesticides. They are widely used on commercial food crops such as blueberries because they have relatively low environmental toxicity and a rapid degradation rate [2]. Organophosphorous pesticides interfere with the impulse transmission between nerve endings when they enter the central nervous system of insects [3]. At the molecular level, the action of the enzyme acetyl cholinesterase is inhibited by the pesticides. This enzyme is very important for the nervous system because it controls the hydrolysis of acetylcholine generated at nerve junctions into choline. In the absence of active acetyl cholinesterase, the extra acetylcholine will accumulate and prevent the smooth transmission of nervous impulses across the synaptic gap at the nerve junction. This can then result in a loss of muscular coordination, convulsions and ultimately death. Since acetyl cholinesterase is an essential enzyme of the nervous system of both pests and mammals, organophosphorous compounds are also toxic to mammals [4].

Organophosphorous pesticides have been widely used to control pests in the agriculture industry for many years. In the case of blueberries, the blueberry fruit fly lays eggs inside the berry [5]. The larvae hatch and consume the contents of the berry. Some of the infested berries are harvested and shipped, although the majority of the contaminated fruit drops to ground. The larvae hatch and flies overwhelm the rest of the shipment during the traveling of fruit from the field to the market [6]. Stringent limits are set up by the government for the number of maggots per jar of canned blueberries. Therefore the farmers' response is to use pesticide, specifically organophosphorous pesticides.

Since organophosphorous pesticides can enter the food chain especially under prolonged or repeated exposure. There can be ill effects to consumers if they consume large quantities of blueberries that have been treated with a pesticide. Side effects of organophosphorous pesticides used on blueberries include cramps, diarrhea, labored breathing, nausea and in extreme cases unconsciousness, vomiting and blurred vision [7]. This issue becomes worse with respect to children because organophosphates have the potential to interfere with their development [8]. This is alarming because children are generally encouraged to consume high quantities of fruits, and vegetables for their nutritional value and are thus put at high risk of exposure. Adults could screen fruits and vegetables before consuming them or giving them to their children if they had a pesticide detector.

Generally, farmers also want to reduce the usage of organophosphorous pesticides. One reason is the toxicity of pesticide use to bees. Because bees provide the means for pollination, they are important tools to farmers. A portable sensor would allow farmers to measure and regulate the concentration level of use and thus reduce pesticide exposure to bees.

Organic product has become attractive in part because of the adverse side effects of pesticides. The "organic" label means that the product was grown without the aid of pesticides. With the increasing knowledge of the adverse side effects, food grown without exposure to any type of pesticide is regarded as a more attractive choice for the American public. Because of its higher production costs, "organic" food is priced 1.5 to 2 times higher than "non organic" food. A sensor could help prevent fraud in this expanding industry. It could also be used to screen food imported from other countries where pesticide laws are limited and less strictly enforced [65].

The above reasons, clearly identify a strong need to develop low cost portable methods of detecting pesticide residues on food products.

1.2 Previous Work

The detection of organophosphorous pesticides at the concentrations at which they occur in the environment demands analytical methods that are very sensitive and accurate. Traditional methods of detecting these compounds have used laboratory-based techniques such as high performance liquid chromatography (HPLC), gas chromatography (GC), mass spectrometry (MS) and combinations of these methods (GC/MS, HPLC/MS) [9-11]. Generally these methods are complicated due to the need for sample preprocessing prior to sample injection into the analytical instruments and the high degree of expertise required for instrument operation and data interpretation.

There have been only limited reports of rapid and relatively inexpensive sensing methods to detect organophosphorous pesticides. In the 1970s, Guilbault and coworkers [12] used bulk acoustic wave sensors coated with inorganic films of $FeCl_3$, $CuCl_2$, $NiCl_2$ and $CdCl_2$ to detect diisopropyl methylphosphonate (DIMP) in the gas phase. After optimization of the above coatings, the sensitivity of the most sensitive coating, $Fe(DIMP)_xCl_3$, was below 10ppm. DIMP was used as a model for organophosphorous pesticides. While DIMP has a relatively high vapor pressure that lends itself to gas phase detection, other organophosphorous pesticides have very low room temperature vapor pressures making gas phase detection difficult. Since the response of a $Fe(DIMP)_xCl_3$ coated sensor to a real pesticide, paraoxon, was extremely small, they used a $FeCl_3$-paraoxon complex coated QCM (Quartz Crystal Microbalance) to detect paraoxon. The sensitivity was not as good as for DIMP, but still could reach 50Hz/10ppm. Guilbault and his coworkers [13] did further work to try to increase the sensitivity and selectivity of the QCM sensor to DIMP through optimizing the coatings. In 1981, they used a ternary mixture of Triton X-100, NaOH and 1-n-dodecy-3-hydroximinomethylpyridinium iodide (3-PAD) as the coating and the DIMP sensitivity was increased to 612Hz/15ppm. This coating showed good selectivity to various interferences, which included ammonia, carbon monoxide, benzene, toluene ethyl alcohol, chloroform and sulfur dioxide. In 1985, they found two other coatings, PVP (poly vinylpyrrolidone)-TMEDA (teramethylethylenediamine) and PVBC (poly vinylbenzyl chloride)-TMEDA, which were also sensitive to DIMP in the ppb concentration range [14]. Compared to the previously described coatings, these coatings had higher sensitivity and faster response times (minutes for the PVP-TEMDA coating and seconds for the PVBC-TEMDA coating).

In general, there are two kinds of biosensors that have been used to detect organophosphorous pesticides; 1) Sensors based on the immunoassay technique and 2) sensors using the immobilized enzyme probe (IEP) technique. The mechanism of immunoassays is based on the interaction between the antigen (Ag) in question and its specific binding partner or antibody (Ab) to form an antibody/antigen (Ab/Ag) complex. Therefore for a certain concentration of Ab, the ratio of bound to free Ag is quantitatively related to the total amount of Ag present after the equilibrium of the assay is reached. Either an Ag or Ab can be labeled by agents, such as fluorescent probes, chemiluminescent probes and radioisotopes. Thus, if a certain amount of labeled Ag is introduced into the assay, the concentration of the unknown Ag can then be determined by comparing the measurements of Ab/ known concentration Ag and Ab/ unknown concentration Ag.

The IEP technique is based on the fact that organophosphorous pesticides act by interfering with enzymes. As mentioned before, organophosphorous pesticides are inhibitors of the enzyme acetyl cholinesterase, which plays an important role in the transmission of nerve impulses. In the IEP technique, the substrate, which contains acetylcholine, will be hydrolyzed by cholinesterase (enzyme) immobilized on a transducer. The hydrolyzing process can generate acid, which results in a decrease of PH of the substrate and indicates the enzymatic activities of the immobilized acetyl cholinesterase. Therefore the immobilization of the enzyme acetyl cholinesterase on a selected transducer can be used to detect pesticide residues due to the enzyme inhibition. The inhibition level, which can be obtained by the measuring pH of the substrate before and after pesticides exposure, is related to the pesticide concentration in solution.

In 1986, the immunoassay technique was used to detect parathion in the gas phase by Guilbault and his coworkers [15]. Parathion in the gas phase was detected by a 9 MHz piezoelectric quartz crystal coated with antibodies against parathion. The carrier gas was bubbled through the parathion solution to get saturated parathion gas. Various concentrations of parathion gas were obtained by changing the flow rate of a carrier gas, which was combined with the saturated parathion gas. The sensitivity of this sensor was 11Hz/ppb.

In 1990, Wlodarski and coworkers [16] presented a biosensor based on a IEP technique to detect organophosphorous pesticides (Parathion, Dichlorvos) in the liquid phase. They used butyryl cholinesterase (enzyme), glutaraldehyde and bovine serum albumin to prepare the immobilized enzyme membrane and fixed this membrane on the gate of pH-ion sensitive field effect transistor (ISFET) by a nylon net. The substrate butyryl choline diffused into the immobilized enzyme layer and was hydrolyzed by cholinesterase to produce butyric acid, and then the pH of the buffered substrate solution was decreased. The decrease of pH on the surface of the ISFET represented the enzymatic activity of immobilized cholinesterase when the enzyme coated ISFET was inserted in a certain concentration of buffered substrate solution. The concentration of pesticide solution was determined by the change of enzymatic activities before and after exposure to the enzyme inhibitor, which was the organophosphorous pesticide. The sensitivity of this sensor can reach the ppb level.

1.3 Purpose and Objectives

The purpose of this thesis is to develop a prototype sensor to detect pesticide residues on blueberries. The ultimate objective will be a reusable and portable sensor for the real-time testing of pesticide residues on blueberries. Since phosmet ($C_{11}H_{12}NO_4PS_2$) is one of the most commonly used organophosphorous pesticides within the state of Maine, it was selected as the target pesticide of this thesis.

Two existing sensing techniques used in the Laboratory of Surface Science and Technology (LASST) were investigated. One technique uses a polymer coated quartz crystal microbalance (QCM), where the polymer film used was polyepichlorohydrin (PECH) and the other is a chemiresistive semiconductor metal oxide (SMO) sensor, with WO_3 used as the sensing film. The polymer coated QCM sensing technique is based on the relationship between the resonant frequency shift of the QCM and the mass loading and liquid loading phenomena. A frequency measuring system was built to perform the phosmet detection experiment in the liquid phase. The SMO sensing technique is based on the change of carrier density, which is caused by the interactions between the analyte and SMO film. In order to determine the response between the WO_3 film and phosmet, a positive pressure gas delivery system was built and the resistance of the WO_3 film was measured in compressed air from room temperature (25°C) to 400°C.

1.4 Organization

This thesis is organized into 5 chapters, the first of which is the Introduction. The second chapter describes the operation of the QCM and SMO sensors. This chapter then proceeds to describe the mechanisms of how the frequency of the QCM changed with the phosmet concentration in solution, and how the conductivity of the WO_3 film was changed when phosmet was introduced..

Chapter 3 describes the experimental setups used. It includes a discussion of the frequency measuring system and the water bath for the QCM sensor, the positive pressure gas delivery system and the temperature control system for the SMO sensor. The experimental setup of the GC/MS and Purge & Trap is also presented in this chapter.

Chapter 4 presents the experimental data obtained by monitoring the frequency shift of the PECH coated QCM and the DC conductivity of the WO_3 film. The PECH coated QCM was exposed to various concentrations of phosmet solution. The frequency shift of the PECH coated QCM due to the mass loading and liquid loading of various concentrations of phosmet solution is discussed. The SMO sensors were operated at various film temperatures. The different responses between the phosmet gas and a gold-doped WO_3 film and an undoped WO_3 film are discussed. Chromatogram and mass spectra of phosmet in the liquid phase and from gas phase headspace sampling at different temperatures were obtained. The chromatograms and mass spectra of phosmet residues on blueberries are presented in this chapter also.

Chapter 5 presents a summary of the work, conclusions about the SMO/QCM microsensor and directions relating to future work.

The appendices are reserved for the derivation of the Sauerbrey and Kanazawa equations, and the development of the expressions for the circuit elements of the modified Butterworth-Van Dyke (BVD) model.

2 THEORY OF QUARTZ CRYSTAL MICROBALANCE AND SEMICONDUCTING METAL OXIDE MICROSENSORS

This chapter presents the configuration and the theory of the polymer coated quartz crystal microbalance (QCM) sensor and the WO_3 thin film sensor. In the first part, the Sauerbrey equation and the modified Butterworth-Van Dyke (BVD) electrical circuit is presented to explain the mass and liquid loading behavior of the QCM. The mechanism between the target analyte and the polymer is also discussed. The second part includes the mechanism of the interactions between the target gas and the semiconductor film, and also the role Au plays as a catalyst during chemisorption.

2.1 Quartz Crystal Microbalance

2.1.1 The configuration of the QCM sensor

The QCM sensor shown in figure 1 used a 5-MHz, AT-cut quartz crystal. Referring to the top view, the sensor consists of a quartz disk and a gold sensing electrode (dark area), which is much thinner than quartz disk, on the top and a reference electrode (dashed line) on the bottom. The tab of the sensing electrode goes around the edge of the crystal to the reference side so that both electrodes can be contacted on the reference side. A selective thin polymer film was coated on the top electrode of the quartz crystal as shown in the cross-sectional view. The electric field generated by applying an AC voltage across the electrodes excites a horizontally polarized shear wave in the quartz disk. The quartz crystal resonates at a frequency determined by the crystal thickness and the type of mode that is excited. When the bare quartz crystal is loaded with a thin film, the resonant frequency change is proportional to the mass of the thin film. In figure 1, only the polymer coated sensing electrode is in contact with a viscous liquid. As the thin film absorbs a target analyte within the liquid, the resonant frequency change is directly proportional to the mass of the absorbed analyte. The detailed description of QCM measurement system is presented in 3.2.3.

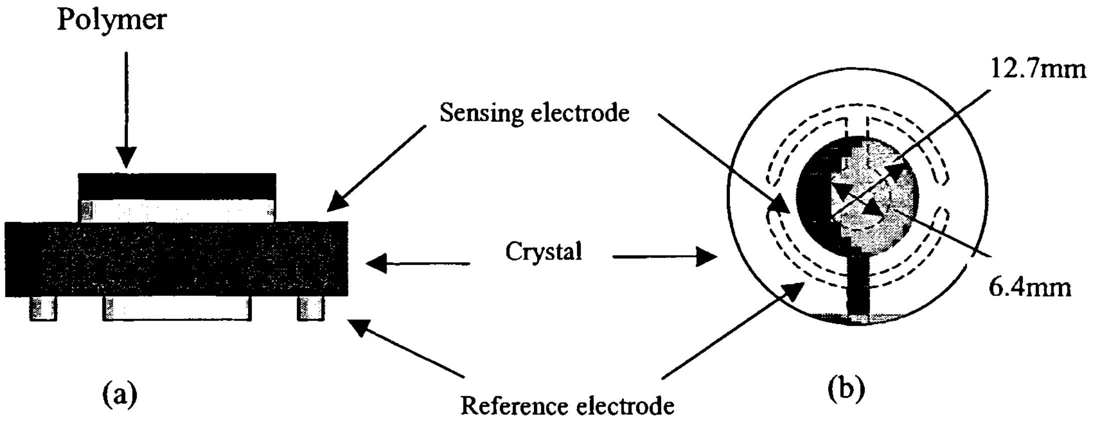

Figure 1: Configuration of the polymer coated QCM sensors. a) Cross-section view, b) Top view.

2.1.2 The Sauerbrey equation and Kanazawa expression

Sauerbrey first indicated the possibility of using a piezoelectric quartz resonator as a quantitative mass-measuring device [17]. The decrease of the resonant frequency, Δf, of a thickness shear vibrating quartz crystal, having either an AT or BT cut, was found to be proportional to the added mass of the deposited film [18],

$$\Delta f = -\frac{f_q^2}{N \cdot \rho_q \cdot S} M_f = -K_m M_f , \tag{1}$$

where f_q is the fundamental resonance frequency of the quartz crystal, N is the frequency constant of the specific crystal cut (N_{AT}=167 KHz cm, N_{BT}=250 KHz cm), ρ_q is the quartz density(ρ_q=2.648 g cm^{-3}), S is the surface area of the deposited film which is equal to the surface sensing area of the quartz crystal, and M_f is the mass of the deposited film. For a 5MHz AT-cut quartz crystal, the mass sensitivity constant, K_m, can be calculated as $56.5 Hz / \mu g$. Another form of the Sauerbrey equation can be expressed as

$$\frac{\Delta f}{f_q} = -\frac{M_f}{M_q}, \tag{2}$$

where M_q is the mass of the vibrating quartz crystal. The detailed derivation of equations (1) and (2) is given in appendix A.

Beginning in 1980 attention was focused not only on solid deposits on the surface of shear vibrating quartz crystal resonators, but also on operations in liquids. Kanazawa and Gordon [19,20] theoretically showed that the resonant frequency shift caused by immersing the sensing face of a quartz crystal in a viscous fluid is a function of the material parameters of the fluid and quartz. They presented a physical model that treats the quartz as an elastic solid and the liquid as a purely viscous fluid. The frequency shift is derived by assuming that the shear wave in the quartz is coupled with a damped shear wave in the liquid. After applying specific boundary conditions, the following relationship for the measured frequency change was obtained,

$$\Delta f = -f_q^{3/2}\left(\rho\eta/\pi\rho_q\mu_q\right)^{1/2}, \qquad (3)$$

where ρ and η are the density and viscosity of the liquid, μ_q is the stiffened shear modulus of quartz and defined as $\mu_q = \overline{C_{66}} = C_{66} + e_{26}^2 / \varepsilon_{22}$, C_{66}, e_{26} and ε_{22} are the shear elastic, piezoelectric and permittivity constants of the quartz crystal respectively. For the AT cut in quartz μ_q ==2.947x10^{11} dyne cm^{-2}. The detailed derivation of equation (3) is presented in appendix B.

2.1.3 The Butterworth-Van Dyke (BVD) electrical circuit

The crystal is electrically excited into resonance by applying a voltage across the electrodes of a crystal disk at an excitation frequency such that the crystal thickness is an odd multiple of a half of an acoustic wavelength. At these frequencies, a standing shear wave is formed between the two surfaces of the crystal disk [21]. Figure 2 shows the fundamental and third harmonic resonances.

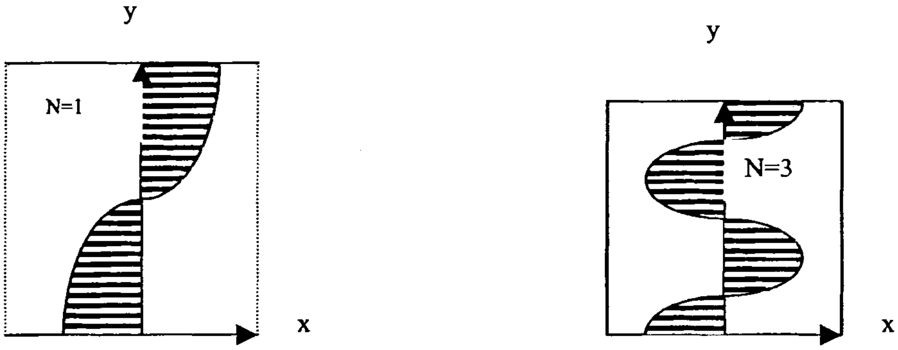

Figure 2: Shear displacement profiles across the QCM thickness for the fundamental (N=1) and third (N=3) harmonic resonance.

Butterworth and coworkers [22] indicated that an equivalent circuit model could represent a mechanically vibrating device such as the unpertubed (without any loading) QCM driven by an AC voltage. Figure 3 shows this model, which is also called the Butterworth-Van Dyke (BVD) model. C_0 is the electrostatic capacitance between the two parallel electrodes in the quartz crystal. The electromechanical coupling caused by the piezoelectric property forms the motional arm (L_1, C_1, R_1) in the BVD model. L_1 represents the motional inductance, which is a measure of the inertia of the oscillating system. C_1 represents the motional capacitance, which is related to the elasticity or energy stored in the crystal. R_1 represents the motional resistance and is a measure of the internal energy dissipation in the crystal. The circuit components, C_0, L_1, C_1, R_1, have explicit expressions in terms of the material properties of the quartz crystal. The detailed derivation of the expressions for C_0, L_1, C_1, R_1, are given in appendix C.

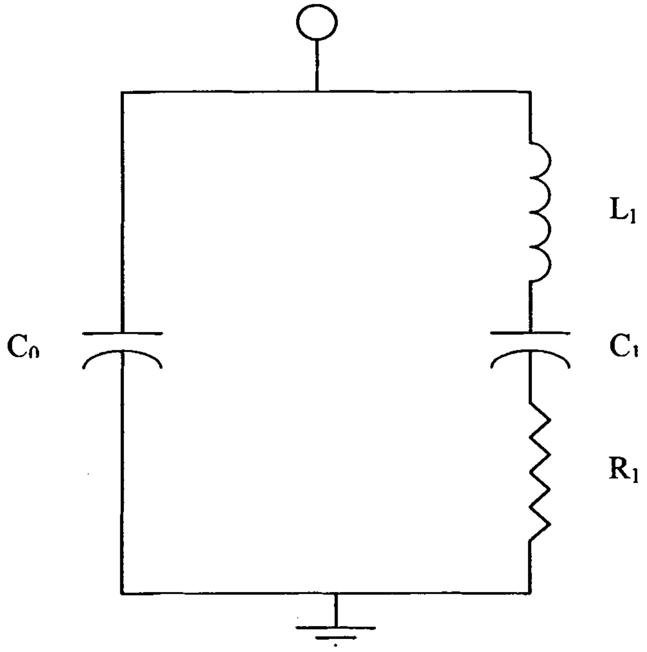

Figure 3: Butterworth-Van Dyke equivalent circuit for the unpertubed QCM.

The impedance of the motional arm in figure 3 is,

$$Z_m = R_1 + j\omega L_1 + \frac{1}{j\omega C_1} = \sqrt{R_1^2 + \left(\omega L_1 - \frac{1}{\omega C_1}\right)^2} \angle \tan^{-1}\frac{\omega L_1 - \frac{1}{\omega C_1}}{R_1}, \tag{4}$$

The frequency normally used to quantify the sensitivity of the QCM sensor is the series resonant frequency, which is usually defined as the frequency of the minimum impedance of the resonator or the frequency at zero phase. From equation (4) this occurs when,

$$f_s = \frac{\omega_s}{2\pi} = {}^{1}\!\big/_{2\pi\sqrt{L_1C_1}}, \tag{5}$$

The admittance of the BVD model in figure 3 is,

$$Y = j\omega C_0 + \frac{1}{Z_m} = \frac{R_1}{R_1^2 + \left(\omega L_1 - \frac{1}{\omega C_1}\right)^2} + j\left(\omega C_0 - \frac{\omega L_1 - \frac{1}{\omega C_1}}{R_1^2 + \left(\omega L_1 - \frac{1}{\omega C_1}\right)^2}\right), \tag{6}$$

When the bare QCM operates near the series resonant frequency, $\omega \approx \omega_s = \frac{1}{\sqrt{L_1C_1}}$, equation (6) can be simplified as,

$$Y \approx \frac{1}{R_1} + j\omega C_0 = \frac{1}{R_1} + j\frac{C_0}{\sqrt{L_1C_1}}. \tag{6a}$$

Martin [22] obtained the values of circuit components, $R_1 = 55.3\,\Omega$, $C_0 = 4.3pF$, $C_1 = 26.9fF$ and $L_1 = 37.92mH$ for the typical unperturbed 5MHz QCM by fitting the BVD model to the unperturbed QCM admittance versus frequency data measured near resonance. The real part of equation (6a), $\frac{1}{R_1} = 0.018$, is much larger than the imaginary part, $\frac{C_0}{\sqrt{L_1 C_1}} = 1.346 \cdot 10^{-4}$, therefore, equation (6a) reduces to,

$$Y \approx \frac{1}{R_1}. \tag{6b}$$

When the bare QCM operates away from series resonant frequency, ω_s, therefore $\omega \; \pi\pi \; \omega_s$ or $\omega \; \phi\phi \; \omega_s$, the term $\omega L_1 - \frac{1}{\omega C_1}$ becomes larger compared to the value of R_1^2. Therefore, the real part of equation (6) and the second term in the imaginary part go to zero. Equation (6) then reduces to,

$$Y \approx j\omega C_0 \tag{6c}$$

Equation (6b) and (6c) indicate that while the motional resistance contribution dominates near resonance, the electrostatic capacitance dominates the admittance away from resonance.

Using the circuit element values reported by Martin[22], figure 4 shows the magnitude and phase of the admittance of the BVD model as a function of frequency. At the series resonant frequency f_s, the magnitude of admittance is the maximum and the phase is zero. At the parallel resonant frequency f_p, the magnitude of admittance is the minimum and the phase is zero. Since the resonant frequency of QCM is determined by the crystal thickness (see equation A-2 in appendix A), the manufacturing tolerance of the crystal thickness causes the series resonant frequency to be slightly different than 5MHz.

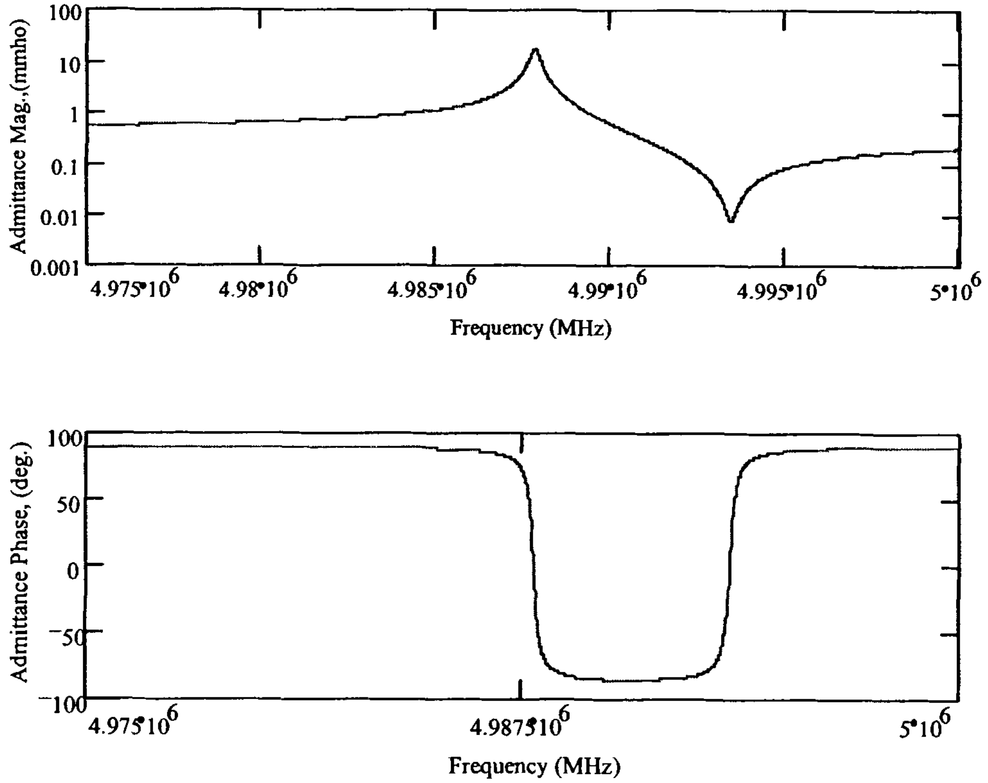

Figure 4: The admittance of the BVD model as a function of frequency based on the values of the circuit components on page 14.

(a) The magnitude of the admittance vs. frequency

(b) The phase of the admittance vs. frequency

2.1.4 The modified Butterworth-Van Dyke (BVD) electrical circuit

When a QCM operates in a liquid, its resonant frequency will be decreased by the effect of both mass and liquid loading. Figure 5 shows the cross sectional geometry of the QCM operating in a viscous fluid, which results in both mass and liquid loading on the upper sensing surface. Figure 5 also illustrates that a damped shear wave is propagated into the viscous liquid when the QCM is excited into resonance. The liquid can be considered semi-infinite if the liquid thickness is large compared to the decay length of the propagated shear wave. Excitation electrodes, which are located on both sides of the quartz crystal, are assumed to be very thin compared to the crystal thickness. The loaded mass layer is also assumed to be very thin compared to the acoustic wavelength and rigidly attached to the QCM in order to ensure that it will vibrate synchronously with the quartz crystal.

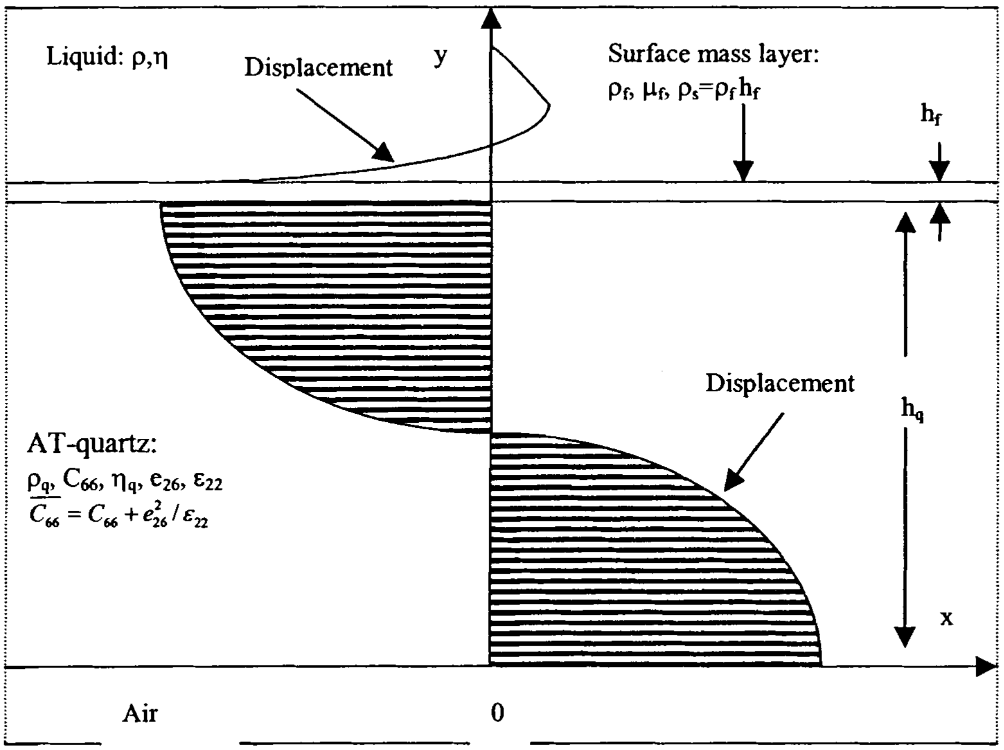

Figure 5: Shear displacement profile and cross sectional view of a QCM simultaneously loaded on one side by a surface mass layer and a contacting Newtonian liquid.

In figure 5, ρ and η are the liquid mass density and shear viscosity, ρ_f and μ_f represent the mass density and shear stiffness of the surface mass layer, $\rho_s = \rho_f h_f$ is the surface mass density of the surface mass layer, ρ_q and η_q represent the quartz mass density and effective quartz viscosity. Since the quartz crystal is AT cut and the wave propagating in the liquid is a shear wave, only C_{66}, e_{26} and ε_{22}, which are the quartz elastic, piezoelectric and permittivity constants respectively are related to the shear wave, and $\overline{C_{66}} = C_{66} + e_{26}^2 / \varepsilon_{22}$ is the piezoelectrically stiffened quartz elastic constant. As discussed in more detail in appendix C, when the losses in the quartz are considered, the piezoelectrically stiffened quartz elastic constant, $\overline{C_{66}}$ becomes a complex and may be written as, $\overline{\overline{C_{66}}} = \overline{C_{66}}(1 + j\xi)$, where ξ is defined as the quartz loss parameter and given as $\xi = \dfrac{\omega\eta_q}{\overline{C_{66}}}$.

Martin and coworkers [22] presented a modified BVD equivalent circuit model that describes the QCM simultaneously loaded by a thin surface mass layer and a semi-infinite Newtonian liquid. The definition of a Newtonian liquid is given in appendix B. Figure 6 shows this model and the circuit elements, which can be used to represent the mass and liquid loaded QCM, respectively.

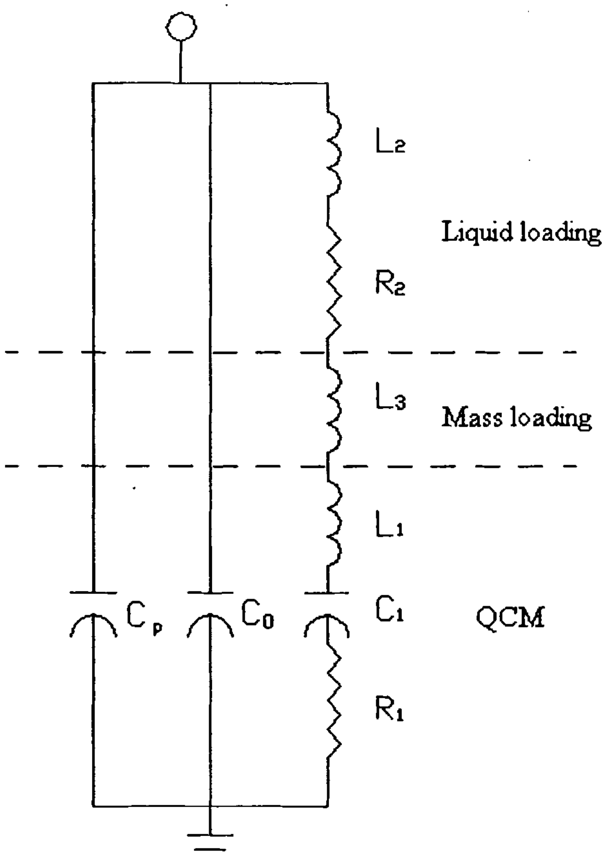

Figure 6: Equivalent circuit for a QCM under mass and liquid loading.

In figure 6, Cp is the parasitic capacitance of the test fixture, R_2 and L_2 are the resistance and inductance associated with the liquid loading and L_3 is associated with the mass loading.

Martin explicitly related the circuit elements of the modified BVD model to the physical properties of the QCM and the perturbing mass and liquid as follows,

$$C_0 = \frac{\varepsilon_{22} S}{h_q}, \tag{7a}$$

$$C_1 = \frac{8K_0^2 C_0}{(n\pi)^2}, \tag{7b}$$

$$L_1 = \frac{1}{\omega_s^2 C_1}, \tag{7c}$$

$$R_1 = \frac{\eta_q}{\bar{C}_{66} C_1}\left(\frac{\omega}{\omega_s}\right)^2, \tag{7d}$$

$$L_2 = \frac{\omega_s L_1}{n\pi}\left(\frac{2\rho\eta}{\omega \bar{\bar{C}}_{66}\rho_q}\right)^{1/2}, \tag{7e}$$

$$R_2 = \frac{\omega_s L_1}{n\pi}\left(\frac{2\omega\rho\eta}{\bar{C}_{66}\rho_q}\right)^{1/2} \tag{7f}$$

and

$$L_3 = \frac{2\omega_s L_1 \rho_s}{n\pi\sqrt{\bar{\bar{C}}_{66}\rho_q}}, \tag{7g}$$

where ω_s is defined in equation (5), $K_0^2 = e_{26}^2 \big/ \left(\bar{C}_{66}\varepsilon_{22}\right)$ is the electromechanical coupling constant of the QCM and n is the harmonic number ($n = 1,3,5\ldots$). The detailed derivation of equation (7a-7g) is given in appendix C.

For the bare QCM, ρ_s, ρ and η are zero, hence $L_2 = R_2 = L_3 = 0$, and figure 6 reduces to the BVD equivalent circuit for the unloaded QCM, shown in figure 3. The change in resonant frequency with mass and liquid loading can be derived from the modified BVD equivalent circuit model. Following the expression for the series resonant frequency given in equation (5), the new series resonant frequency after mass and liquid loading are included becomes $f_s^* = 1/\left(2\pi(LC_1)^{1/2}\right)$, where $L = L_1 + \Delta L = L_1 + L_2 + L_3$ and C_1 is unchanged by mass or liquid loading. The change in f_s can be expressed as follows,

$$\begin{aligned}\Delta f_s &= f_s^* - f_s = \frac{1}{2\pi\sqrt{C_1}}\left(\sqrt{\frac{1}{L_1 + \Delta L}} - \sqrt{\frac{1}{L_1}}\right) = \frac{1}{2\pi\sqrt{C_1 L_1}}\left(\sqrt{\frac{L_1}{L_1 + \Delta L}} - 1\right) \\ &= f_s\left(\sqrt{\frac{L_1}{L_1 + \Delta L}} - 1\right),\end{aligned} \tag{8}$$

Applying a Taylor expansion on Δf_s about $\Delta L = 0$ and neglecting the second and higher order terms, one obtains,

$$\begin{aligned}\Delta f_s &= f_s\left(\sqrt{\frac{L_1}{L_1 + \Delta L}} - 1\right) \approx \Delta f_s\big|_{\Delta L=0} + \frac{d\Delta f_s}{d\Delta L}\Big|_{\Delta L=0}(\Delta L - 0) \\ &= f_s\left(\frac{1}{2}\right)\left(\frac{L_1}{L_1 + \Delta L}\right)^{-\frac{1}{2}} \frac{-L_1}{(L_1 + \Delta L)^2}\Big|_{\Delta L=0}\Delta L = -\frac{f_s}{2}\frac{L_2 + L_3}{L_1}.\end{aligned} \tag{9}$$

substituting equations (7) into equation (9) and noting that $\omega = \omega_s$, results in the following expression for the change in resonant frequency,

$$\Delta f_s \approx -\frac{2f_s^2}{n\sqrt{C_{66}\rho_q}}\left[\rho_s + \left(\frac{\rho\eta}{4\pi f_s}\right)^{1/2}\right]. \tag{10}$$

Equation (10) indicates that a change in resonant frequency from its unperturbed value is caused by both the mass and liquid loading. At the fundamental resonance, $n = 1$, equation (10) reduces to the following,

$$\Delta f_s \approx -\frac{2f_s^2}{\sqrt{C_{66}\rho_q}}\left[\rho_s + \left(\frac{\rho\eta}{4\pi f_s}\right)^{1/2}\right]. \tag{10a}$$

Examining the first term in equation (10a) and introducing the mass of the deposited film, $M_f = \rho_f h_f S = \rho_s S$, and the frequency constant of a specific crystal cut, $N = \frac{V_{shear}}{2} = \frac{1}{2}\sqrt{\frac{\mu_q}{\rho_q}} = \frac{1}{2}\sqrt{\frac{\overline{C}_{66}}{\rho_q}}$ (see equation A-10 in the appendix A), the resonant frequency change due to mass loading in equation (1) can be expressed as,

$$\Delta f = -\frac{f_s^2}{N \cdot \rho_q \cdot S} M_f = -K_m M_f \,. \tag{10b}$$

Comparing equations (1) and (10b), one observes that the first term in equation (10a), describes the effect of mass loading.

Noting that $\mu_q = \overline{\overline{C}}_{66}$, the second term of equation (10a) can be simplified as follows,

$$\Delta f_s = -\frac{2 f_s^2}{\sqrt{\overline{\overline{C}}_{66} \rho_q}} \left(\frac{\rho \eta}{4 \pi f_s} \right)^{1/2} = -f_s^{\frac{3}{2}} \left(\rho\eta \big/ \pi \mu_q \rho_q \right)^{\frac{1}{2}} = K_l (\rho \eta)^{\frac{1}{2}} \,. \tag{10c}$$

where $K_l = \frac{f_s^{3/2}}{\sqrt{\pi \mu_q \rho_q}}$, is defined as the liquid sensitivity constant. Comparing equations (3) and (10c), one observes that the second term in equation (10a), describes the effect of liquid loading.

Equation (10) also shows that it is impossible to differentiate changes in surface mass from liquid properties when only the resonant frequency is monitored. The admittance of the modified BVD model in figure 6 can be expressed as follows,

$$Y = j\omega(C_0 + C_p) + \frac{1}{Z_m} = \frac{R_1 + R_2}{(R_1 + R_2)^2 + \left(\omega(L_1 + L_2 + L_3) - \frac{1}{\omega C_1}\right)^2}$$

$$+ j\left(\omega(C_0 + C_p) - \frac{\omega(L_1 + L_2 + L_3) - \frac{1}{\omega C_1}}{(R_1 + R_2)^2 + \left(\omega(L_1 + L_2 + L_3) - \frac{1}{\omega C_1}\right)^2}\right). \tag{11}$$

The maximum admittance occurs near the series resonant frequency of modified BVD model, which can be expressed as $\omega_s = \frac{1}{\sqrt{(L_1 + L_2 + L_3)C_1}}$. Near the series resonance, equation (11) can be reduced to the following,

$$Y_{\max} \approx \frac{1}{R_1 + R_2} + j\frac{C_0 + C_p}{\sqrt{(L_1 + L_2 + L_3)C_1}}. \tag{11a}$$

When mass and liquid loading are small, one obtains $L_2 + L_3 \pi\pi L_1$. Using the same values of R_1, C_1, C_0, L_1 used in the derivation of equation (6b) and $C_p = 7.62pF$, $R_2 = 34.1\Omega$ [22], the real part of equation (11a), $\frac{1}{R_1 + R_2} = 0.011$, is much greater than the imaginary part $\frac{C_0 + C_p}{\sqrt{(L_1 + L_2 + L_3)C_1}}$, which is smaller than $\frac{C_0 + C_p}{\sqrt{L_1 C_1}} = 1.346 \cdot 10^{-4}$. Equation (11a) reduces to,

$$Y_{\max} \approx 1/(R_1 + R_2) \tag{11b}$$

Substituting equations (7d) and (7f) into (11b) and using equation (7c) yields,

$$\frac{1}{Y_{\max}} \approx R_1 + R_2 = \frac{\eta_q}{\bar{\bar{C}}_{66} C_1} + \frac{1}{n\pi\omega_s C_1}\left(\frac{2\omega\rho\eta}{\bar{\bar{C}}_{66}\rho_q}\right)^{1/2} = \frac{\eta_q}{\bar{\bar{C}}_{66} C_1} + \frac{1}{n\pi C_1}\left(\frac{2\rho\eta}{\omega_s \bar{\bar{C}}_{66}\rho_q}\right)^{1/2}$$
$$= \frac{\eta_q}{\bar{\bar{C}}_{66} C_1} + \frac{1}{n\pi C_1}\left(\frac{\rho\eta}{\pi f_s \bar{\bar{C}}_{66}\rho_q}\right)^{1/2}. \tag{11c}$$

Equation (11c) shows that the maximum admittance depends on the liquid density viscosity product, $\rho\eta$, but is unaffected by the mass loading (ρ_s). If we measure the resonant frequency change of the QCM in the liquid and use an impedance analyzer to measure the admittance of the loaded QCM, the value of $\rho\eta$ can be obtained from equation (11c). Substituting this result into equation (10a) yields,

$$\Delta f_s \approx -\left[\frac{2 f_s^2 \rho_s}{n\sqrt{\bar{\bar{C}}_{66}\rho_q}} + \left(\frac{1}{Y_{\max}} - \frac{\eta_q}{\bar{\bar{C}}_{66} C_1}\right)\frac{f_s^2 \pi C_1 \sqrt{\bar{\bar{C}}_{66}}}{\sqrt{\bar{\bar{C}}_{66}}}\right]. \tag{11d}$$

Equation (11d) indicates that the resonant frequency change due to film mass loading could be separated from changes in liquid properties, if the admittance of the loaded QCM is also measured.

Another possible approach is to use a differential setup with one coated and one uncoated QCM sensor submerged in the liquid to be analyzed. The resonant frequency of both QCMs will change according to equation (10a). However according to equation (10c) the frequency change in the uncoated QCM will be due only to the change of the liquid density viscosity product ($\rho\eta$), while the frequency change of the coated QCM will be due to the liquid density viscosity product change and mass changes in the coating. The first prerequisite of the differential setup is that the resonant frequency changes of the coated and uncoated QCM caused by the change of liquid properties are the same. From equation (10c) we know, the resonant frequency f_s (5 or 9MHz), density ρ_q (2.648 g cm^{-3}) and shear modulus μ_q (2.947x10^{11} dyne cm^{-2}) of QCM will be different before and after it is coated with polymer. However, the mass of the polymer film ($26.5\mu g$) is very small compared to the mass of QCM (11.9g), hence, the change of the density ρ_q and shear modulus μ_q of QCM can be neglected. The resonant frequency shift (1.5KHz in section 3.2.2) due to polymer coating is also very small compared to the resonant frequency of commercial QCM (5 or 9MHz). Using equation (10c), the resonant frequency shifts, Δf_s, of the coated and uncoated QCM caused by putting them from air into water ($\rho = 0.9982 g/ml, \eta = 1.002 \times 10^{-2} dyne \cdot s/cm^2$ at 20 °C) respectively, can be calculated as 713.8Hz and 714.1Hz respectively. Hence, the difference between the resonant frequencies of the above two QCM submerged in the liquid to be analyzed is determined only by the mass of the compounds absorbed on the coated QCM. Another prerequisite is that the bare QCM shouldn't absorb either target or interferent compounds within the liquid. If the uncoated QCM also absorbs other compounds within the liquid, but not the target compounds, the differential setup still cannot distinguish the mass loading of target compounds from liquid loading.

Equation (10) also indicates that there are not any cross terms between the mass loading term and liquid loading term, it results in that there is no effect on liquid loading response due to the coating film. However, equation (10), which is derived in appendix C, is based on numerous approximations. It is possible that there are some cross terms, which correlated mass loading term and liquid loading term in equation (10) and result in the mass loading or liquid loading phenomena of the coated QCM being shielded by the coated film.

2.1.5 The response mechanism between analytes and the polymer coating

In order to detect specific analytes or classes of analytes sensitively and selectively, an analyte specific film is coated on the sensing surface of the QCM sensor. To make the QCM sensor respond reversibly and recover after the analyte compound is removed, the selected film should not form covalent bonds to the target analyte. Interactions between the target analyte and the film should be limited to dispersions, dipolar, and hydrogen-bonding interactions [23]. Since these interactions are inter-molecular forces, they are typically grouped together and termed as van der Waals forces, which are much weaker than covalent bonds. A variety of films may be used to coat QCM sensors, such as inorganic films, organic films, polymer films and biofilms etc.

McGill [24] pointed out that the chemical processes that govern the sensitivity and selectivity of a polymer coated QCM sensor are very similar to those of the solution process of an analyte in a liquid solvent. The responses of the polymer coated QCM devices can be understood more conveniently by first examining what governs the solution process of the analyte in a solvent polymer phase. This process includes two main processes: cavity formation and insertion of the solute molecules into that cavity. In the first step, a cavity is formed in the solvent, which is the polymer in this case, to make a room for the analyte molecule. Cavity formation is an endothermic process, in which the interactions of polymer molecules are broken. In the second step, a solute analyte molecule is inserted inside the cavity and forms interactions with the surrounding solvent polymer molecules. During this stage the polymer molecules may rearrange their dipoles or functional groups to maximize the strength of their interaction with the inserted analyte molecule and to maintain the strength of interactions between polymer molecules. The solvent-solute (polymer-analyte) interactions include van der Waals or London dispersion forces and, when indicated, dipolar, polarizable, and hydrogen-bonding interactions. All these interactions are exothermic and the energy balance between this exothermic process and the endothermic cavity formation process largely determines the extent to which the target analyte interacts with a solvent polymer coating.

Since the polymer film coated on the QCM is in the solid state, the interaction between polymer and analyte is unlikely to change its viscosity. Since the mass of the polymer is increased after the formation of polymer-analyte interactions, the density of the polymer may change also.

The amount of the analyte that the polymer can adsorb depends on the environmental temperature, the concentration of the analyte and the effective surface area of the polymer [25,26]. The concept used to describe the adsorption of a gas on the surface of a solid, is the adsorption isotherm. The adsorption isotherm is the relationship between the pressure of the gas and the amount of the gas adsorbed by the solid at a constant temperature. In liquid phase, the adsorption isotherm can be understood as the relationship between the concentration of the analyte and the amount of analyte absorbed on the effective surface, or in the available cavities of the polymer. The adsorption isotherms can be classified as monomolecular adsorption and multimolecular adsorption. The basic model used to describe monomolecular adsorption is Langmuir adsorption isotherm. The langmuir adsorption isotherm is based on three assumptions: analyte molecules can be represented by uniform spheres, only a monolayer of adsorbed molecules can be formed and all adsorption sites are equivalent and are unaffected by the presence of analyte molecules at adjacent sites. More generally the adsorption is not limited to a monomolecular adsorption, but can continue until a multimolecular layer of analyte covers the effective surface of the polymer. The model used to describe the multimolecular adsorption is the BET (Brunauer-Emmett-Teller) adsorption isotherm. Fig 7 shows the two adsorption isotherms. The shape of both adsorption isotherms is linear in the low concentration region. The shape of the isotherms will affect the shape of the frequency shift versus target concentration curves in chapter4.

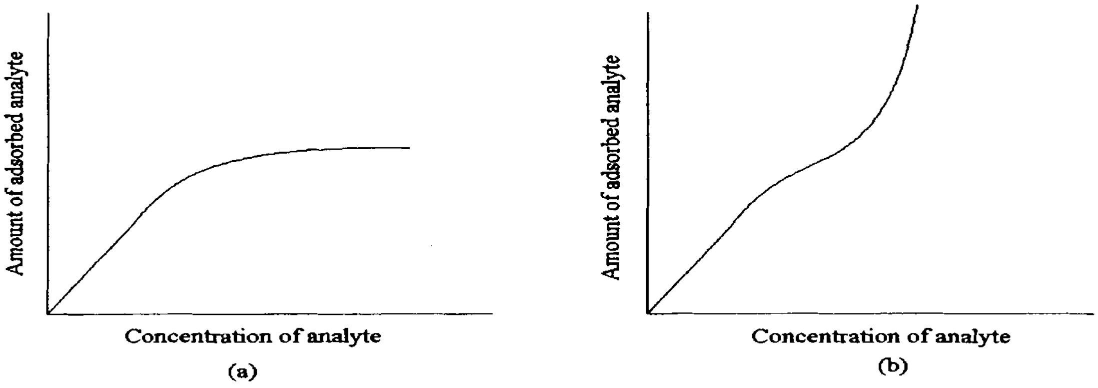

Figure 7: Adsorption isotherms.

(a) Langmuir adsorption isotherm,

(b) BET adsorption isotherm.

2.2 Semiconducting Metal Oxide Sensor

2.2.1 The configuration of WO_3 thin film

The configuration of the WO_3 thin film sensors made by other researchers in the Laboratory of Surface Science and Technology (LASST) at the University of Maine is shown in figure 8. The 3000 Å thick interdigital platinum electrodes on insulating r-cut sapphire substrates were patterned by photolithography. The 500Å thick metal oxide semiconducting film, which is, tungsten trioxide WO_3, was deposited across the interdigital fingers of the platinum electrodes using RF sputtering techniques. Before depositing WO_3, the tungsten target was pre sputtered in argon for 5 minutes in order to get a pure tungsten target. The deposition parameters for WO_3 were: 500°C substrate temperature, 50% argon / 50% oxygen gas flow rate, a total pressure of 3 mTorr, and deposition rate of 1Å/s. The sample was rotated during the sputtering process in order to evenly coat the sensors. The gold doping was accomplished using a low temperature effusion cell technique (evaporative process). The rate for the gold doping was 2Å/minute and the thickness of the gold-layer was 15Å. After the deposition process, the sample was annealed in room air at 400°C in an oven for 24 hours.

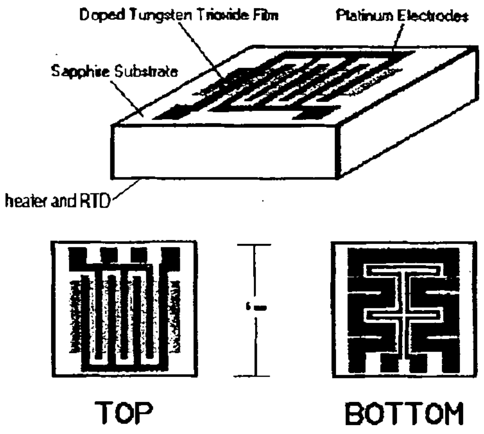

Figure 8: WO_3 sensor structure.

Because the interaction between the target gas and the sensing film depends on the temperature of the sensing film, it is important to control the operating temperature of the sensing film. A serpentine heating element made of platinum deposited on the bottom of substrate provides enough heat to maintain the sensing film at the desired temperature. The desired temperature is measured through a resistance temperature device (RTD), which is also deposited on the bottom of substrate. Between the platinum and the substrate there is a 200Å layer of zirconium, which aids in adhering the platinum to the sapphire substrate. Photolithography techniques are employed to make the platinum heater and RTD patterns. The platinum and zirconium are deposited at room temperature by electron beam evaporation. The deposition rates for platinum and zirconium were 2~4 Å/s and 2Å/s respectively.

2.2.2 Mechanism of interaction between the target gas and the SMO film

Most semiconducting metal oxide films such as WO_3 are n-type semiconductors. The n-type behavior is due to the fact that oxygen vacancies exist in the film. Therefore the ratio of oxygen ions to tungsten ions is not exactly three to one but slightly less. This gives rise to weakly bonded electrons around some of the tungsten ions. These weakly bonded electrons readily enter the conduction band causing the metal oxide to be n-type. The oxygen vacancies are then said to act as donors in the film. Since the geometry of the film is severely interrupted at the surface, this could lead to localized allowed energy levels, which may occur in the energy gap. Since metal oxides are more ionic than covalent in nature, the metal ion is referred to as the cation and oxygen is the anion. The surface metal ions have an incomplete outer shell of electrons and hence tend to capture extra electrons and therefore act as acceptors. On the other hand, the oxygen ions on the surface have only two electrons in their outer orbit and therefore tend to give up their electrons and act as donors. Figure 9 shows the band structure of the metal oxide semiconductor surface. In this case, there is no net surface charge and it is called the flat-band case. The surface states are shown as narrow bands with the donor states occupied and the acceptor states unoccupied.

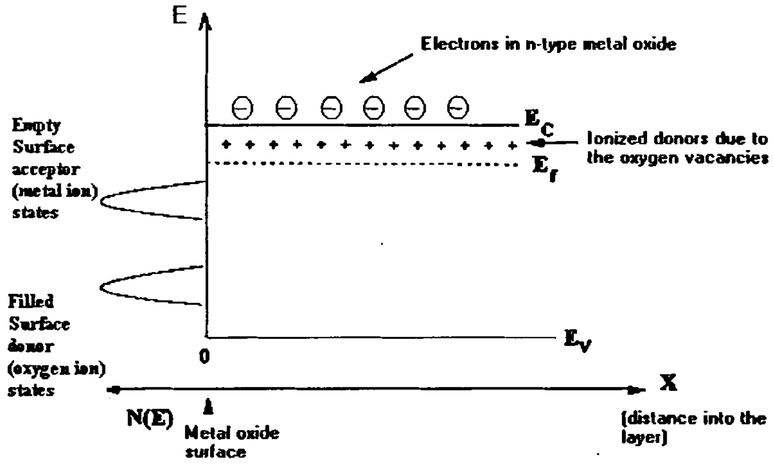

Figure 9: Band structure for an n-type metal oxide.

The surface band structure can be modified by charged surface acceptor states or ionized surface donor states through introducing a space charge layer (depletion layer). These varied surface states are mainly caused by intrinsic defects or by the adsorption of foreign atoms and molecules. In thermal equilibrium, the occupation probability for surface states can be obtained by Fermi statistics and expressed by means of the Fermi level E_f, as for bulk states [27].

When the n-type metal oxide film is exposed to a target gas, chemsorption is usually considered as the dominant mechanism for the interactions between the metal oxide surface and the target gas [28]. Figure 10 shows the case of a depletion layer induced by adsorbing an oxidizing agent, such as oxygen and figure 11 shows the case of an accumulation layer induced by adsorbing a reducing agent, such as hydrogen or hydrogen bearing gases.

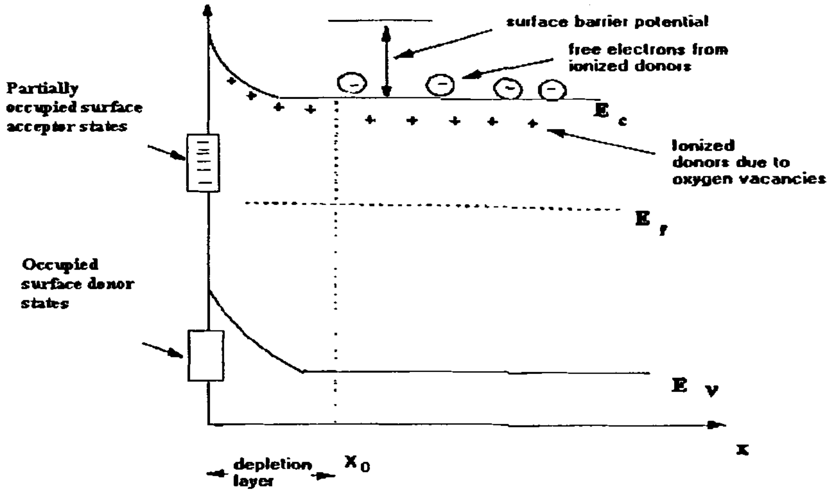

Figure 10: The double layer near a metal oxide surface.

When an oxidizing agent is adsorbed on a metal oxide surface and extracts electrons out of the bulk donor sites (oxygen vacancies) partially occupied surface acceptor states are produced. A so-called double layer is then formed which has positively charged donor ions in the semiconductor and negatively charged surface acceptor states as a sheet of charges on the surface. The double layer is shown in Figure 10. The region $0 < x < x_0$ is called the space charge layer or depletion layer and is depleted of any mobile charges. The carrier density within the space charge layer is decreased hence the conductivity near the surface is decreased also.

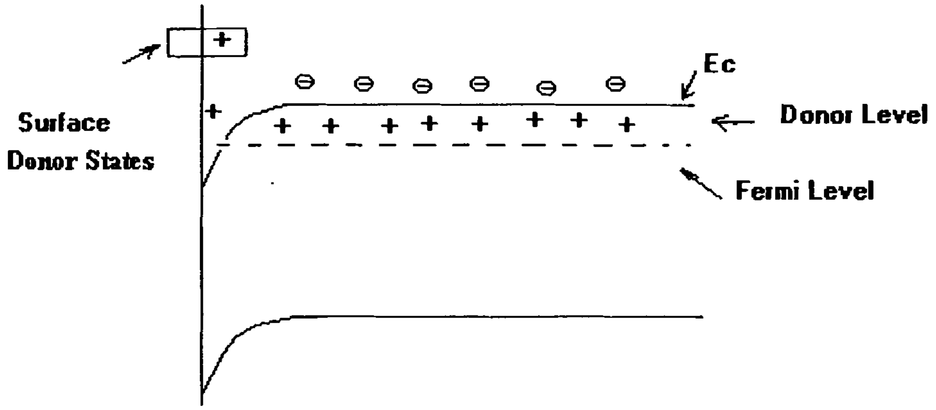

Figure 11: An accumulation layer in an n-type metal oxide.

When a reducing agent is adsorbed on the surface of a metal oxide and donates electrons to the space charge layer surface donor states are produced. The accumulation layer is caused by these surface donor states that are located near the conduction band of the semiconductor. The carrier density within the space charge layer is increased hence the conductivity near the surface is increased also.

The most fundamental reaction for a SMO sensing film operating in air is the reaction between oxygen and the film. Reducing gases can react with oxygen adsorbed on the surface or with surface lattice oxygen. Oxygen from the air is required to restore the film to its pre-exposure condition. Basically, the adsorption of oxygen can be described in terms of the following reaction steps [29]:

$$O_{2\,(gas)} + e^{-1} \rightarrow O_2^{-1}{}_{(surface)} \tag{12}$$

$$O_2^{-1}{}_{(surface)} + e^{-1} \rightarrow 2O^{-1}{}_{(surface)} \tag{13}$$

$$O^{-1}{}_{(surface)} + e^{-1} \rightarrow O^{-2}{}_{(surface)} \tag{14}$$

As discussed before, the carrier concentration within the space charge layer is decreased by formation of the above surface charged states. That means the concentration of surface oxygen vacancies (with respect to the lattice they were charged +1 or +2 after dissociation of one or two electrons into conduction band) is also decreased by ambient oxygen. At sufficiently high temperatures and after adequate time a diffusion of oxygen vacancies also takes place and results in a decrease of the conductivity. Eventually an equilibrium between bulk oxygen vacancies and ambient oxygen will be established [30]. This equilibrium can be described by the following reactions:

$$O^{2-}_{(lattice)} \leftrightarrow V_o^{+} + e^{-} + \frac{1}{2}O_{2\,(gas)} \tag{15}$$

or

$$O^{2-}_{(lattice)} \leftrightarrow V_o^{2+} + 2e^{-} + \frac{1}{2}O_{2\,(gas)} \tag{16}$$

where V_o is the oxygen vacancy.

When the SMO film reacts with a reducing agent such as H_2S, the carrier concentration of the surface charge layer is increased by the production of additional surface donor states(oxygen vacancies). The equilibrium mentioned above is broken and the reaction can be described by the following reaction:

$$3O^{2-}_{(lattice)} + H_2S \rightarrow 3V_o^{2+} + H_2O_{(gas)} + SO_{2\,(gas)} + 6e^{-} \tag{17}$$

The competition between the formation of the oxygen vacancies by interaction with H_2S and the reoxidation by O_2 will result in the formation of a steady state concentration of oxygen vacancies [31]. A new equilibrium is reached and the conductivity is increased when the redox reaction is completed. Since phosmet is a thermally unstable organophosphorous pesticide, a slow process of degradation of phosmet already occurs below 50 °C with the formation of small quantities of sulfur containing compounds such as disulphides[32]. Hence, when the SMO film reacts with phosmet gas, the conductivity of the sensing film will be increased.

2.2.3 Mechanism of Au catalyst

It has been found that a small amount of a certain metal added to a metal oxide promotes the heterogeneous catalytic process. This enhanced catalysis is called the effect of strong metal –support interaction (SMSI) in catalysis chemistry [33]. In the case of interactions between a solid and gas, this effect is called spillover [34]. This effect consists of the formation and migration of dissociatively adsorbed gas species on the metal oxide surface doped with metal particles. The doping material used for the WO_3 film in this thesis is Au, which is one of the typical noble metals used as a catalyst for metal oxide sensing films.

Typically, a catalyst is added to a metal oxide semiconductor to speed up a chemical reaction. Ideally, finely divided particles of the catalyst should be added so that there is a large surface area. The catalyst, although critical to the chemical reactions, does not undergo any changes during the reaction. The catalyst can play two important roles in the chemical reaction. First, it can concentrate the reactants by adsorbing the appropriate gas molecules. Second, it can provide a reaction path, which requires a small amount of activation energy.

In general, two spillover models have been proposed: chemical sensitization and electronic sensitization, which are described in figure 12 [35]. In the chemical sensitization model, the role of the metal additive is to activate and dissociate the reactants that spillover and reduce the surface of the metal oxide. In this case, the change in oxidation state of the metal oxide is the origin of the film conductivity change. In the electronic sensitization model, the metal additive donates or accepts electrons to/from the metal oxide, and the origin of conductivity change is the change in oxidation state of the metal additive.

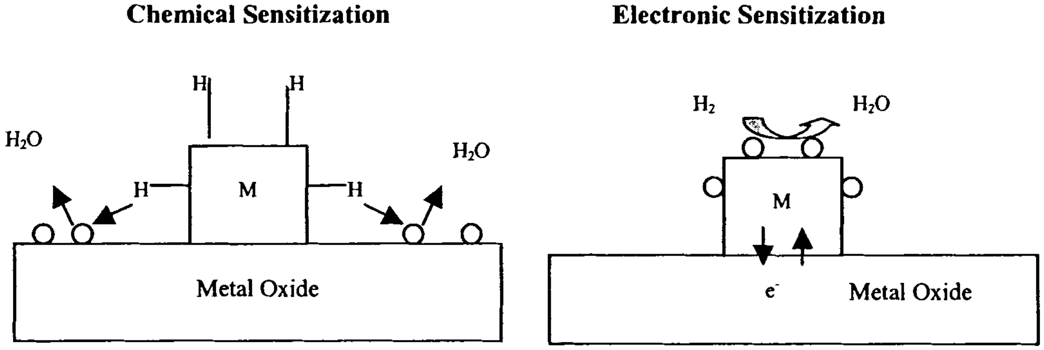

Figure 12: Spillover model.

Since Au is a very inert material [36], it is very hard to get or lose electrons. When the gold doped WO_3 film reacts with phosmet gas, phosmet molecules could be adsorbed on the surface of gold and to be activated and dissociated, then migrate or spillover to the WO_3 surface. The activated species thus react with the adsorbed or surface oxygen of WO_3 film, resulting in the increase of the conductivity of WO_3 film.

Baili Hu [59] in LASST presented another spillover model, shown in figure 13 to explain the results obtained from X-ray photoelectron spectroscopy (XPS) experiments, which were performed to demonstrate that Au doping on the top of a WO_3 film promoted reduction of WO_3 by NH_3. She pointed out that the Lewis acid sites W^{+6} serve as a source of adsorbed NH_3 that is bound to the WO_3 surface by donating its lone pair electrons to empty 5d orbital of W^{+6}. Coordinately, the adjacent Au particle acting as a bridge of electron transfer from N to W and finally back to H to facilitate bond breaking of N-H. Subsequently, the transient disassociatively adsorbed species such as NH_2, NH or H migrate and reduce the WO_3 surface. Since H_2S, which is a thermal break down compound of phosmet, is also a reducing agent, it is possible a similar mechanism could be involved.

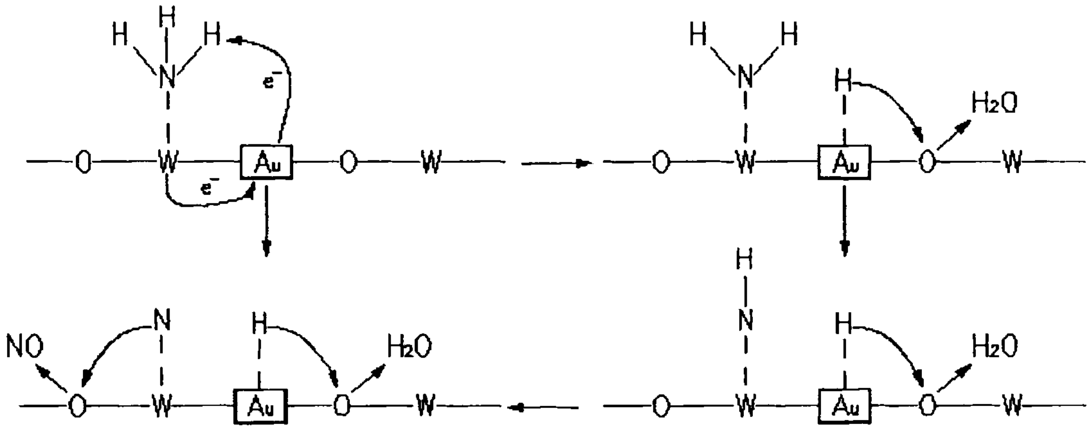

Figure 13: New spillover model.

3 EXPERIMENTAL SETUP

This chapter describes the physical design characteristics of both the QCM and SMO test system, including a discussion of the properties of the pesticide samples, the frequency measuring system, the gas delivery system, electronic hardware and temperature control system. The operating principles and parameters of GS/MS and purge & trap concentrator are also presented in this chapter.

3.1 The Physical and Chemical Properties of the Target Pesticide

The chemical name of phosmet is S- [(1,3-dihydro-1, 3-dioxo-2H-isoindol-2-yl) methyl] O, O-dimethyl phosphorodithioate (CAS RN 732-11-6)[37]. The structure is shown in figure 14. Phosmet (98% pure) is a colorless crystal, while technical grade is a white to pink solid (70% pure). It has a molecular formula of $C_{11}H_{12}NO_4PS_2$, a molecular weight of 317.33, and a melting point of 71.9 °C. Phosmet is thermally unstable; it begins to decompose at 65 °C and more rapidly above 100 °C [38]. The solubility of phosmet is 25 mg/l at 25 °C in water, 50 g/l in methanol, 650 g/l in acetone. The vapor pressure of phosmet is 0.065 mPa at 25 °C and 0.0128 Pa at 50 °C. The vapor pressure of phosmet is the pressure exerted by its vapor when phosmet and its vapor are in dynamic equilibrium. The vapor pressure of a substance depends upon the environmental temperature and can be used to calculate the concentration of the substance in the gas phase within a sealed container.

Phosmet is used on fruit (e.g. apples, pears, peaches, apricots, cherries and blueberries, citrus, grapes), potatoes and in forests. The tolerance of phosmet ranges from 0.1 to 40 ppm in food and is 10 ppm maximum in blueberries [39]. Phosmet is a non-systemic pesticide and acaricide with predominantly contact action by cholinesterase inhibition. The acute oral LD_{50} (Lethal Dose 50) for rats is 230-299 mg/kg; the acute dermal LD_{50} for albino rabbits is >3160 mg/kg. The probable lethal dose for humans is 50-500mg/kg. Symptoms of toxicity include headache, giddiness, nervousness, blurred vision, weakness, nausea, cramps, diarrhea, abdominal cramps, shock, heartburn, confusion, dizziness, hepatic damage, and discomfort in the chest. Signs include sweating, miosis, tearing, vomiting, muscle atrophy, twitching and death due to respiratory failure [40].

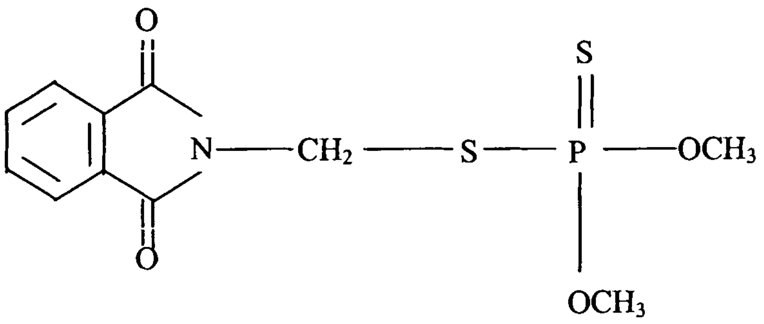

Figure 14: Chemical structure of phosmet.

3.2 Experimental Setup, QCM Measurements

3.2.1 Sample preparation

The phosmet solution was prepared by dissolving 50.3mg of analytical 98% purity phosmet, which was purchased from Crescent Chemical Co., Inc., in 2ml of methanol. The concentration of this solution is 3.2% by weight. Since methanol is a volatile solvent and the container of phosmet solution was opened and closed several times during the experiment, the methanol evaporation results in the concentration of the phosmet solution gradually increasing with use. By the end of the experimental runs, the concentration of phosmet solution was 3.5% as determined by the weight of solution before and after the experiments.

In order to obtain liquid samples for testing of phosmet treated blueberries and organic (untreated) blueberries, two bags of organic blueberries were obtained directly from a farm and one bag was sprayed with phosmet solution by Dr. Brian Perkins from the Food Science Department. The concentration of phosmet on the treated blueberries was measured as 2.5ppm through GC/MS by Dr. Perkins. 216g of treated blueberries were then put into a beaker with 200ml water, as shown in figure 15. After 30 minutes stirring followed by filtration with a Whatman filter paper, 200ml treated blueberry juice was obtained. If all the phosmet applied to the blueberries dissolved in the water, the phosmet concentration would be 2.75ppm. Organic blueberry juice was prepared using the same method.

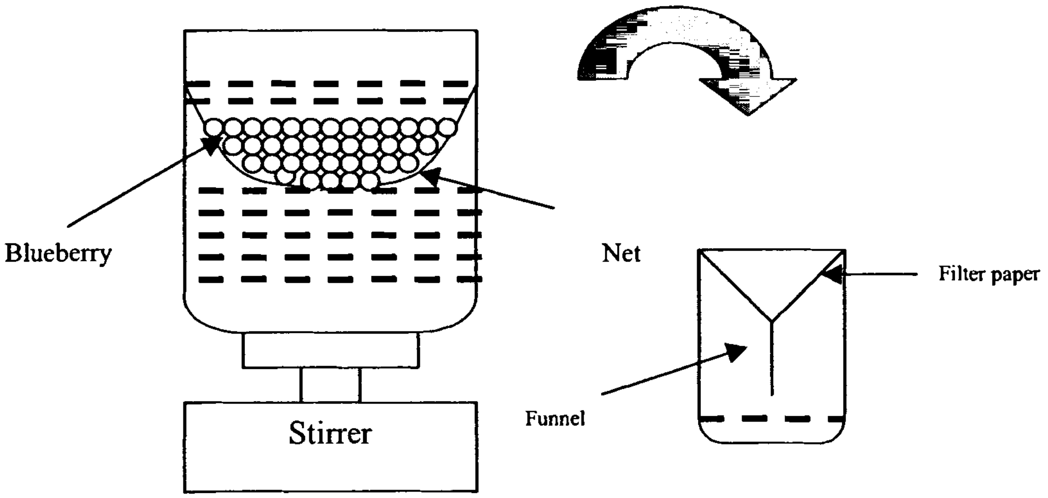

Figure 15: Apparatus for the preparation of blueberry juice.

3.2.2 Coating preparation

Polyepichlorohydrin (PECH) with a chemical formula $[C_3H_5ClO]_n$ and polyvinyl alcohol (PVA) with a formula $[C_2H_4O]_n$ was recommended by Dr. Todd Mlsna [64] as a good coating material to detect phosmet. Since the QCM measurants are performed in the liquid phase, an important requirement in the coating selection is the coating stability in water. Since PVA swells in water, PECH became the only polymer candidate in this experiment. Figure 16 shows the chemical structure of PECH. 223mg of PECH purchased from Fisher Scientific was dissolved in 27.56g chloroform to make the coating solution. Several drops of the coating solution were applied to the surface of the sensing electrode of the QCM (see figure 1) using a syringe. After being evaporated with a flow of dry nitrogen, a frequency shift of approximately 1.5 KHz from the uncoated resonant frequency was observed. To make the QCM reusable, the PECH coating can be washed off by using acetone at 50 °C [41].

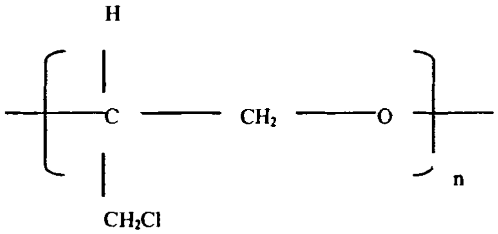

Figure 16: The chemical structure of PECH.

3.2.3 Liquid phase QCM measurement system

The system for liquid phase measurement is shown in Figure 17. A commercial 5 MHz AT-cut QCM (model number 149211-1, Maxtek, Inc) was used as the sensing platform. This quartz crystal was installed into a crystal holder (model number CHT-100, Maxtek, Inc). A commercial oscillator (model number PI-70, Maxtek, Inc) was used to drive the QCM submerged in a water bath at room temperature. Using a syringe, amounts ranging from 2-20 μl of the 3.2% phosmet solution were then injected into the water bath. A magnetic stirrer was used to continually mix the solution while a PC recorded the output frequency of the frequency counter, which is used to measure the output frequency of the oscillator. Even though the resolution of frequency counter is 0.1 Hz, the observed noise level in the frequency measured during the tests was 1Hz. In separate experiments, two additional beakers A and B were used to flush the solution from the water bath. During this process valve A was totally opened and valve B was used to maintain the constant water level in the water bath.

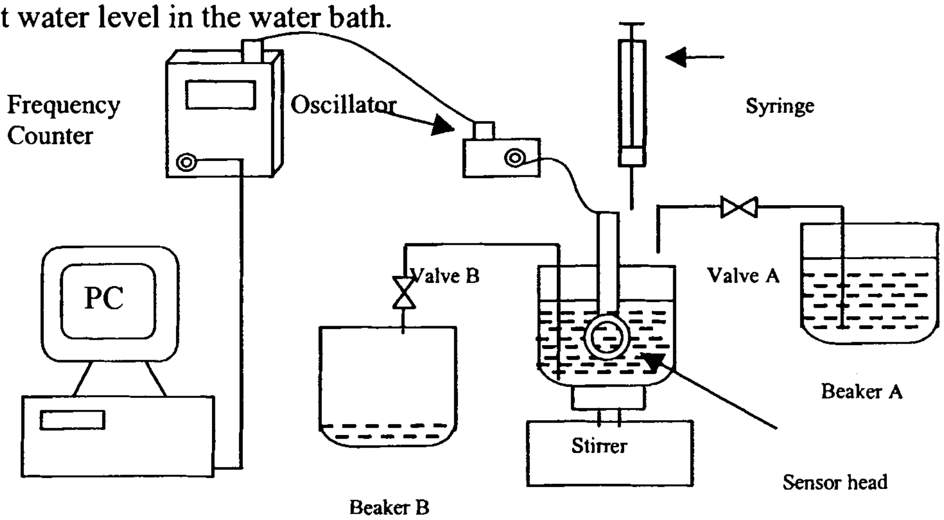

Figure 17: Frequency measuring system.

3.2.4 Phase shift of quartz crystal in oscillating circuit

When the QCM is electrically excited into resonance by applying a voltage across the electrodes, a standing shear wave is formed across the two surfaces of the crystal disk. In order to sustain the generated standing wave, it is required that there be no net gain or loss in energy through the process of the wave generation, propagation and regeneration. However, these processes are not 100% efficient due to frictional losses, viscous losses and inefficient coupling of the electric field to the piezoelectric material, so that the wave motion will be dampened. Therefore, extra electrical energy is needed for the acoustic wave to ensure a constant physical wave amplitude and continuous wave propagation. An oscillating circuit shown in the upper part of figure 18 can continuously provide the amount of additional energy required to sustain the resonance of the QCM, with a positive feedback that uses the QCM as the frequency control element. The magnitude and phase of the QCM impedance also can be measured by connecting an impedance analyzer to the sensing electrodes of the QCM as shown in the lower part of figure 18. A frequency counter shown in figure 17 is used to measure the resonant frequency of the oscillating circuit.

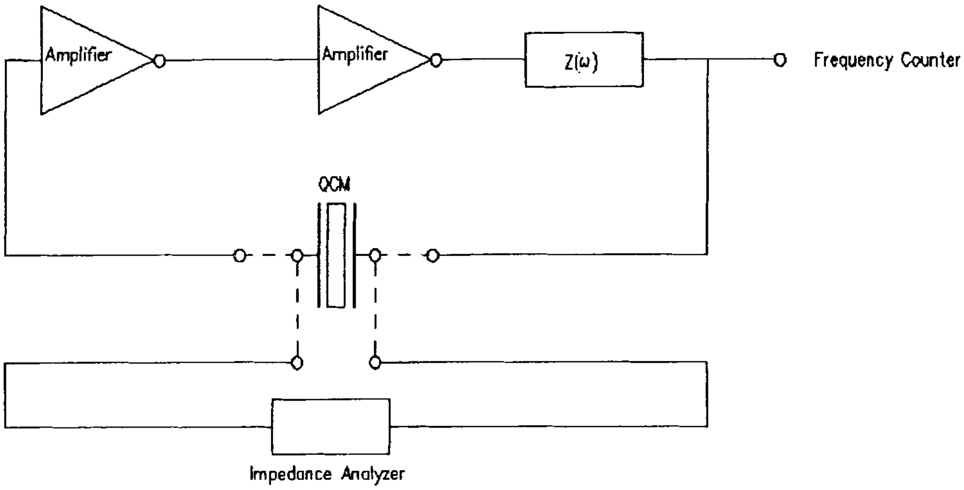

Figure 18: The typical oscillating circuit used to drive a QCM.

In order to have the current wave in the oscillating circuit to add in phase, the operating constraint of the oscillator circuit requires that the total phase shift in the oscillating circuit must be equal to $2n\pi(n = 0,1,2...)$, etc. radians. In order to make the QCM work at its series resonant frequency, which is usually defined as the frequency of the minimum impedance of the resonator or the frequency at zero phase, the impedance phase of the resonator should be zero. If the unknown impedance shown in figure 18 is $Z(\omega) = 0$, the phase shift of the amplifier has to be $2n\pi(n = 0,1,2...)$ to make the QCM work at its series resonant frequency. Since the phase shift of an amplifier or inverter is π, therefore two series amplifiers in the oscillating circuit are necessary.

It would be ideal if there were no phase shifts in the amplifiers and $Z(\omega)$ was zero. In this case, the output frequency of the QCM would be equal to the series resonant frequency of the QCM, f_s. At the series resonant frequency, the impedance of the resonator is minimum and the admittance is the maximum. However, the series and parallel-added capacitors, resistors and/or inductors of the practical oscillator circuit, which are due to the external components and the circuit board and shown as $Z(\omega)$ in figure 18, cause the circuit to operate at a constant nonzero phase. The phase shift introduced by $Z(\omega) = |Z|e^{j\phi_1}$ would be ϕ_1. Hence to get oscillations the phase shift in the QCM must be $-\phi_1$. Hence, the modified BVD equivalent circuit model shown in figure 6, that describes the QCM simultaneously loaded by a thin surface mass layer and a semi-infinite Newtonian liquid needs be revised. Figure 19 shows the revised equivalent circuit model. When the QCM operates in air, the elements to describe the mass and liquid loading phenomena, L_2, R_2, and L_3 are zero.

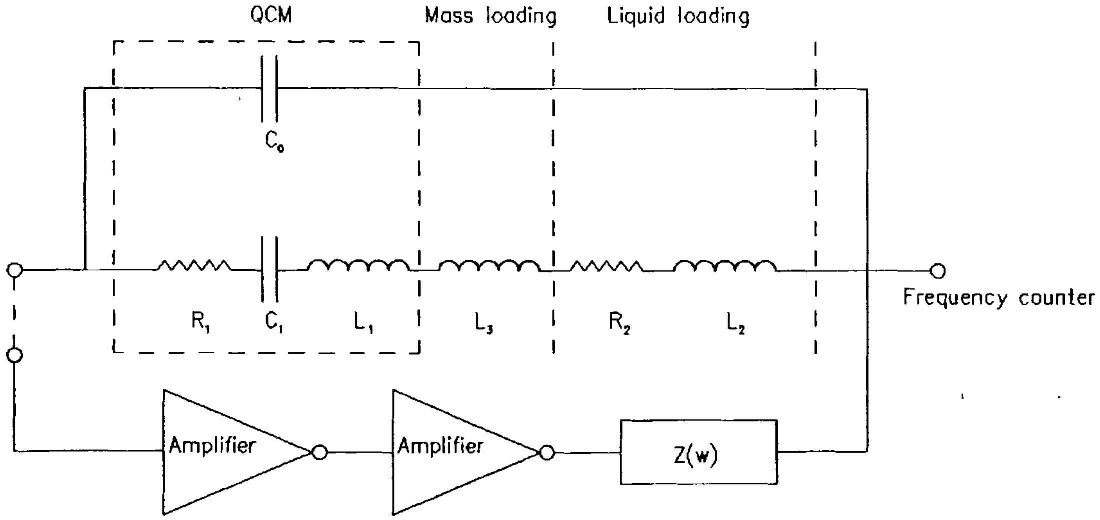

Figure 19: The new equivalent circuit model.

The phase shift, ϕ_1, of the QCM oscillator circuit was obtained from the experimental results of Dr. Chao Zhang [52]. Dr. Chao Zhang used the same frequency measuring system described in figure 17 to measure the resonant frequency change of a bare QCM with the same standard geometry shown in figure 1, when exposed to various concentrations of NaCl in water. Using an impedance analyzer, the impedance of the same bare QCM sensor was also measured during exposure to NaCl solutions of similar concentration. The frequency change at different constant phase values as a function of the NaCl concentration was obtained from the measured impedance curves. Comparing these results with the resonant frequency change versus NaCl concentration measured using the commercial oscillator circuit, showed that the commercial oscillator operates at approximately -60° phase.

3.3 Experimental Setup, SMO Measurements

3.3.1 Gas delivery system

Since the SMO sensor only can operate in the gas phase, a gas delivery system was built to deliver the phosmet gas to SMO sensor. Figure 20 displays a diagram of the gas delivery system developed for the present work. This gas delivery system consists of one Tylan model FC-260 mass flow controller (MFC1) with a flow rate of 0~30 standard cubic centimeters per minutes (SCCM), two Hastings model 202A mass flow controllers (MFC2 and MFC5) with flow rates of 0~10 and 0~100 SCCM respectively. Two Brooks rotameters (FC3 and FC4), a control circuit for the above MFCs, a bubbler, two sample channels, one sensor chamber, one Fisher Isotemp Oven, one 6-way valve, ¼ inch Teflon and stainless steel tubing and various Swagelock fittings to connect the elements to the system are also included.

In figure 20, MFC1 regulates the flow of the dry carrier gas. The carrier gas is grade 2 compressed dry air. MFC2 provides dry air for the bubbler that produces saturated water vapor. A carrier gas with various humidity levels can be obtained by manipulating the flows of MFC1 and MFC2. Because the measured resistance of the SMO film depends on the flow rates of the carrier gas, FC3 and FC4 are used to establish the same flow rate in the two channels. MFC5 is used as a flow meter to monitor the flow through the sensor chamber. The 6-way valve switches the flow from one channel to another and the two exits prevent the air pressure from changing abruptly during switching. Figure 21 shows the flow paths of 6-way valve. The two sample channels were fabricated in the LASST machine shop. A 2-inch long hole was drilled in the middle of the aluminum rod and two fritted filter discs were put at both ends of the channel. 24.2mg of analytical phosmet powder was put into one of these channels and this channel provides phosmet gas when air blows through it. Figure 22 shows the structure of the sample channel. Since the vapor pressure is a strong function of temperature [42], these channels were put into an oven whose temperature can be elevated from room temperature to 150 °C. To estimate the maximum phosmet concentrations within the sample channel at 25 °C and 50 °C, the sample channel was assumed to be a sealed container and the phosmet solid and its vapor are in dynamic equilibrium state. The partial pressure of phosmet gas in equilibrium, which is the ratio of the vapor pressure of phosmet to the sum of phosmet vapor pressure and atmosphere pressure at certain temperature, can be used to express the concentration of the phosmet gas. The estimated maximum concentration of phosmet gas within the sample channel is 1ppb at 25 °C and 1.1ppm at 50 °C respectively. During an actual experiment air passes through the channel, so the actual phosmet concentration will be much less than its equilibrium value.

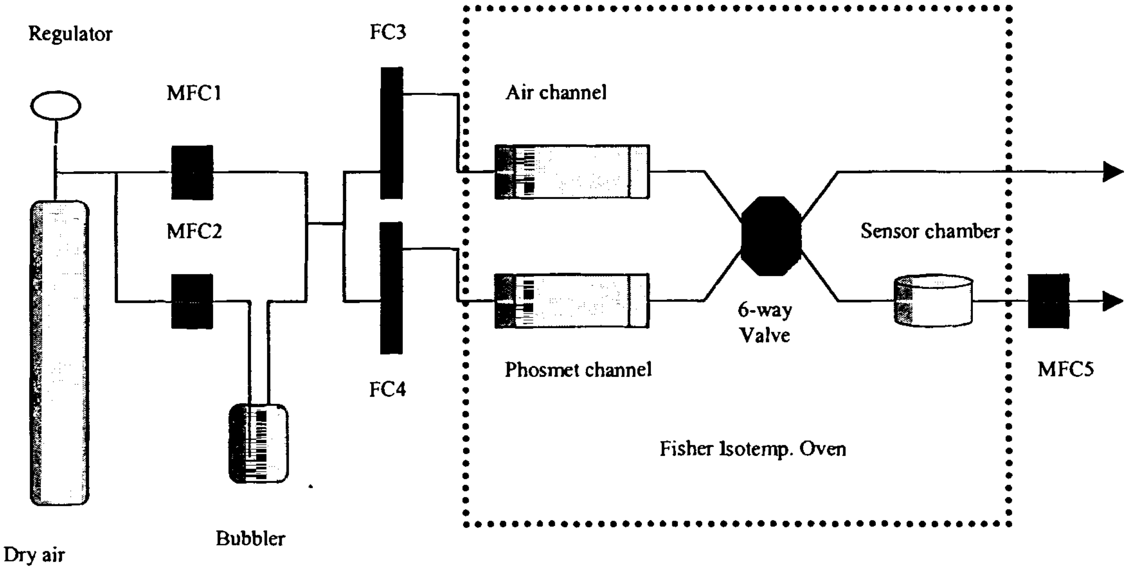

Figure 20: Gas delivery system.

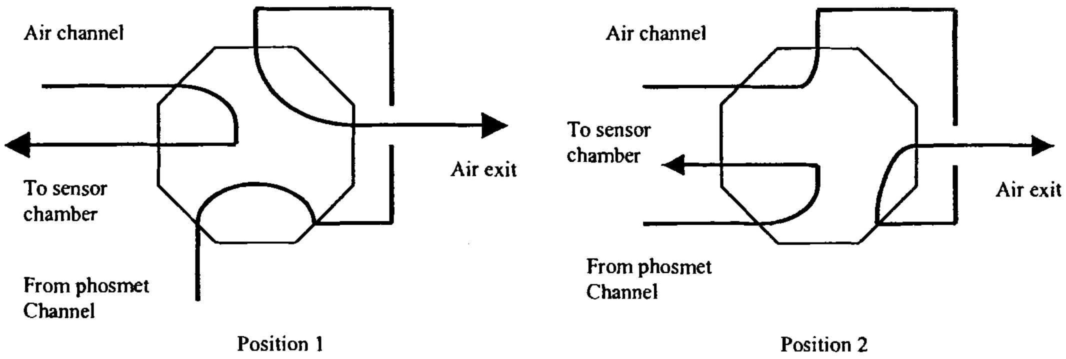

Figure 21: Flow paths of the 6-way valve.

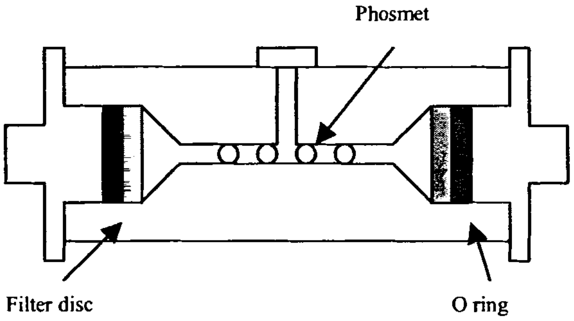

Figure 22: Structure of the sample channel.

3.3.2 Data acquisition and temperature control system

Because the conductivity of the SMO film changes during its interaction with a target gas, a data acquisition system was set up to record the resistance of the film. Since the interaction between the film and target gas depends on temperature, a heating/temperature control system was built to provide enough heat to maintain the temperature of the film. The data acquisition system consists of a Keithley 2400 source meter, a Keithley 617 electrometer, the data acquisition board and a computer. The temperature control system consists of a Kepco power supply and a Watlow series 980 model temperature controller. Both systems are shown in Figure 23.

In figure 23, the platinum RTD of the sensor was connected to the temperature controller input. The 1~5V output of the temperature controller was connected to the programming voltage input of the Kepco power supply, which converts the changing voltage input signal to a 0~3A current signal. This current signal provided the power for the serpentine heater on the bottom of the sensor. The difference between the desired temperature and the actual process temperature measured by the RTD can be minimized by the built in PID algorithm of the temperature controller. Since the RTD calibration curve of the sensor RTD is different from the standard European curve within the Watlow temperature controller, a measured RTD resistance versus temperature conversion curve was used. First the RTD resistance at the desired temperature is determined from the calibration curve, and then the temperature corresponding to that RTD resistance from the standard European curve can be entered into the controller as the set point.

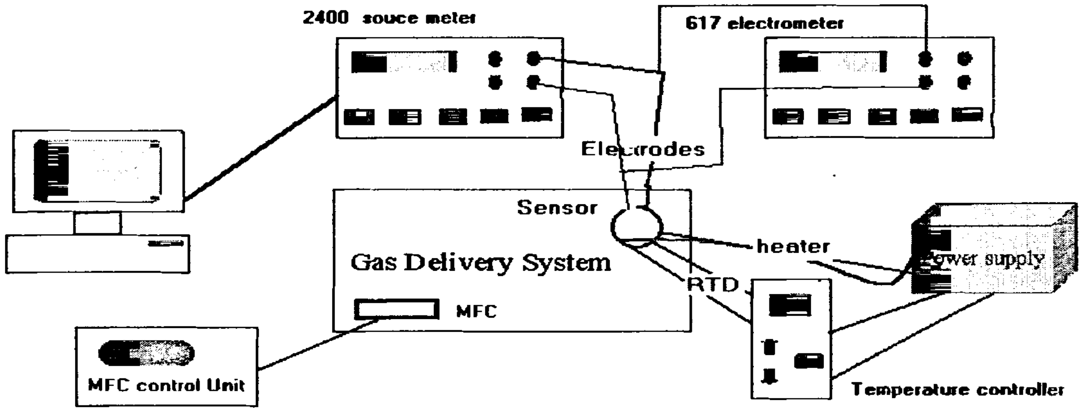

Figure 23: Diagram of the data acquisition system.

The source meter provided a constant 2.5V voltage across the film and the electrometer recorded the current through the film. The data from both meters were transmitted to a personal computer via a computer Boards GPIB (General Purpose Interface Bus) card. This GPIB card has an IEEE-488.2 bus, which is common to the testing meters. The Labview graphical programming language was used to provide a real time display of the film resistance obtained by dividing the voltage by the current. The film resistance versus time data was stored in the hard disk instantaneously.

3.4 Experimental Setup, GC/MS and Purge & Trap Concentrator

Chromatography has been defined by the International Union of Pure and Applied Chemistry (IUPAC) as " A method used primarily for the separation of the components of a sample, in which the components are distributed between two phases, one of which is stationary while the other moves."[43]. When a gas is used as the mobile phase, it is called gas chromatography (GC). This mobile phase is forced through a stationary phase, which is fixed in place in a column or on a solid surface. The two phases are chosen so that the components of the sample distribute themselves between the mobile and stationary phase to varying degrees. Those components that are strongly retained by the stationary phase move only slowly with the flow of mobile phase. In contrast, components that are weakly held by the stationary phase travel rapidly. As a consequence of these differences in mobility, sample components separate into discrete bands, or zones, that can be analyzed qualitatively and quantitatively. Figure 24 shows the basic configuration of a gas chromatograph.

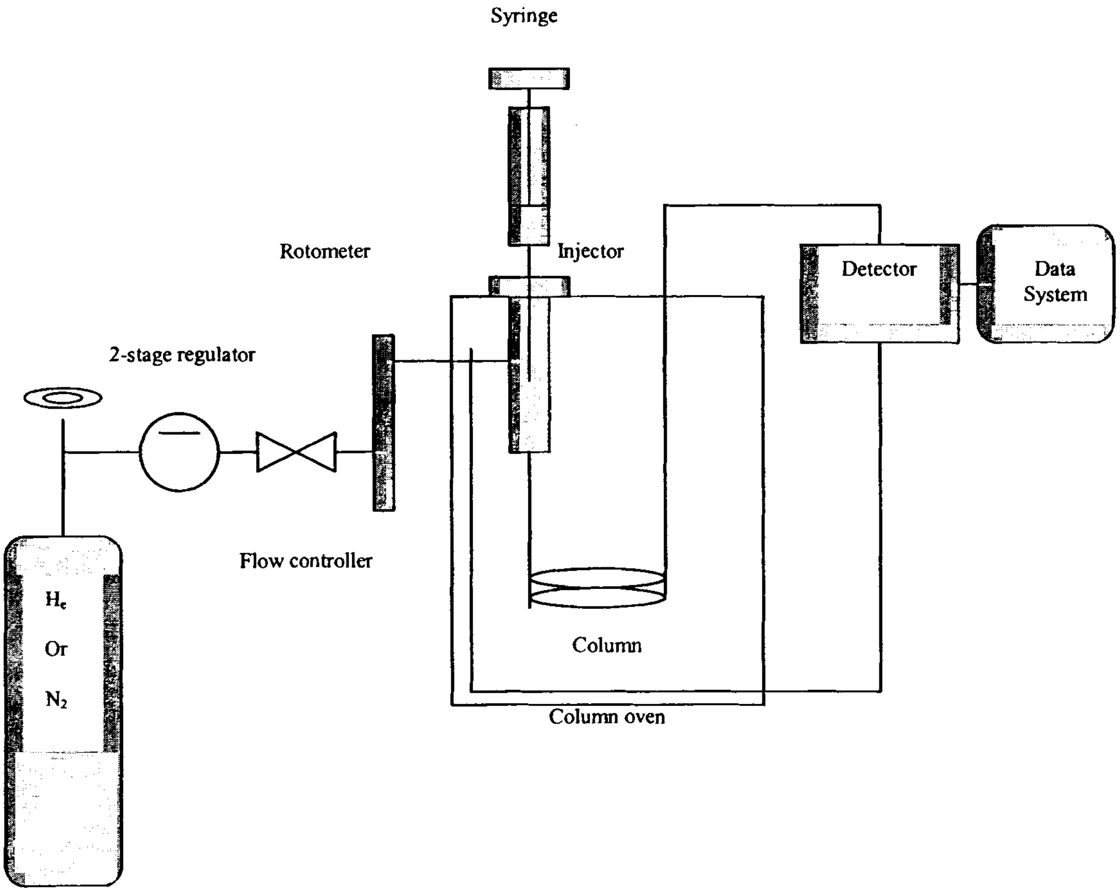

Figure 24: Gas chromatography.

Gas chromatography is often coupled with the mass spectrometry, which allows us to obtain a mass spectrum from the output of the GC. Since the flow rate from the GC columns is generally low, the column output can be fed directly into the ionization chamber of the mass spectrometer. In the jet separator, the exit gases flow through a nozzle, which increases the momentum of the heavier analyte molecules so that more of them travel in a straighter path to the skimmer. The light helium atoms, in contrast, are deflected and pumped away. A schematic of a typical MS system is shown in figure 25. The components of a specific sample can be identified by comparing the measured mass spectrum with the standard mass spectra located in a database.

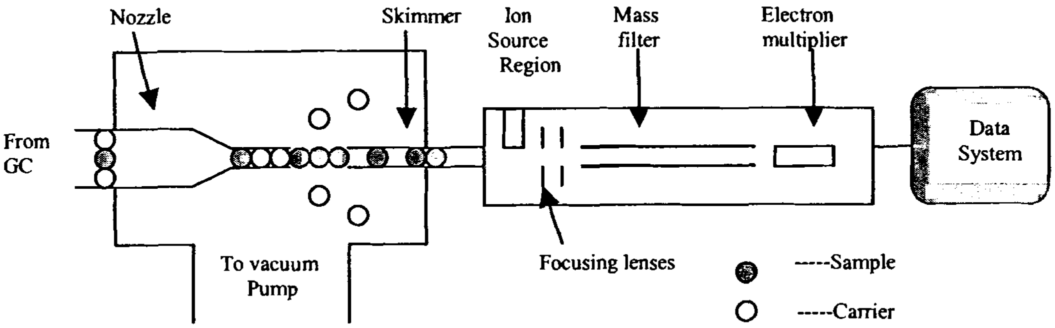

Figure 25: Mass spectrometry.

When the concentration of the sample is extremely low, the sample must be concentrated before it is injected into the GC/MS. A tekmar 3000 purge & trap concentrator was used to concentrate volatile and semi volatile organic compounds. The concentrator releases these compounds from the heated blueberry sample by extraction with a carrier gas. The compounds are absorbed on a trap column by flowing the carrier gas through the trap. The trap is then rapidly heated to desorb these compounds and introduce them into the GC column. Figure 26 shows the flow path of a purge & trap concentrator.

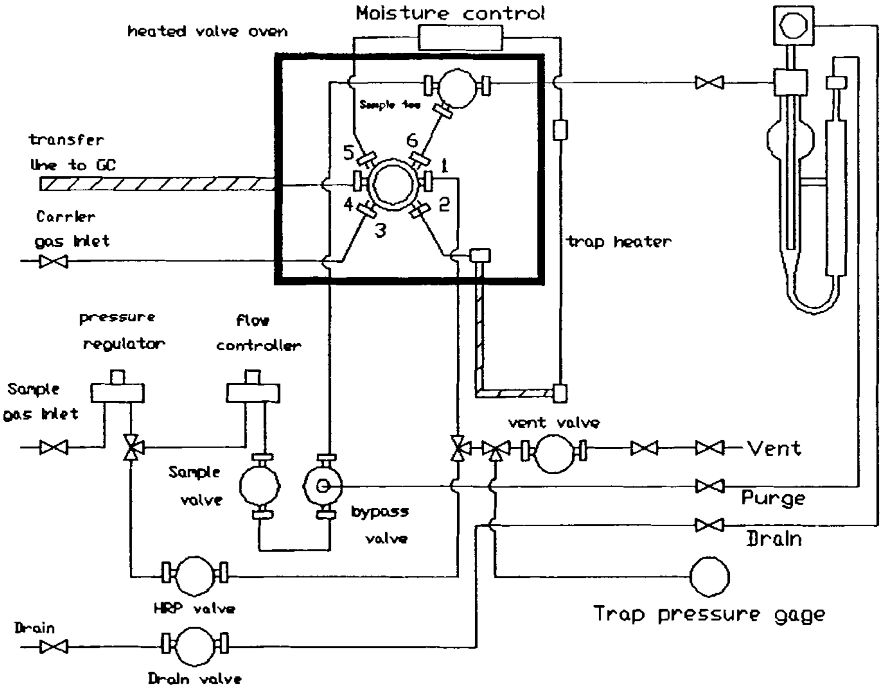

Figure 26: Tekmar 3000 flow path.

With the help of Dr. Therese Anderson, a method called Blueber.m was set up on the HP 5973 GC/MS with a 25mmx60mx0.25μm GC column. The initial parameters were:

Inlet temperature	250 °C
Initial oven temperature	150 °C
Initial oven hold time	1 minute
Final oven hold temperature	300 °C
Final oven hold time	10minutes
Oven ramp rate	10 °C/min.
Total run time	26 minutes

Carrier gas flow rate	1.2ml/min.
Splitless mode	

A tekmar 3000 purge & trap concentrator was hooked up to the GC/MS. Some typical parameters for the concentrator were as follows:

Purge time	10-30min.
Dry purge time	0min.
GC start	Des start
Cryo Focuser	Off
GC cycle time	0min.
Cryo standby	100Sec.
Cryo focus temperature	-150 °C
Inject time	1.00min.
Cryo injection temperature	180 °C
Desorb preheat	175-220 °C
Desorb time	2-6min.
Desorb temperature	175-250 °C
Sample drain	Off
Bake time	10min.
Bake temperature	250 °C

BGB on delay	2.00min.
MCS bake temperature	310 °C
Line temperature	175-250 °C
Valve temperature	175-250 °C
Mount temperature	40 °C
MCS line temperature	40 °C
Purge ready temperature	40 °C
Purge temperature	40 °C
Turbo cool temperature	-20 °C
Sample heating	On
Pre purge time	1.00min.
Pre heat time	5.00min.
Sample temperature	100 °C

4 EXPERIMENTAL RESULTS

This chapter presents the experimental results of the two kinds of prototype pesticide sensors and of measurements from the GC/MS. Therefore separate sections for the QCM, SMO and GC/MS measurements will follow. For these sections experimental data obtained from the output of the sensor was recorded during target phosmet solution injections or gas exposures. The data is graphically displayed as a function of time and also plotted such that the theories examined in chapter two can be compared to the results.

4.1 Experimental Results based on the QCM Sensing Technique

4.1.1 Water based experiments

In order to determine whether the bare QCM will sorb phosmet and what effect the change in fluid density and viscosity due to the addition of phosmet may have, the following experiment was performed. Figure 27 shows the resonant frequency of the bare QCM after 50 μl of 3.2% phosmet solution was injected into a water bath containing 66 ml of water. The resonant frequency change is only 1~2 Hz which is within the noise level. Hence, it indicates that the sensing area of bare QCM does not absorb phosmet within the detectable limit and that the phosmet solution did not have any measurable effect on the density and viscosity of the fluid.

A second experiment was performed on a PECH coated QCM to determine if methanol adsorps on PECH and what effect the fluid density and viscosity changes caused by small injections of methanol in water may have. Figure 28 shows that the resonant frequency of the PECH coated QCM after 50 μl methanol was injected into a water bath containing 66 ml of water. The resonant frequency change is only 1~2 Hz which is within the noise level. Hence, it indicates that the PECH coating does not absorb methanol within the detectable limit and that small injections of methanol cause no noticeable change in frequency due to the liquid density and viscosity change.

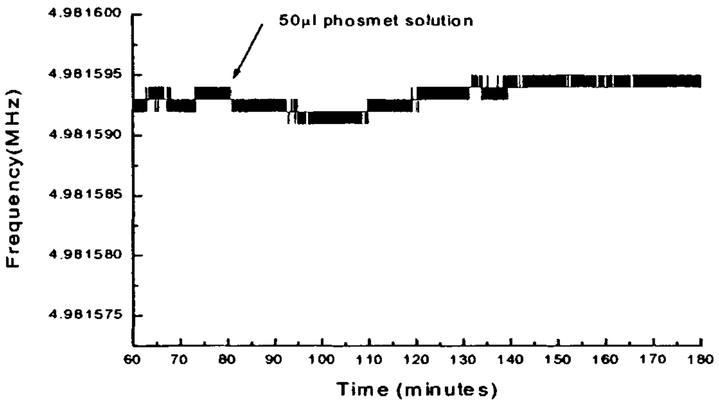

Figure 27: Resonant frequency of the bare QCM following a 50 μl of 3.2% phosmet injection to the water bath containing 66ml of water.

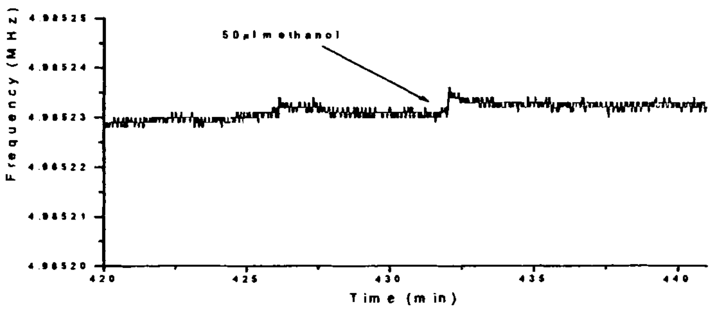

Figure 28: Resonant frequency of the PECH coated QCM following a 50μl methanol injection to the water bath containing 66ml of water.

Figure 29 shows changes in the resonant frequency of the PECH coated QCM following multiple injections of phosmet into a water bath containing 66 ml of water. As shown in the figure the size of the 3.2 % phosmet solution injections ranged from 2 to 10 μl. A 10 μl injection corresponds to a 4.7ppm concentration of phosmet in the water bath. The turnaround in the frequency shift at approximately 300 minutes is due to the saturation of the water bath with phosmet. The solubility limit of phosmet in water is 25mg/l, which in this experiment would be reached following injections of a total of 53 μl of phosmet solution into the water bath. The data indicate that during the injection process the solution first becomes supersaturated since the QCM frequency continues to decrease until a total of 75 μl have been added. At that point there was an increase in the QCM frequency, which is most likely due primarily to precipitation of phosmet from the supersatured solution causing a decrease in phosmet concentration in the solution and subsequent the phosmet desorption from the PECH film. Small changes in the density and viscosity of the fluid also occur, however the changes are not expected to have a significant effect on the QCM frequency, based on the previous results on the bare and PECH coated QCM (see figures 27 and 28). The final frequency of 4.985125 MHz is approximately equal to the frequency shift observed after 55 μl of injections or approximately 25mg/l concentration of phosmet in the water bath. Figure 30 shows the frequency shift as a function of the amount of phosmet injected into the water. The slope of the curve in figure 30 indicates that the sensitivity of this sensor is 15±2 Hz/ppm.

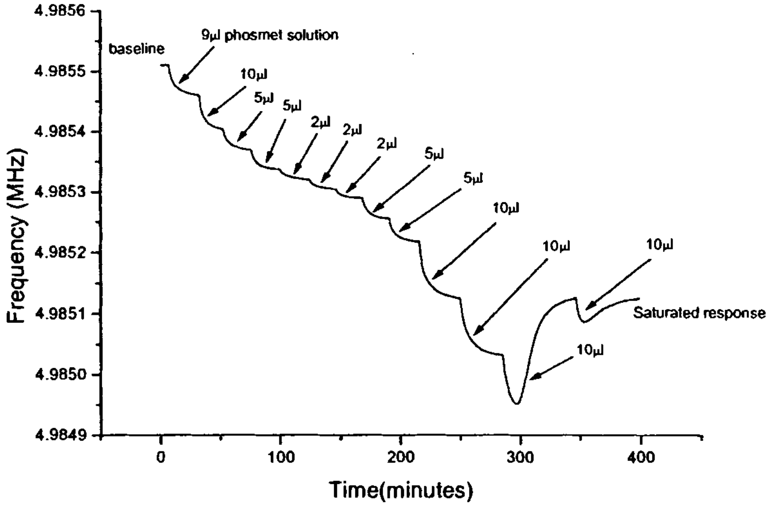

Figure 29: Changes in resonant frequency of the PECH coated QCM following a series of phosmet injections to the water bath.

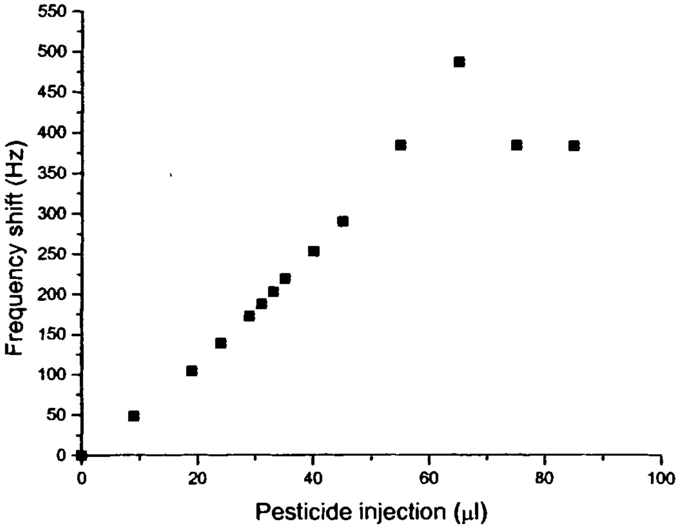

Figure 30: Net frequency shift as a function of phosmet injections from the data of Figure 29.

Figure 31 shows the results from four sets of injections of phosmet solution to the same PECH coated QCM. This PECH coated QCM was put into a small plastic box at room temperature between tests. The similar response patterns indicate good reproducibility. The data from figures 29 and 30 is the second exposure shown in figure 31. Figure 32 summarizes results for three of the sets of injections of phosmet solution shown in figure 31. Between each of the series of injections, the variation of sensitivity is less than 2 Hz/ppm. The average sensitivity is 15 ± 2 Hz/ppm. The data also shows that the maximum frequency shift of the sensor in a saturated solution of phosmet in water, 349, 383 and 342Hz respectively, is very close in these three tests. The total amount of phosmet injected into the water bath in each experimental run is 3.1, 2.5 and 2.7 mg respectively, although the solubility limit of phosmet means a maximum of 1.5mg phosmet can dissolve in 66ml water. Figure 32 also shows that the response curves are not exactly linear, increasing in slope at higher phosmet concentrations.

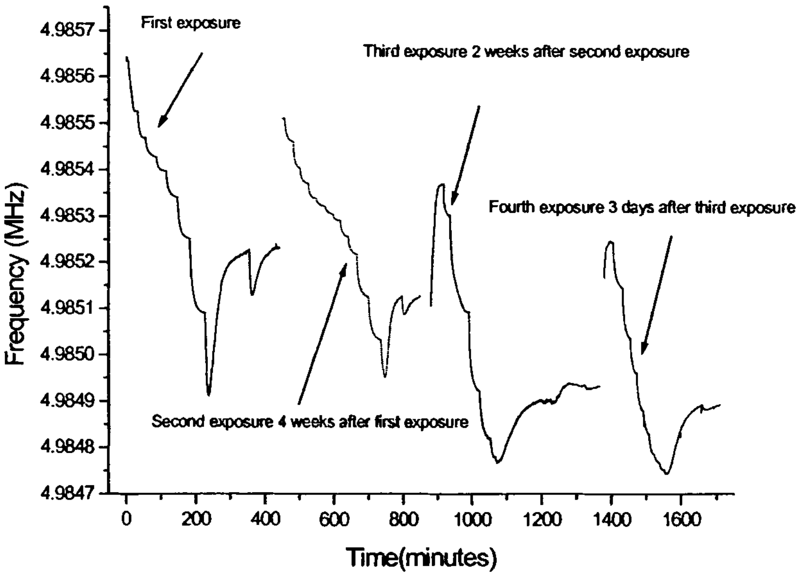

Figure 31: Results of four sets of phosmet injections to the same sensor.

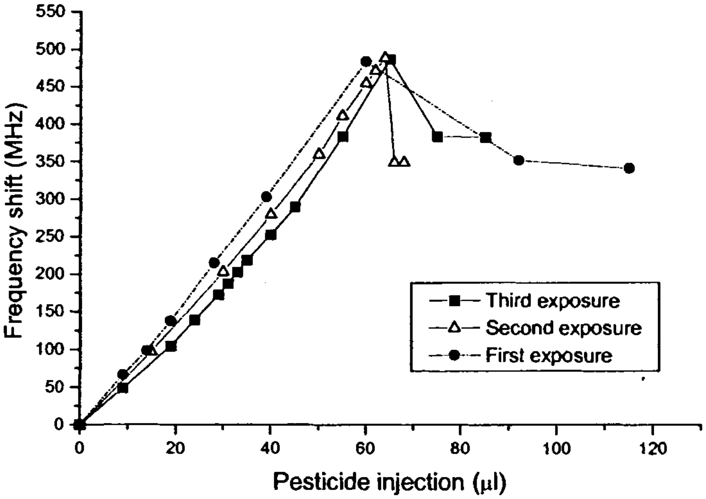

Figure 32: Results of three series of phosmet injections using the same PECH coated QCM sensor.

Martin [22] developed a relationship for the change of resonant frequency in a QCM, which has a surface mass layer and a liquid layer on the sensing surface (see figure 5 in section 2.1.4). Martin [22] modeled this sensor with an equivalent circuit called the Butterworth Van Dyke (BVD) equivalent circuit and then developed the following relation for the change in resonant frequency by both the mass and liquid loading from its value associated with the bare or uncoated QCM in air.

$$\Delta f_s = -\frac{2f_s^2}{\sqrt{\overline{\overline{C}}_{66}\rho_q}}\left[\rho_s + \left(\frac{\rho\eta}{4\pi f_s}\right)^{1/2}\right] \tag{10a}$$

The experiments relating to the addition of a 50μl phosmet solution injection to the water bath for the bare QCM (see figure 27) and 50μl methanol injection to the water bath for the PECH coated QCM (see figure 28) clearly show that the change in resonant frequency of the QCM was negligible. As a result of the measurements, it is clear that the change in liquid density and viscosity due to these injections was not sufficient to change the QCM resonant frequency in either experiment. The data also indicates that PECH does not absorb methanol. Hence, we can consider that the observed resonant frequency shifts of the PECH coated QCM in figure 30 were mainly caused by the mass loading of phosmet on the PECH coating. Equation (10a) can be reduced to equation (10b) or (1) in this case. Therefore,

$$\Delta f = -\frac{f_s^2}{N \cdot \rho_q \cdot S} M_f = -K_m M_f \,. \tag{1}$$

Where f_s is the fundamental resonance frequency of the quartz crystal, N is the frequency constant of the specific crystal cut (N_{AT}=167 KHz cm, N_{BT}=250 KHz cm), ρ_q is the quartz density (ρ_q=2.648 g cm^{-3}), S is the surface area of the deposited film which is equal to the surface sensing area of the quartz crystal, and M_f is the mass of the deposited film.

It is assumed that the PECH coating was evenly deposited on the surface of sensing electrode of the bare QCM and the absorbed phosmet was evenly distributed on the surface and the bulk of the PECH coating. Since the mass of the PECH coating and the phosmet absorbed is very small compared to the mass of the bare QCM, the change of the shear modulus and density of the bare QCM can be neglected. For a 5MHz AT-cut quartz crystal, the mass sensitivity constant, $K_m = 2.26 \times 10^{-6} f_s^2$, can be calculated as $56.5 Hz / \mu g$. The f_s in the expression for K_m refers to the series resonant frequency of the QCM when the QCM operates at the zero phase point.

However, the resonant frequency measured is based on the oscillating circuit shown in figure 18 and is not the series resonant frequency defined when the phase shift, ϕ_1, of the QCM is zero, but the resonant frequency with the phase shift of the QCM equals to $-60°$. Both Martin's equation (10a) and Kanazawa's equation (3) were derived on the basis that the QCM operates at zero phase and series resonant frequency, therefore, when $Z(\omega) = 0$ in figure 19. It is not expected that the resonant frequency when $Z(\omega) \neq 0$ would be the same. Therefore, the change in resonant frequency caused by adding a fluid to the QCM surface can not be predicted using Martin's or Kanazawa's equation. In fact Dr. Chao Zhang used the same frequency-measuring system described in figure 17 with $Z(\omega) \neq 0$ to measure the frequency shift of the standard QCM before and after it was submerged in distilled water.

Comparing the measured resonant frequency shift with the frequency shift calculated from the Kanazawa's equation (3), shows that the measured frequency shift, corresponding to the -60° phase, is 3.13 times bigger than the calculated frequency shift.

Hence, the relationship between the resonant frequency shift of QCM under mass and liquid loading need be rederived in this case. The circuit parameters of the QCM, C_0, C_1, R_1, and L_1 can be obtained at various $\omega's$ from the BVD model (see appendix C). The resonant frequency of the QCM operating in air f can be measured using the oscillating circuit. An analytical equation for the f can also be obtained from the circuit in figure 19 and expressed as follows,

$$f = F[C_0, C_1, L_1, R_1, Z(\omega)] \tag{18a}$$

Noting that $Z(\omega)$ does not change when the QCM is in water, the resonant frequency of the QCM operating in different liquids can be expressed as follows,

$$f_j = F[C_0, C_1, L_1, R_1, L_{j2}, R_{j2}, L_{j3}, Z(\omega)];\ (j = 1\mathrm{K}\ n,) \tag{18b}$$

The circuit elements L_{j2}, R_{j2} and L_{j3} can be determined at various $\omega's$ from the modified BVD model (see appendix C). The magnitude of $Z(\omega)$, $|Z(\omega)|$ can be solved in a least square sense at the phase shift $\phi_1 = 60°$. Once $|Z(\omega)|$ is known, it can be incorporated into the theory presented by Kanazawa and Martin in order to develop approporate equations for the change in resonant frequency upon liquid loading. The obvious alternative approach would be to use a QCM oscillator configuration in which $Z(\omega) = 0$. Such a system has been manufactured and is currently in use in Dr. Paul Millard's laboratory at University of Maine.

After this PECH coated crystal was rinsed and put into ambient for several days, another experiment was performed where the water bath containing 110 ml of water was flushed with 600 ml of distilled water following a series of 15 and 20 μl phosmet solution injections. Figure 33 shows the results. A similar saturation effect due to the solubility limit of phosmet in water was observed. In addition the data shows that the operating frequency of phosmet-loaded QCM can be returned nearly to its original value after repeated flushing with de-ionized (D.I.) water. This shows that the phosmet is weakly bound to the PECH and will return to the surrounding solution as the concentration of phosmet is decreased. This conclusion also can be supported by the experimental results in figure 31. In figure 31, the PECH coated QCM was rinsed under D.I. water and put into ambient for several days after one experiment was finished. The baseline frequencies of the PECH coated QCM in the last three experiments approached the original value of previous experiment after being submerged in fresh distilled water for the next experiment. Although the baseline of the QCM submerged in water will vary somewhat due to differences in water temperature, these experimental results still can support the conclusion that the phosmet is weakly bound to the PECH and will return to the surrounding solution after being washed in D.I. water.

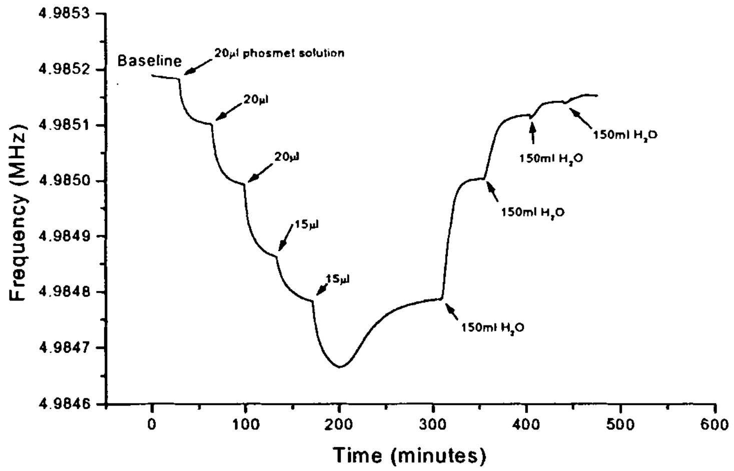

Figure 33: Changes in resonant frequency of the PECH coated QCM following a series of phosmet injections to the water bath followed by flushing with distilled water.

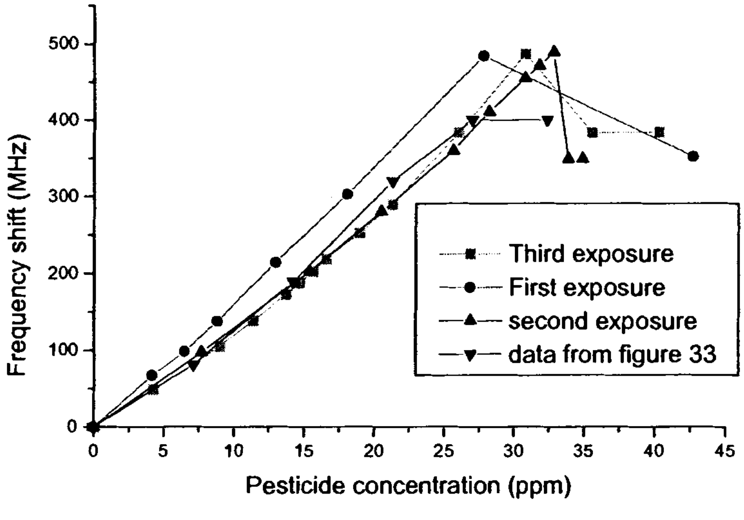

Figure 34: Net frequency shift of data from figure 33 as a function of phosmet concentration together with data from figure 31.

Figure 34 shows the frequency shift as a function of the phosmet concentration in the water bath from the data of figure 33 along with the data from figure 31. The difference between the experiments in figure 33 and figure 31 is that there is 110ml of water in the bath instead of 66ml water. This figure confirms that the sensor is responding to the concentration of phosmet in water and not the amount of phosmet solution added into the beaker. In addition to similar slopes, the final frequency shifts are almost the same, around 390Hz, corresponding to the 25ppm saturated concentration of phosmet in the water bath. Since the response curves in figure 33 are not exactly linear, with increasing in slope in solutions at higher phosmet concentrations, they can be fit to a quadratic function. Using three pair points in figure 33, which are (0Hz, 0ppm), (70Hz, 5ppm) and (390Hz, 25ppm), the quadratic function can be expressed as,

$$\Delta f_s = 0.078C_p^2 + 13.61C_p, \tag{19}$$

where C_p is the phosmet concentration in the liquid in units of ppm.

The above experiments are consistent with a hydrogen-bonding interaction between PECH and phosmet described in 2.1.5. This interaction is due to the fact that the OCH_3 parts in phosmet have strong hydrogen bond basic properties and PECH has moderate hydrogen bond acidic properties [23].

4.1.2 Experiments using blueberry juice

The experimeantal results in section 4.1.1 clearly confirm the sensitivity of the PECH coated QCM sensor under exposures of the phosmet solution in D.I. water. Since the purpose of this thesis is to develop a prototype sensor to detect the phosmet residue on blueberries, the above experiments need to be repeated by using blueberry juice instead of D.I. water. Figure 35 shows changes in the resonant frequency of the PECH coated QCM following multiple injections of the 3.374% phosmet solution into a beaker containing 58.2g of organic (non phosmet treated) blueberry juice. As shown in this figure the size of the 3.3% phosmet solution injections ranged from 10 to 50 µl. A 10 µl injection corresponds to a 5ppm concentration of phosmet in the organic blueberry juice. Saturation phenomena can be observed, similar to which took place in the water bath. The turnaround in the frequency shift at approximately 350 minutes is due to the saturation of the organic juice with phosmet. Similar to the curve in figure 29, the data indicates that during the injection process the solution first becomes supersaturated since the QCM frequency continues to decrease until a total of 164 µl have been added. At that point there was an increase in the QCM frequency indicating a decrease in phosmet concentration likely due to phosmet precipitation from the supersaturated solution and phosmet desorption from the PECH film. The final frequency of 4.983751 MHz is approximately equal to the frequency shift observed after 94 µl of injections or approx. 39ppm concentration of phosmet in the organic blueberry juice. The observed solubility limit of phosmet in this organic juice is 39mg/l, which is higher than 25mg/l limit in water.

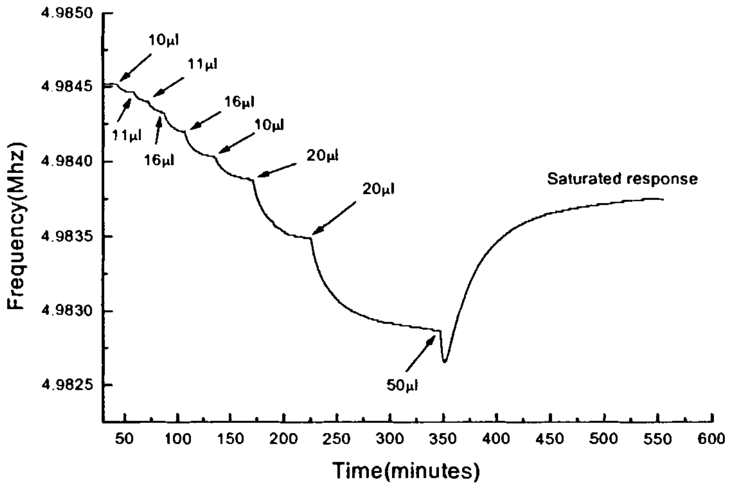

Figure 35: Changes in resonant frequency of the PECH coated QCM following a series of phosmet injections to organic blueberry juice.

Figure 36 shows the frequency shift as a function of the phosmet concentration in the organic blueberry juice from the data of figure 35. It can be observed that the frequency shift is not a linear function but a parabolic function of the phosmet concentration. In figure 35, when the phosmet concentration in the organic blueberry juice reached 32ppm, the resonant frequency shift was 489Hz. By comparison, when the phosmet concentration in the D.I. water reached 28, 32 and 31ppm (figure 34 first, second and third exposure), the frequency shifts were 484, 489 and 487 Hz respectively. It is obvious that the slope of frequency shift curve in figure 36 at concentration less than 32ppm is very close to those slopes in figure 34. The data also indicates that the phosmet still can be sorbed on the PECH coating even in the presence of blueberry juice. Although some reacting sites (cavities) of the PECH coating are likely occupied by organic compounds from the blueberry juice, there is still good sensitivity of the PECH film to phosmet.

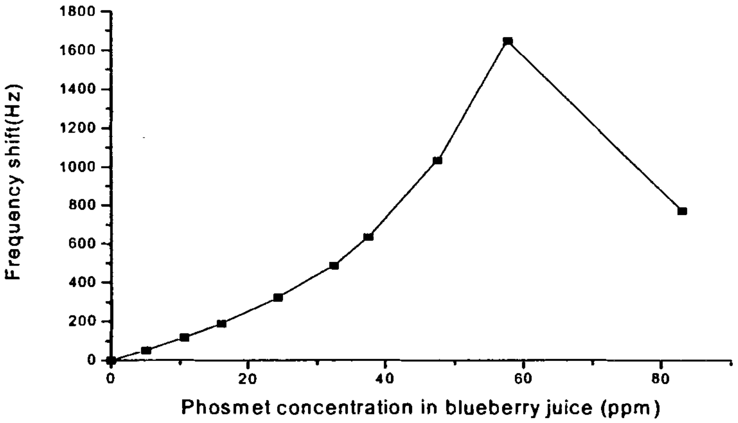

Figure 36: Net frequency shift as a function of phosmet concentration from the data of figure 35.

Figure 37 shows the summary of the results for figures 33 and 35. A 1.5KHz resonant frequency shift was observed after the QCM was coated with PECH due to the effect of the mass loading. 700Hz and 140Hz resonant frequency shifts were obtained after this PECH coated QCM was submerged into organic blueberry juice and D.I. water respectively. These shifts are due to the effect of liquid loading and possible organic sorption on the PECH coated surface of the QCM. The 560 Hz difference between the two values is primarily due to the organic sorption on the sensing surface of the QCM and the difference in density and viscosity between these two fluids. After a series of phosmet injections into the above two fluids, a 383Hz frequency shift was obtained for the saturated phosmet concentration in distilled water (25mg/l) and 771Hz for the saturated phosmet concentration in organic blueberry juice (39mg/l). Since only 0.14g of phosmet solutions were injected into 58.2g of organic blueberry juice, the expected viscosity and density change of the juice should be very small and can be neglected. Therefore, these shifts are due to the effect of mass loading after the saturated phosmet concentration in the above solutions was reached. Using equation (19), the expected frequency shift in organic blueberry juice can be predicted as 649Hz, which is less than the experimental result 771Hz. This may due to that equation (19), which was derived by only fiting 3 points, is not very exact. Another possible explanation for the 122Hz difference is the shape of adsorption isotherm (see section2.1.5). In low phosmet concentration region, the response curve was caused by monomolecular adsorption described by the Langmuir adsorption isotherm. When the phosmet concentration in solution reaches its saturation point, the multimolecular adsorption dominates the adsorbing mechanism and the shape of response curve became parabolic as described in BET adsorption isotherm. The exact reasons of above parabolic phenomena need further explorations in the future.

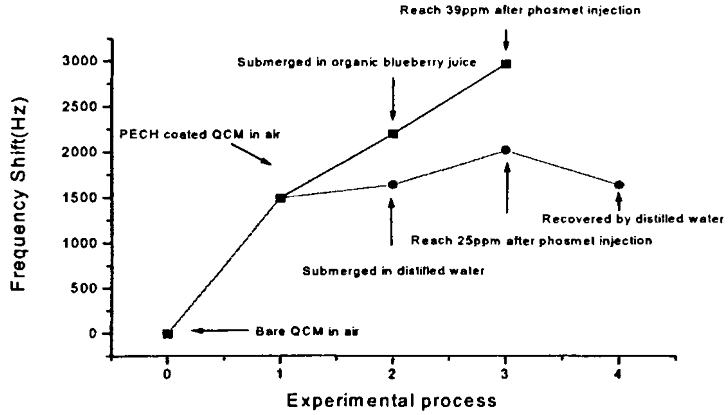

Figure 37: Summary of experimental results of figure 33 and 35.

The previous experiments have confirmed that the PECH coated QCM is sensitive to the phosmet, which has been added to organic blueberry juice. The next step will be to determine the difference in resonant frequency change of the same

PECH coated QCM in D.I. water to the flushing of the phosmet treated blueberry juice, which is obtained from blueberries that have been treated with phosmet in the field and organic blueberries juice described in section 3.2.1 respectively. These experiments will provide information on whether the PECH coated QCM can detect the phosmet in the phosmet treated blueberry juice.

Refering to figure 17, when the resonant frequency of the PECH coated QCM reached it baseline in water, valve A was totally opened and the 200ml treated blueberry juice in beaker A was introduced into the 110ml water bath. Valve B was adjusted manually to maintain the liquid level in the water bath at a constant level as the blueberry juice flowed into the beaker. When beaker A was emplied, valve B was closed until the frequency reache its baseline in treated blueberry juice. Then another 500ml of water was put into beaker A and introduced into the water bath in the same way until the frequency reached its baseline in water again. The same process was repeated for organic blueberry juice to obtain the results shown in figure 38.

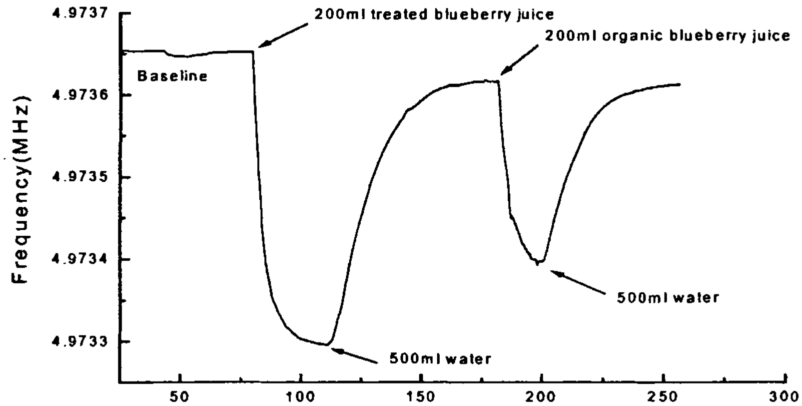

Figure 38: Changes in resonant frequency of the PECH coated QCM following flushing with treated and organic blueberry juice.

In figure 38, the baseline of the resonant frequency in distilled water is 4.973655MHz and the observed frequency shift after being flushed with 200ml of treated blueberry juice is 360Hz. The baseline increased back to 4.973615MHz after being flushed by 500ml water. Similar phenomena occurred when the water bath was flushed with 200ml organic blueberry juice, but the frequency shift is only 217Hz and the baseline returned to 4.973615MHz after being flushed with another 500ml water.

Since it has been previously shown that fluid density and viscosity changes due to phosmet injection to D.I. water does not result in any significant frequency change (see figure 27), it is interesting to investigate the shift of 143 Hz between exposures to organic and treated blueberry juice. If this difference was due to mass loading of phosmet, it would corresponding to about 12ppm of phosmet concentration based on the data of figure 36. However, the maximum possible phosmet concentration of the treated blueberry juice was 2.75ppm (see section 3.2.1), hence a maximum of only 38 Hz frequency shift can be expected based on figure 36. Therefore, the difference in the two frequency shifts, 143Hz, between the treated and organic blueberry juice is most likely caused by both differences in mass loading of the PECH film and the differences in the liquid properties ($\rho\eta$) of the treated blueberry juice and organic blueberry juice. Measuring resonant frequency shifts with a single sensor isn't possible to separate these two effects.

Based on the previous discussion in section 2.1.4, the resonant frequency change due to mass loading could be differentiated from liquid loading using a differential setup, if the resonant frequency changes of the PECH coated QCM and bare QCM caused by the changes of the liquid density and viscosity are the same. We can put a PECH coated QCM and a bare QCM into the treated blueberry juice sequentially and measure their resonant frequencies. The net frequency change caused by mass loading can be obtained by subtracting the frequency shift of the bare QCM from the PECH coated QCM. Figure 39 and 40 show the results of an experiment where a PECH coated crystal and a bare crystal were placed sequentially in a water bath containing 110ml of water and were flushed with 150ml treated blueberry juice and 500ml water. The experimental process is the same as the process described for figure 38.

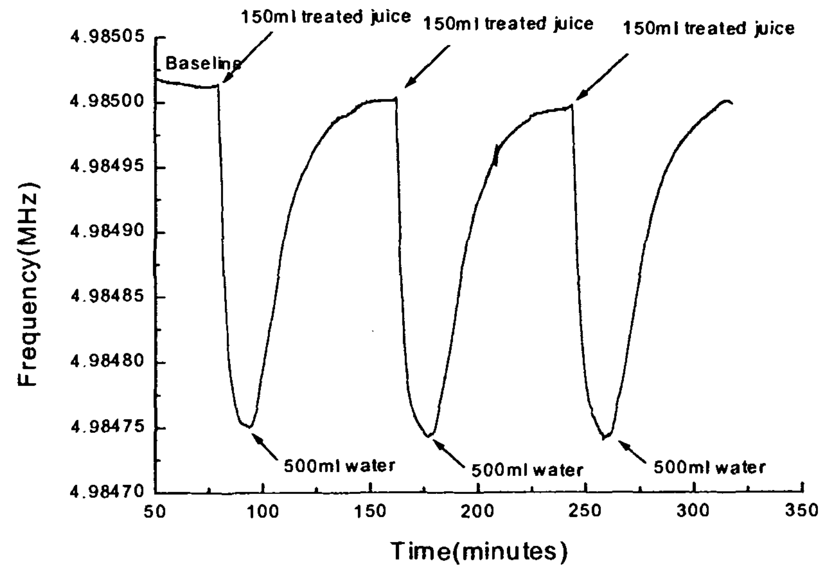

Figure 39: Changes in resonant frequency of the PECH coated QCM following a series of flushings with treated blueberry juice.

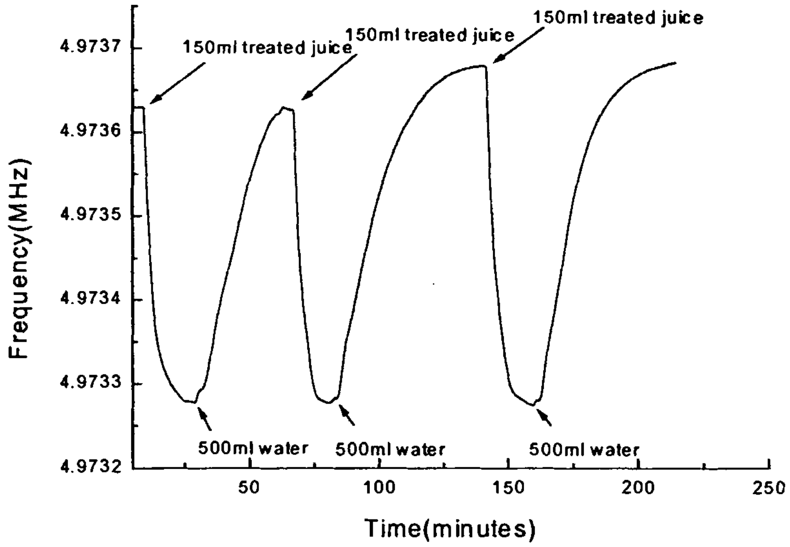

Figure 40: Changes in resonant frequency of the bare QCM following a series of flushing with treated blueberry juice.

Figure 41shows the resonant frequency shift of the PECH coated and bare QCM from the data in figures 39 and 40. The results on PECH coated QCM indicate frequency shifts of about 275Hz which is less than the 360Hz shift shown in figure 38, this is expected since only 150ml of treated blueberry juice was added in the experiment whose results are shown in figure 39. The resonant frequency shift for the bare QCM is, however, 120 Hz larger than that for the PECH coated QCM.

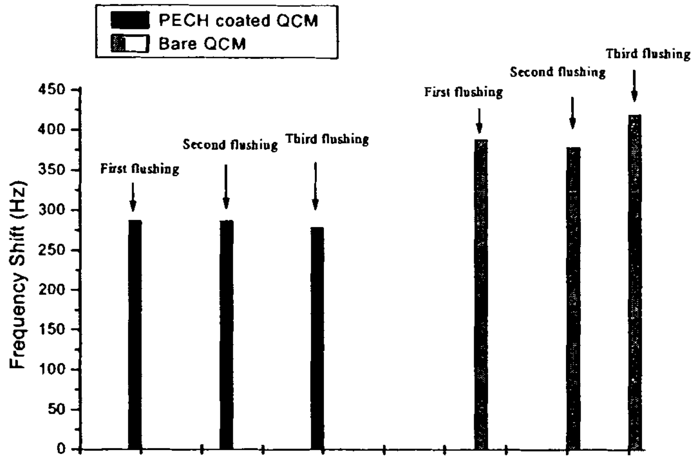

Figure 41: Net frequency shift of bare and PECH coated QCMs following flushing with treated blueberry juice.

Since the blueberry juice sample was obtained by washing and stirring the frozen blueberries, a large quantity of various organic compounds can exist in the blueberry juice, such as 2-methyl-butanoic-acid, 4-vinyl-phenol [45]. Although the sensing area of the bare QCM does not absorb phosmet within the detectable limit (see figure 27), the gold electrode of the QCM, may absorb other organic compounds [46,47]. Hence the other organic compounds absorbed on gold-coated quartz may result in the frequency shift of bare QCM being larger than the frequency shift of the PECH coated QCM in figure 41.

As we know the measured sensitivity of PECH coating is 15Hz/ppm and the maximum phosmet concentration of the treated juice is 2.75ppm (see section 3.2.1), hence the expected maximum frequency shift caused by phosmet loading could be predicted based on figure 36 as 38Hz. Considering the loss of phosmet during the sample preparation period (see figure 15), the practical frequency shift caused by phosmet loading could be much less than 38Hz. On the other hand, the hydrogen bonding acidic property of PECH means it selectively sorbs compounds with complementary properties [23] such as phosmet, hence the classes of analytes absorbed on PECH coated QCM may be less than the bare QCM. This also could result in the amount of mass absorbed on the bare QCM being bigger than the amount of mass absorbed on the PECH coated QCM, and the 120Hz of frequency shift for PECH coated QCM being less than the bare QCM in treated blueberry juice. Whether the sensing area of bare QCM sorbs the compounds in the blueberry juice needs to be verified qualitatively and quantitatively through other techniques, such as surface plasma adsorption in the future.

If all the organic compounds that can absorb on Au are removed from the blueberry juice before the frequency measurement, the difference of frequency shifts between PECH coated QCM and bare QCM in treated blueberry juice would measure the concentration of phosmet. Those organic compounds can be removed by adding some chemicals in to the blueberry juice before frequency measurements are performed. A detailed sample preparation process was presented by Lixin Tiann in her master thesis [48]. She blended 50g treated blueberry with 100ml methanol for 2 minutes followed by vacuum filtration and evaporation. The concentrated filtrate was added to a separatory funnel containing HPLC grade water followed by 50 ml methylene chloride. The methylene chloride layer was passed through sodium sulfate. After another 30ml methylene chloride reextraction, all the extracts were combined and evaporated to dryness at 35 °C. The residues were dissolved in 3ml of methanol. Although the above process is very complicated, phosmet solution without other organic compounds from blueberry juice can be obtained, which is similar to the solution used in figure 29. However, the process described above is very complicated and not practical for a phosmet sensor. Another possible approach could be using a specific filter for the sensor, which can only absorb phosmet molecules and desorbs the molecules absorbed to increase the concentration of the testing sample. It may be possible to use one kind of column within liquid chromatography as this type of specific phosmet filter.

4.2 Experimental Results using SMO Sensing Technique

Figure 42 shows the resistance change of a SMO film after series exposures of phosmet gas from the positive pressure gas delivery system. The film under test was a 500Å thick WO_3 film doped with 15Å gold maintained at a temperature of 350 °C. The flow rate of the system was 12.8 sccm and the carrier gas was compressed air at 50% humidity. The Oven temperature was 50 °C to increase the vapor pressure of the phosmet. This data curve indicates that the resistance of the film was decreased when phosmet gas was introduced in to the testing chamber and the response time, which is defined as the time it takes the film to reach 90% of its steady state value after the introduction of the phosmet gas, is 15 minutes. The magnitude of the first response is 15 KΩ, and there was no visible resistance change when phosmet gas was introduced into the sensor chamber after six exposures.

Figure 43 shows the result of a test of another gold doped WO_3 film, which has a similar response to phosmet as the film in figure 42. The experimental parameters in the test, such as temperature, humidity and flow rate were the same as those in figure 42. Compared to figure 42, the data shows that the maximum magnitude of response is around 8KΩ and the response time is still 15 minutes.

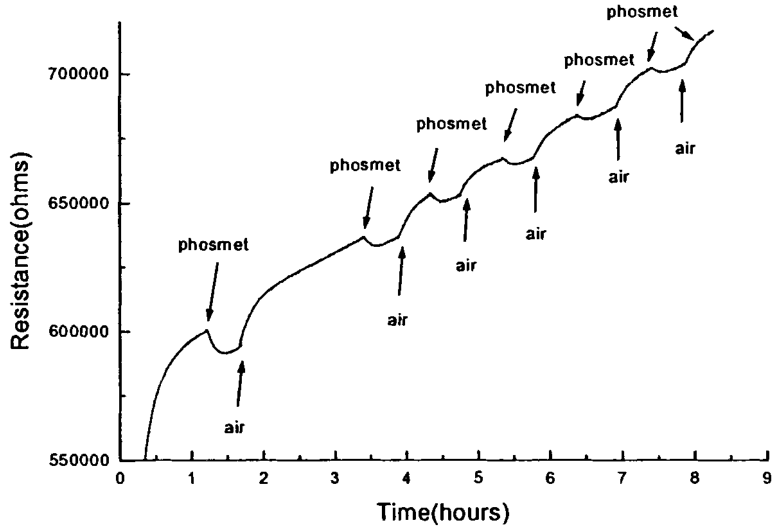

Figure 42: Changes in resistance of WO_3 gold doped film following a series of phosmet gas exposures.

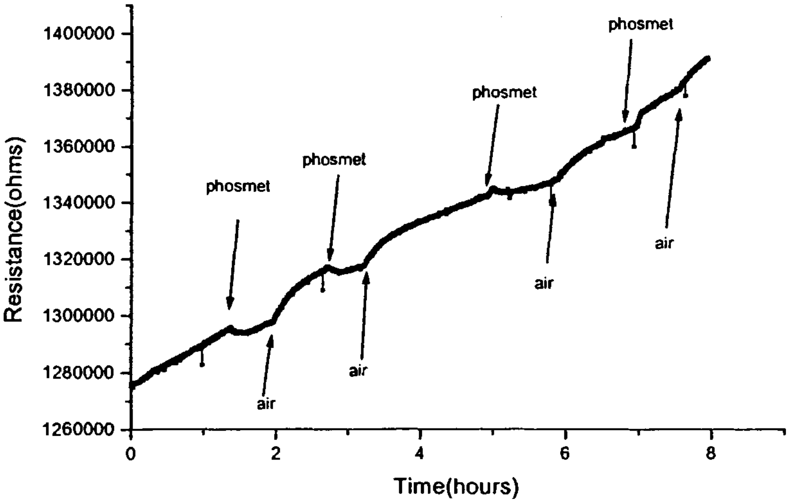

Figure 43: Results from another gold doped WO_3 sensor under the same experimental parameters.

Figure 44 shows the resistance shift on exposure to phosmet as a function of exposure number. The data shows a decrease in sensitivity of the WO_3 gold doped films with continuing exposures to phosmet gas. The similarity of the response and of poisoning phenomena between figure 42 and 43 indicates a good reproducibility between the two films.

The poisoned films were exposed to phosmet gas again at various other operating temperatures, no conductivity change was observed. The poisoned films were then annealed in clean carrier gas at 500°C for 24 hours and phosmet gas was introduced in to the testing chamber again, there was no resistance change observed for either film at 350°C. Figure 45 shows the result of the film in figure 42 and indicates that the bonds between the film and phosmet gas (or its break down components) are too strong to be broken by heating the film to 500°C.

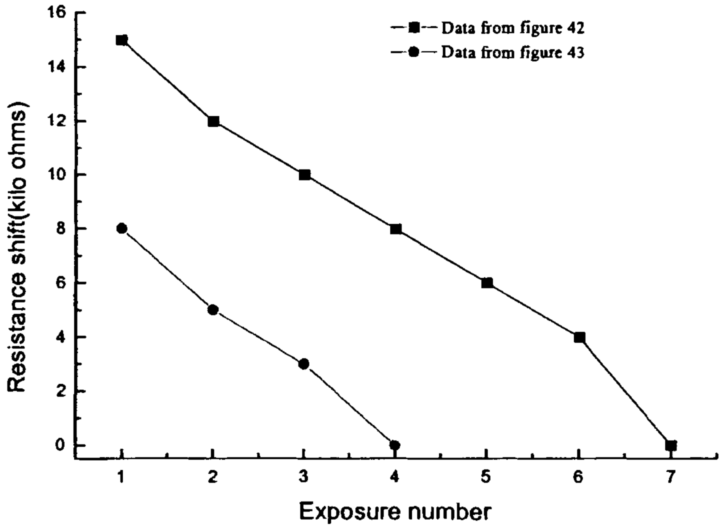

Figure 44: Net resistance shifts as a function of the number of phosmet gas exposures data from figures 42 and 43.

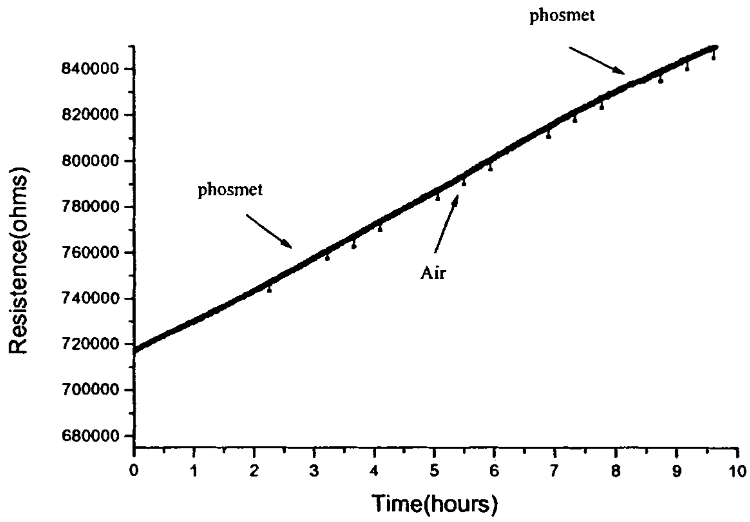

Figure 45: Results from poisoned gold doped WO_3 sensor in figure 42 under the same experimental parameters.

The above figures show an increase in the conductivity of the WO_3 gold doped film on phosmet exposure, this may due to the fact that the film was reduced by the phosmet gas. The phosmet molecule contains sulfur and sulfur is a well-known poison in catalysis [49]. Therefore, it is possible that the poisoning effect of the phosmet gas exposures to the gold doped WO_3 was due to the blocking of surface lattice oxygen by sulfur preventing the WO_3 from being further reduced by phosmet gas.

Figures 46~50 show the results from a 500Å pure WO_3 film without catalyst at 200~400 °C. The order of the experiments is 350 °C, 300 °C, 250 °C, 200 °C, 400 °C. The flow rate of the system is 15 sccm, the carrier gas is compressed air with 50% humidity, and the oven temperature was 50 °C. In figure 49, the sensitivity of this pure WO_3 film became decreased after phosmet gas exposures. Figure 51 shows the sensitivity of this pure WO_3 film as a function of temperature. The data indicates that interaction between the pure WO_3 and the phosmet gas is temperature dependent and the optimum film temperature with 50% humidity and 15sccm flow rate could be at 350 °C. The data also indicates the big sensitivity drop from 350 °C to 400 °C may due to the possible poison phenomena following the order of experiments, hence, the optimum film temperature could be higher than 350 °C and may have affected the shape of the curve in figure 50. Compared with figure 42, the sensitivity of the pure WO_3 film at 350 °C is much greater than gold doped WO_3 film and the response time is about two hours, which is much longer than the gold doped WO_3 film. This is likely due to the fact that the gold works as a catalyst to speed up the reducing reaction between the film and phosmet. For the 500Å pure WO3 film, it takes more time to reach the equilibrium between bulk oxygen and ambient oxygen. Because phosmet is thermally unstable and will totally decompose above 200 °C, the WO_3 film at 350 °C was likely reduced by its break down components such as H_2S.

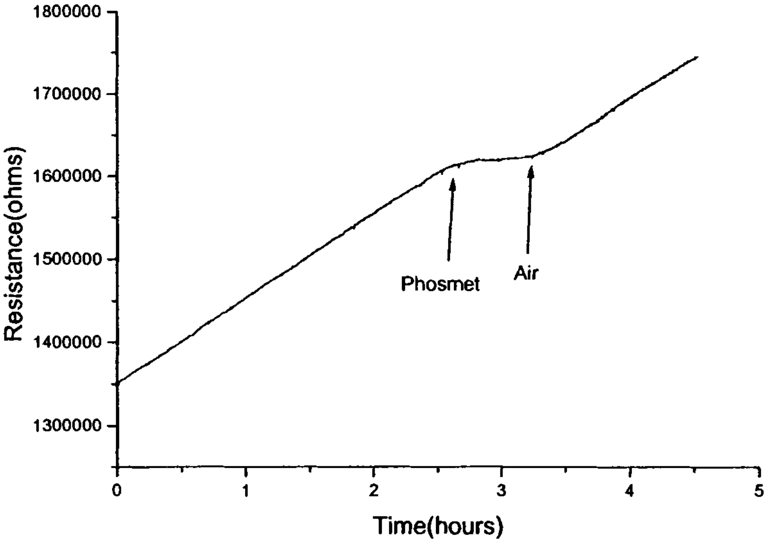

Figure 46: Changes in resistance of a pure WO_3 film following a series of phosmet gas exposures at 200 °C.

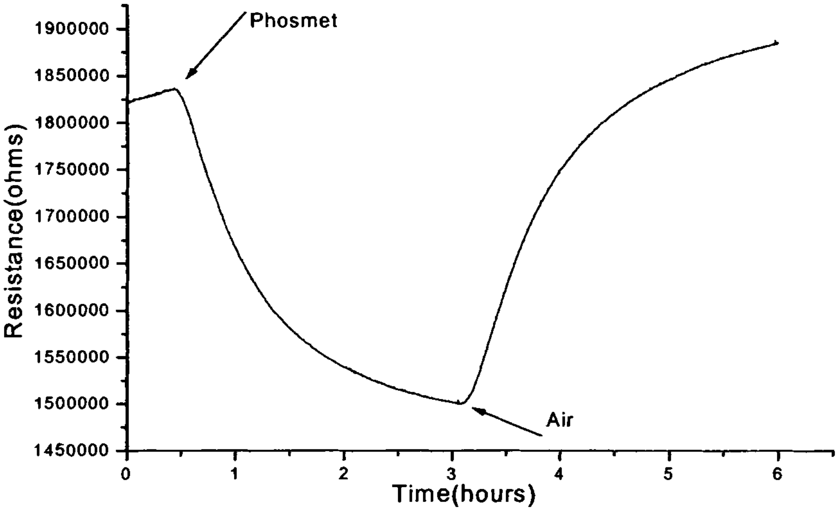

Figure 47: Changes in resistance of a pure WO_3 film following a series of phosmet gas exposures at 250 °C.

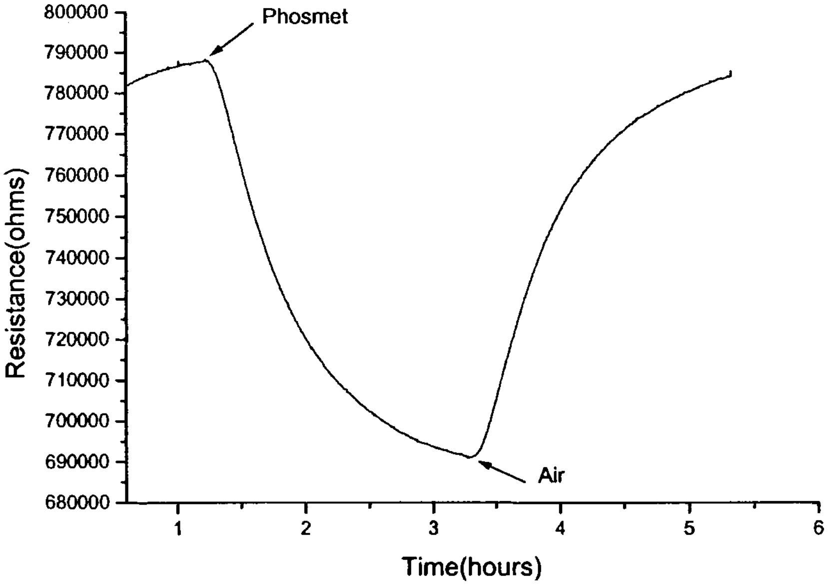

Figure 48: Changes in resistance of a pure WO_3 film following a series of phosmet gas exposures at 300 °C.

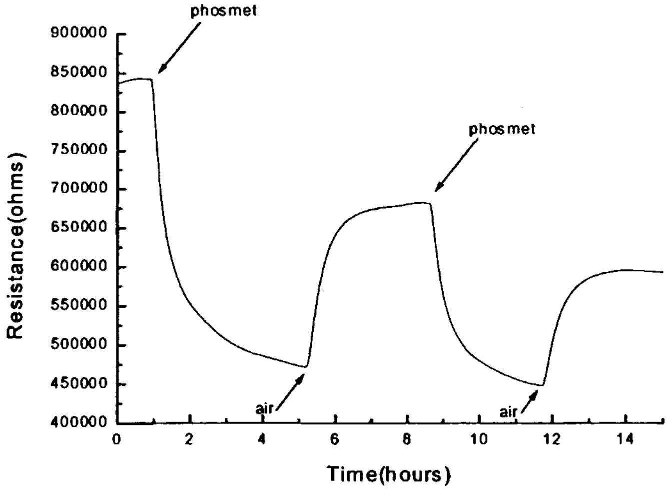

Figure 49: Changes in resistance of a pure WO_3 film following a series of phosmet gas exposures at 350 °C.

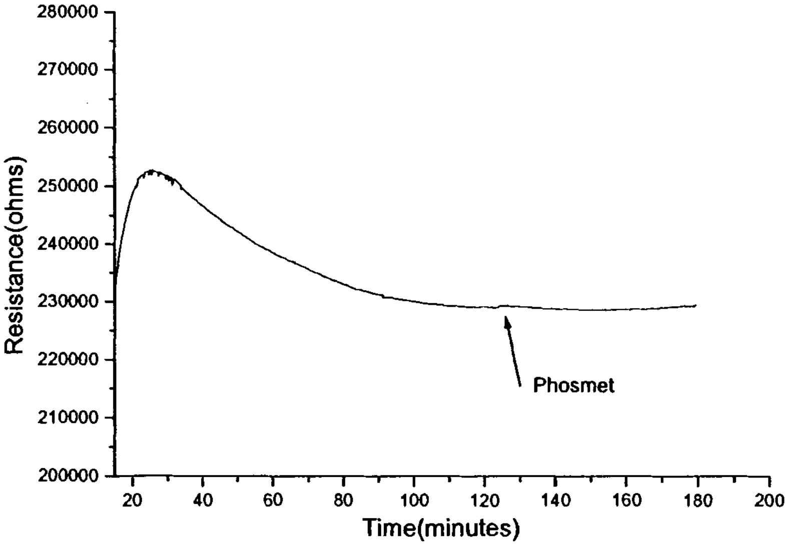

Figure 50: Changes in resistance of a pure WO_3 film following a series of phosmet gas exposures at 400 °C.

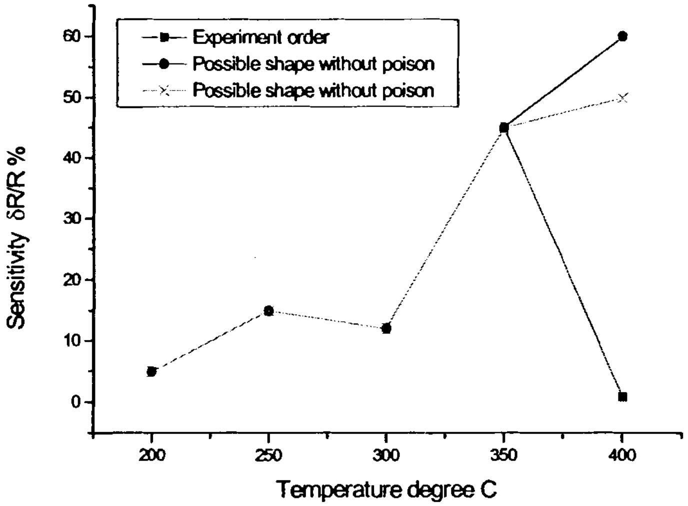

Figure 51: Sensitivity of the same pure WO_3 film versus film temperature.

With the help of Dr David Frankel, the surfaces of some of the sensors were analyzed by using Auger electron spectroscopy (AES). The use of AES for the chemical analysis of surfaces is based on the Auger process. When a core level of a surface atom is ionized by an impinging electron beam, the atom may decay to a lower energy state through an electronic rearrangement, which leaves the atom in a doubly ionized state. The energy difference between these two states is given to the ejected Auger electrons, which will have a kinetic energy characteristic of the parent atom. When the Auger transitions occur within a few angstroms of the surface, the Auger electrons may be ejected from the surface and give rise to peaks in the electron energy distribution function. The energy and shape of these Auger features can be used to identify the composition of the solid surface [50]. Because the Auger peaks are superimposed on a rather large continuous background, they are more easily detected by differentiating the energy distribution function N (E). Thus Auger data is conventionally presented in form of the derivative function dN(E)/dE.

Figure 52 shows the Auger spectrum of an untested sample of gold doped WO_3. Figure 53 shows the Auger spectrum of the gold doped WO_3 film following the tests shown in figure 42. Figure 54 shows the standard Auger spectrum of sulfur. Comparing the above three figures, a peak at 152ev in figure 53 indicates that there is some sulfur accumulated on the surface of the poisoned WO_3 film. Thus the data supports the assumption that the poisoning effect observed with the gold doped WO_3 film was due to the blocking of surface lattice oxygen by sulfur.

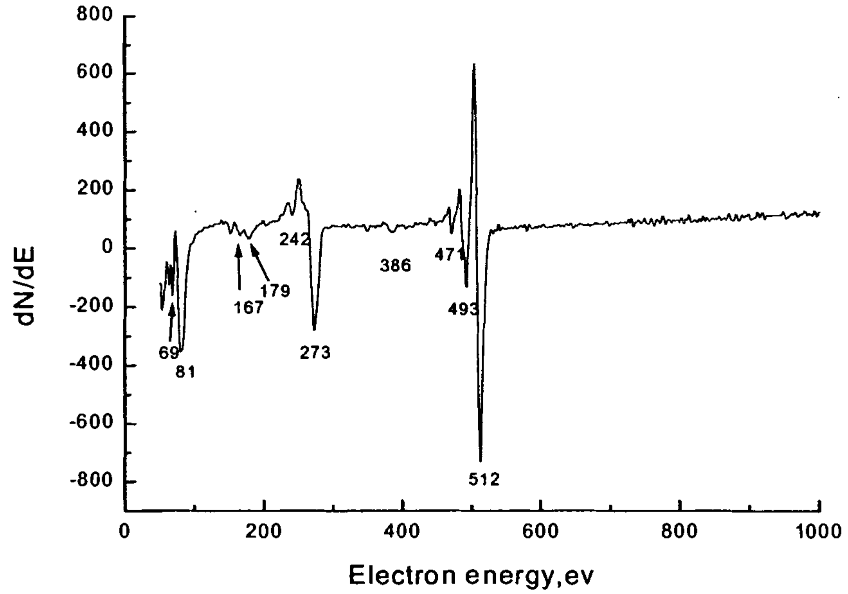

Figure 52: Auger spectrum from an untested gold doped WO_3 film.

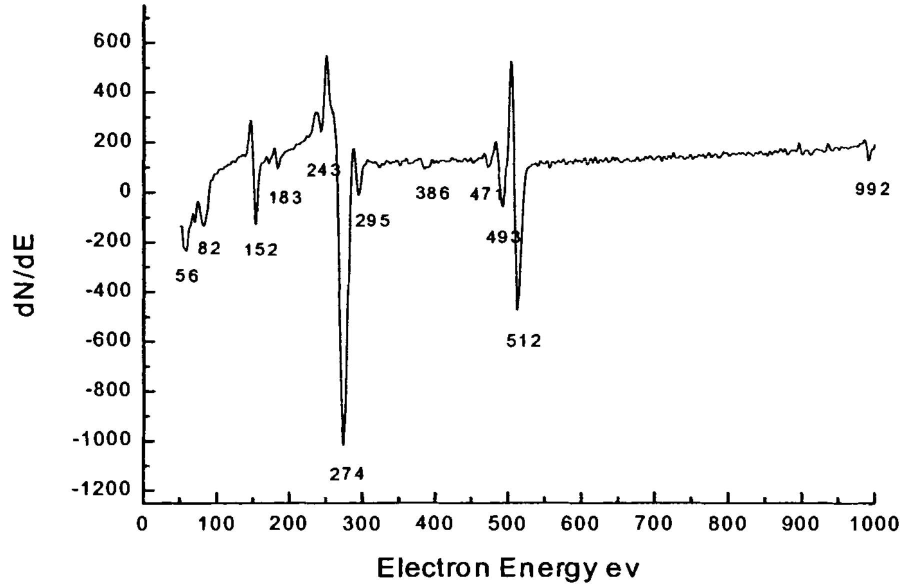

Figure 53: Auger spectrum from the gold doped WO_3 following tests shown in figure 42.

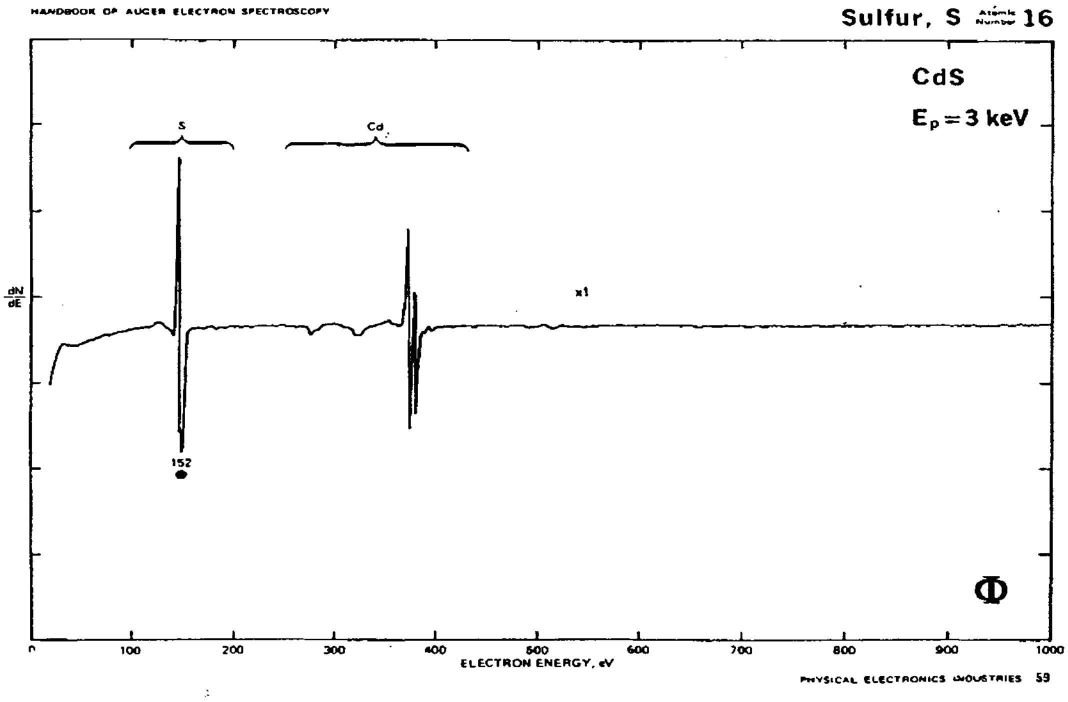

Figure 54: Standard Auger spectrum of sulfur.

4.3 Experimental Results based on GC/MS and Purge & Trap

The GC/MS was used to detect phosmet dissolved in organic solvent, the phosmet residues on blueberries and also to get knowledge of possible interferent molecules present in the blueberries. The GC/MS was also used to detect phosmet and its break down compounds from headspace samples. A purge & trap concentrator was hooked up to the GC/MS to collect and concentrate the phosmet residue on the surface of the blueberry samples and make it detectable by GC/MS.

Figure 55 shows the GC/MS result from 2μl 100ppm phosmet solution as a function of time. This phosmet sample was injected into column of the GC/MS automatically by the GC/MS instrument itself. The retention time of phosmet is around 17 minutes and is confirmed by the presence of mass 317 at this retention time. Figure 56 shows the standard mass spectrum of phosmet in the database of the GC/MS. The similarity between the mass spectrum in figure 55 and 56 indicates that phosmet dissolved in organic solvent can be detected by GC/MS.

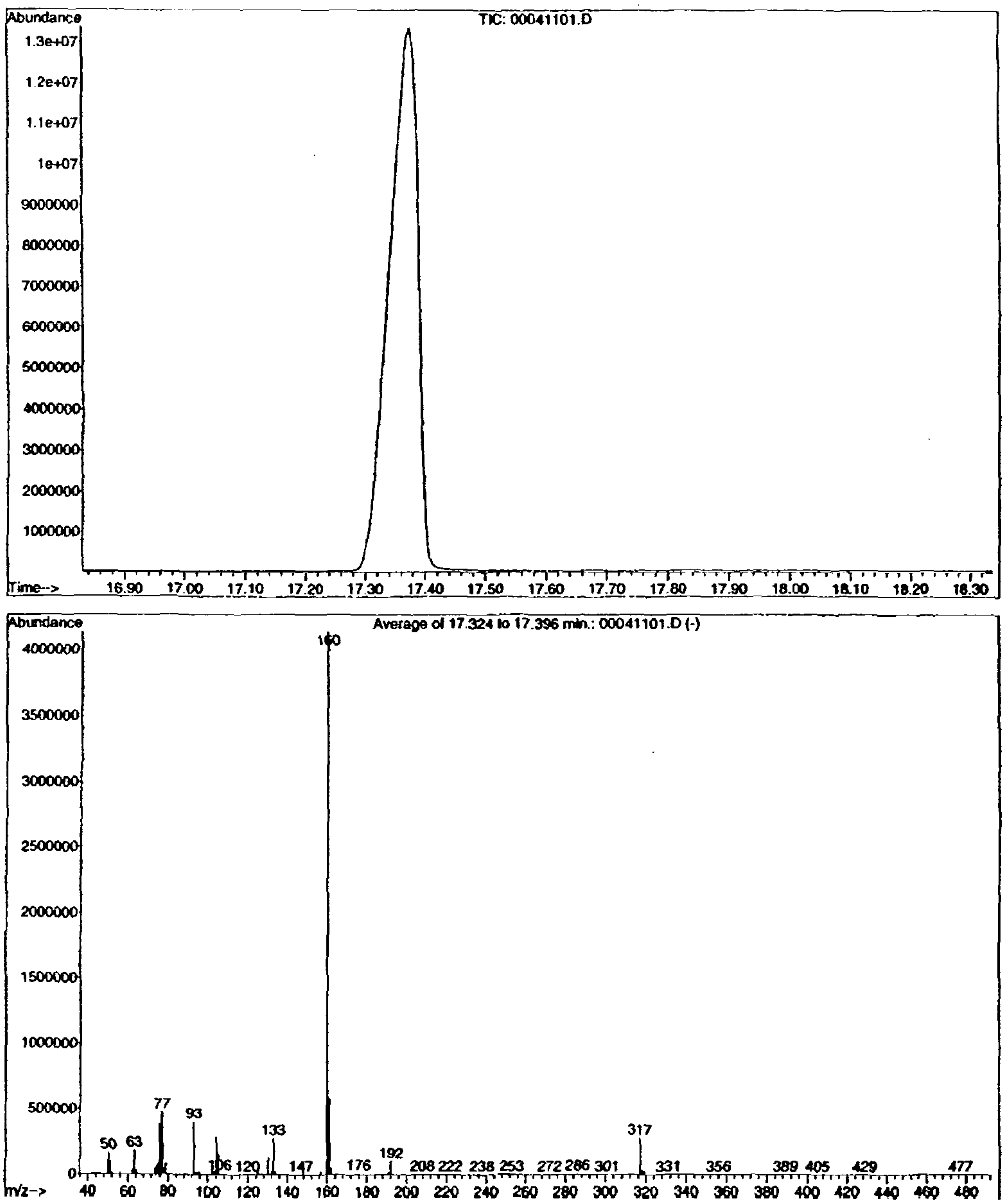

Figure 55: GC/MS spectra from direct injection of a 100ppm phosmet solution.

a) GC abundance vs. retention time in minutes

b) Mass spectrum of 17.3 min. GC peak

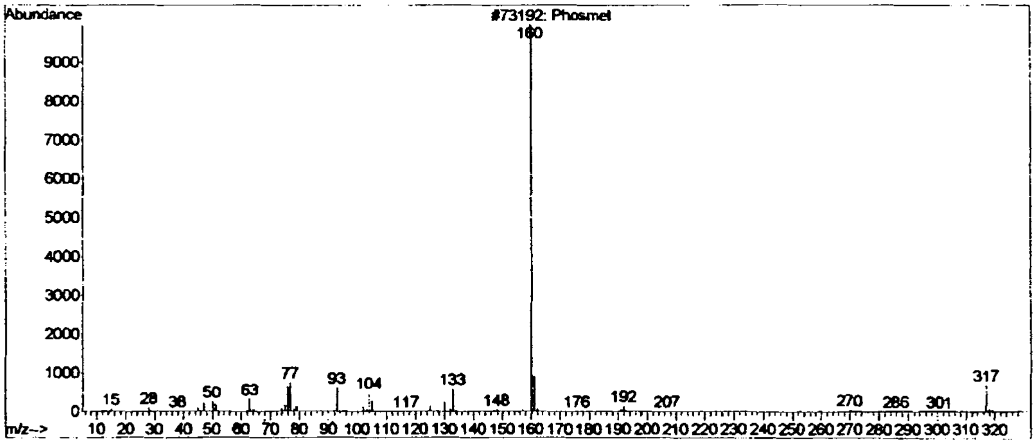

Figure 56: The standard mass spectrum of phosmet in the GC/MS database.

Phosmet is a thermally unstable material. A slow process of degradation occurs even below 50 °C and phosmet begins to decompose at 65 °C [51]. Figure 57 shows the common breakdown components of phosmet, mass 93,125 160 and 172. Since ions with mass 93, 125 and 160 also can be found from the break down components of other organic chemicals, the mass 172 ion, phosphordithioic acid, can be used as an indicator of the presence of phosmet.

Another experiment was performed to understand the thermal stability of solid phosmet. 1.2mg analytical phosmet crystal was put into a 2ml vial and this vial was put into an oven. After being heated up to a certain temperature and maintained at this temperature for 2~3 hours, the equilibrium state between phosmet solid and gas would be reached. 200μl headspace samples were extracted from the heated vial and injected into the GC/MS manually with a 500μl syringe. Figure 58~61 show the GC/MS results for headspace samples heated to 25 °C, 50 °C, 75 °C and 100 °C respectively. Selected ions mode (SIM) was used, only peaks of ion mass 125, 160 and 172 at a retention time of approximately 9 minutes were recorded in the mass spectrum. The results in figure 58~61 indicate that solid phosmet is a thermally unstable material, and the concentration of the broken down compounds, which can be expressed by the area of the ion peak, increases with temperature.

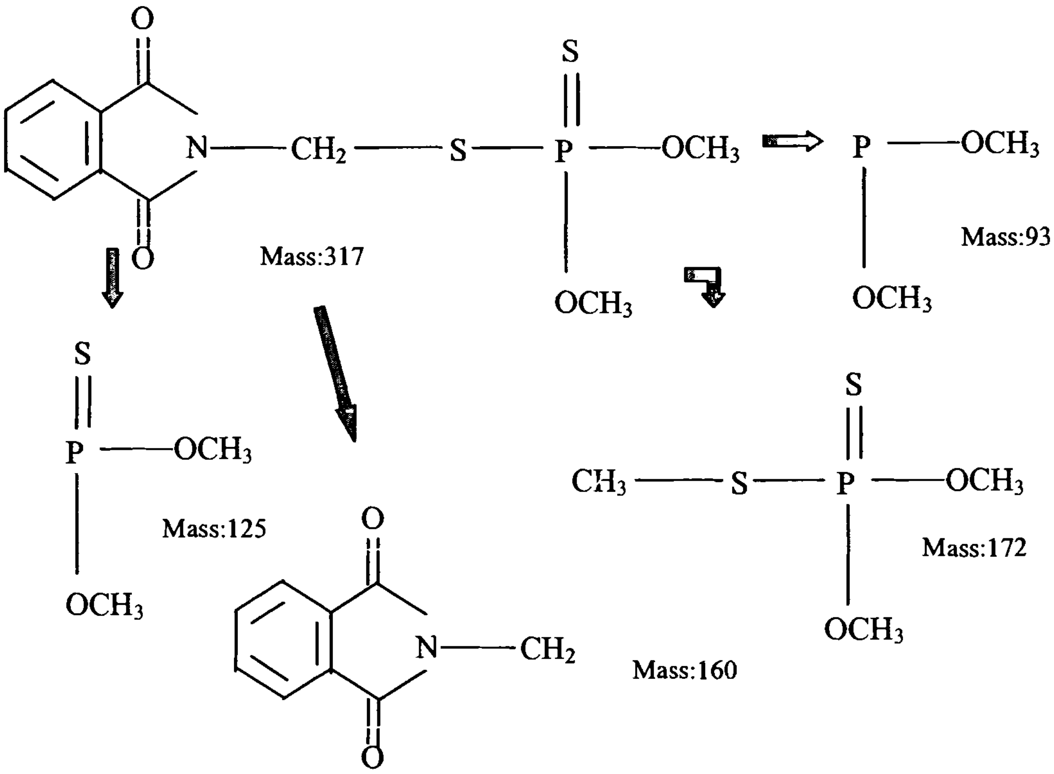

Figure 57: Breakdown components of phosmet.

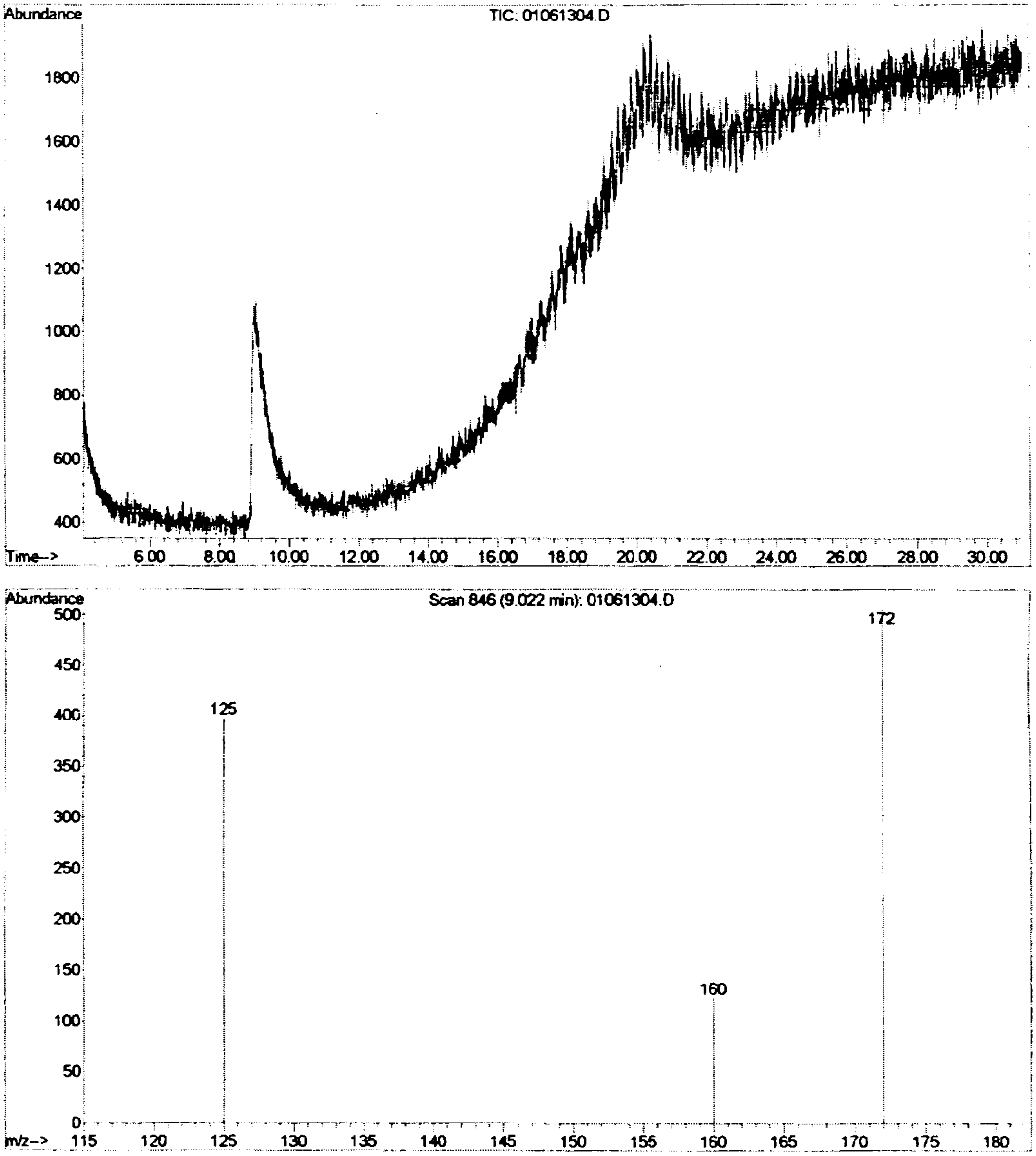

Figure 58: GC/MS spectra from pure phosmet headspace at 25 °C.

(a) GC abundance vs. retention time in minutes

(b) Mass spectrum of 9 min. GC peak

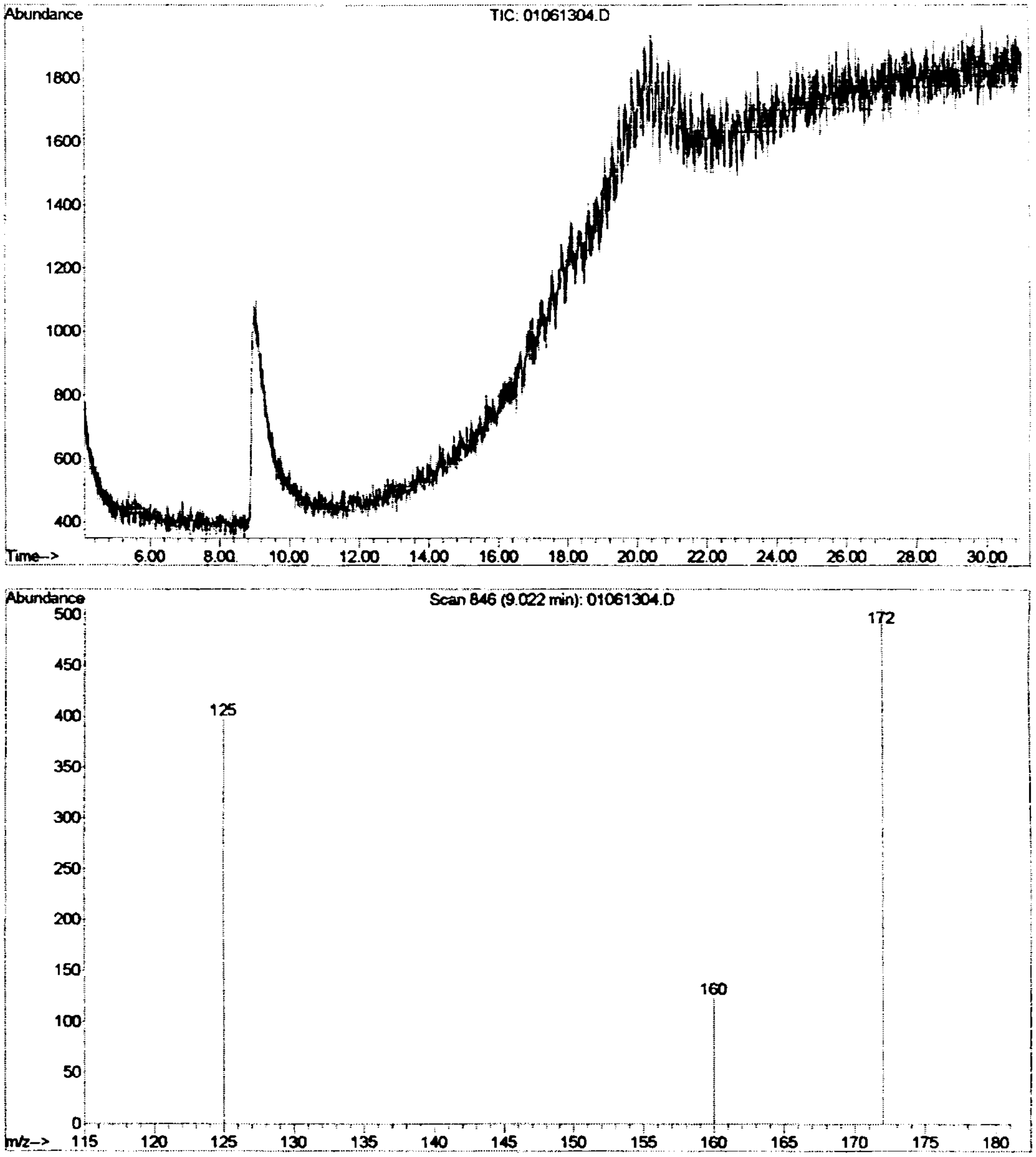

Figure 59: GC/MS spectra from pure phosmet headspace at 50 °C.

(a) GC abundance vs. retention time in minutes

(b) Mass spectrum of 9 min. GC peak

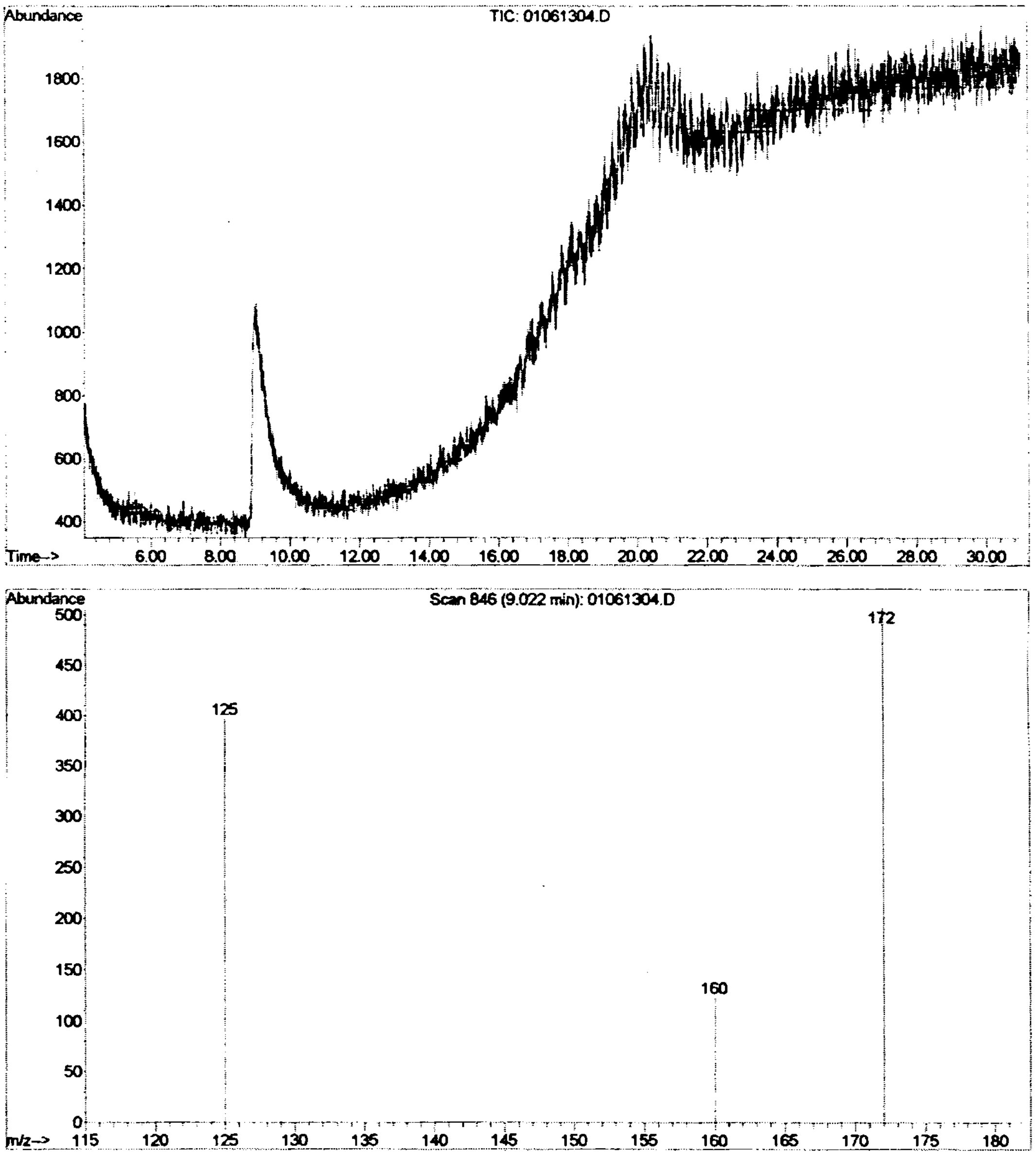

Figure 60: GC/MS spectra from pure phosmet headspace at 75 °C.

(a) GC abundance vs. retention time in minutes

(b) Mass spectrum of 9 min. GC peak

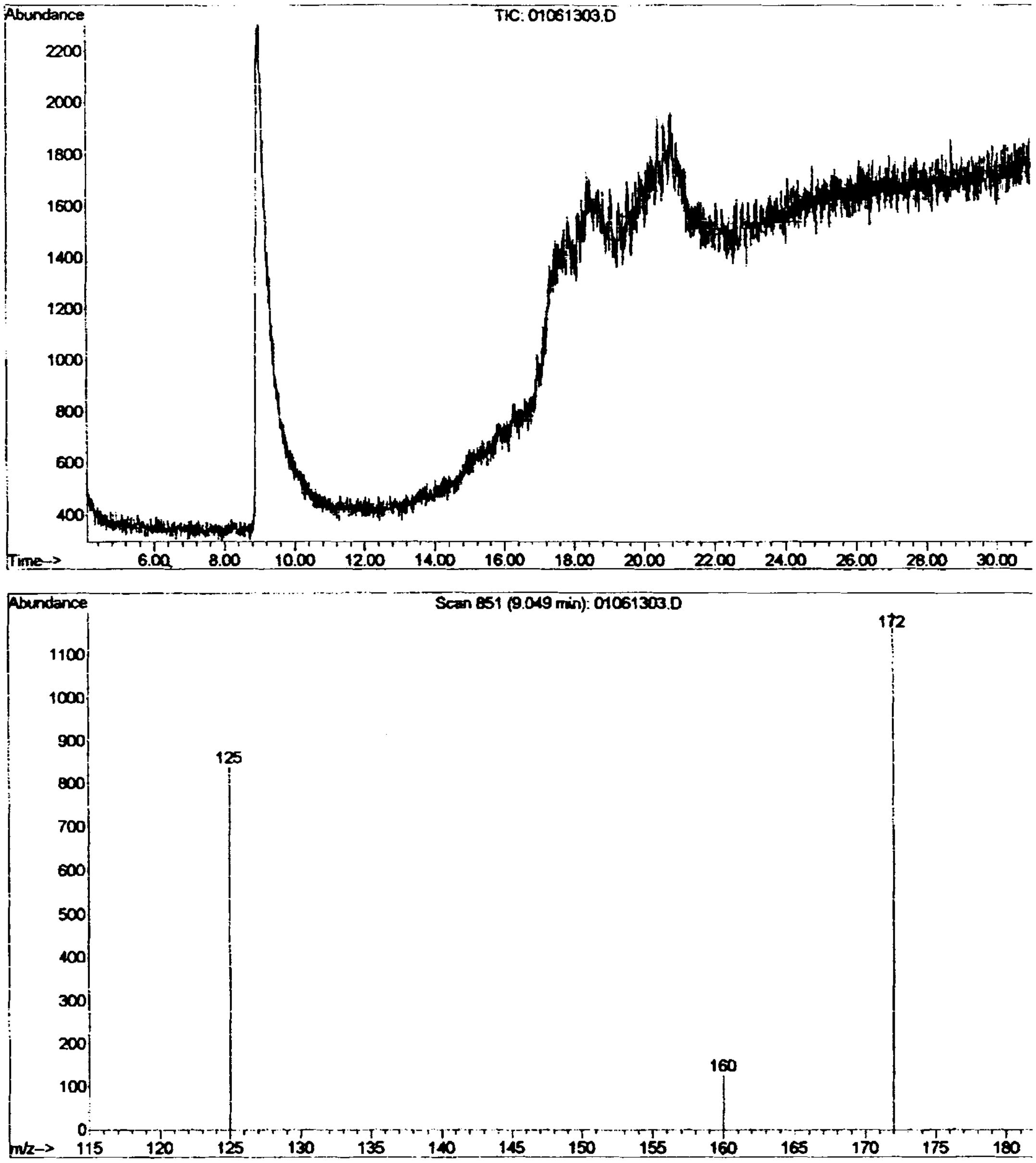

Figure 61: GC/MS spectra from pure phosmet headspace at 100 °C.

(a) GC abundance vs. retention time in minutes

(b) Mass spectrum of 9 min. GC peak

Since only ion 172 can be used as an indicator of the existence of phosmet, figure 62 summarizes the mass172 peak area as a function of headspace temperature. Figure 62 indicates that the abundance of the peak increased with the temperature but less than one magnitude from 25 °C to 50 °C. Since the documented vapor pressure of phosmet at 50 °C (0.0128Pa) is three orders magnitude higher than it at 25 °C (0.065 mPa), one possible explanation for the discrepancy is that the headspace sample was cooled down before it was injected into GC column during experiments. The phosmet compounds may condense at the inner surface of syringe to result the abundance of mass 172 peaks smaller than which it was expected to be. Another possible explanation is that the thermal break down components of phosmet, which are ion 125, 160 and 172, might have lower vapor pressure.

The headspace sample from our gas delivery system was also injected into GC/MS but no mass 125 or 172 peaks were found. This is due to the fact that there is a constant gas flow blowing through the phosmet sample channel, hence, the gas that is delivered into the sensor chamber will never reach the equilibrium state. The partial pressure of phosmet within the sensor chamber is therefore likely to be lower than it is in that 2ml vial in the equilibrium state. Since the detectable limit of in GC/MS for the concentration of phosmet gas under equilibrium state can reach 1ppb level, the estimated concentration of phosmet gas within the gas delivery system should be less than 1ppb.

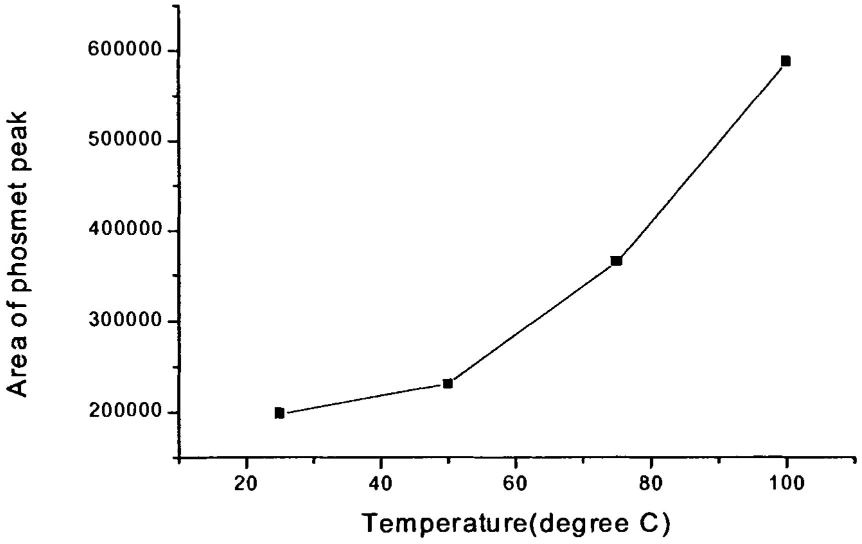

Figure 62: Area of ion 172 peak as a function of temperature.

Since the concentration of phosmet residue on the surface of blueberries is too low to be directly detected by GC/MS, a purge & trap concentrator was used. 5.2g of phosmet treated blueberries were crushed and put into a glass sampler. During the purge cycle, which lasts approximately 10 minutes and maintains at 40 °C, helium gas was bubbled through the above crushed blueberries to deliver the headspace of the blueberry sample to the column within the concentrator where the selected compounds including phosmet molecules, based on the characteristic of the column were absorbed. Those compounds were desorbed during the trap cycle by heating to 175 °C and automatically injected into GC/MS. Figures 63 and 64 show the spectrum from samples of blueberries with 1ppm phosmet and organic blueberries. The retention time of ion 172 and 125 in figure 63 is around 6.2 minutes. These results indicate that the purge & trap effectively concentrates the phosmet component of the treated blueberry sample. More importantly, heated organic blueberries do not decompose into the same ions, instead they decompose into limonene, which is ion 136. Therefore the presence of ion 172 can be used as an indicator to detect phosmet on blueberries.

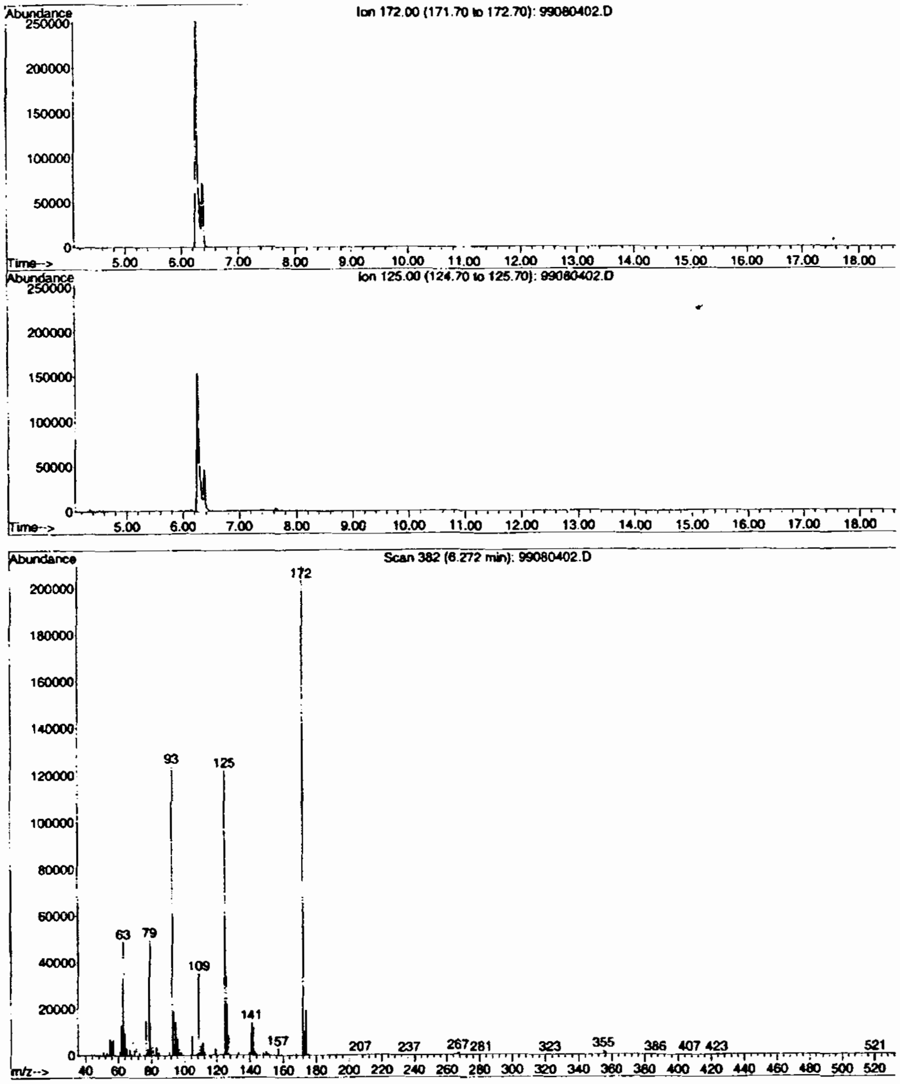

Figure 63: GC/MS spectra from a headspace of 1ppm treated blueberry sample using purge & trap concentrator.

(a) Ion 172 abundance in SIM mode vs. retention time in minutes

(b) Ion 125 abundance in SIM mode vs. retention time in minutes

(c) Mass spectrum of 6.2 min. GC peak

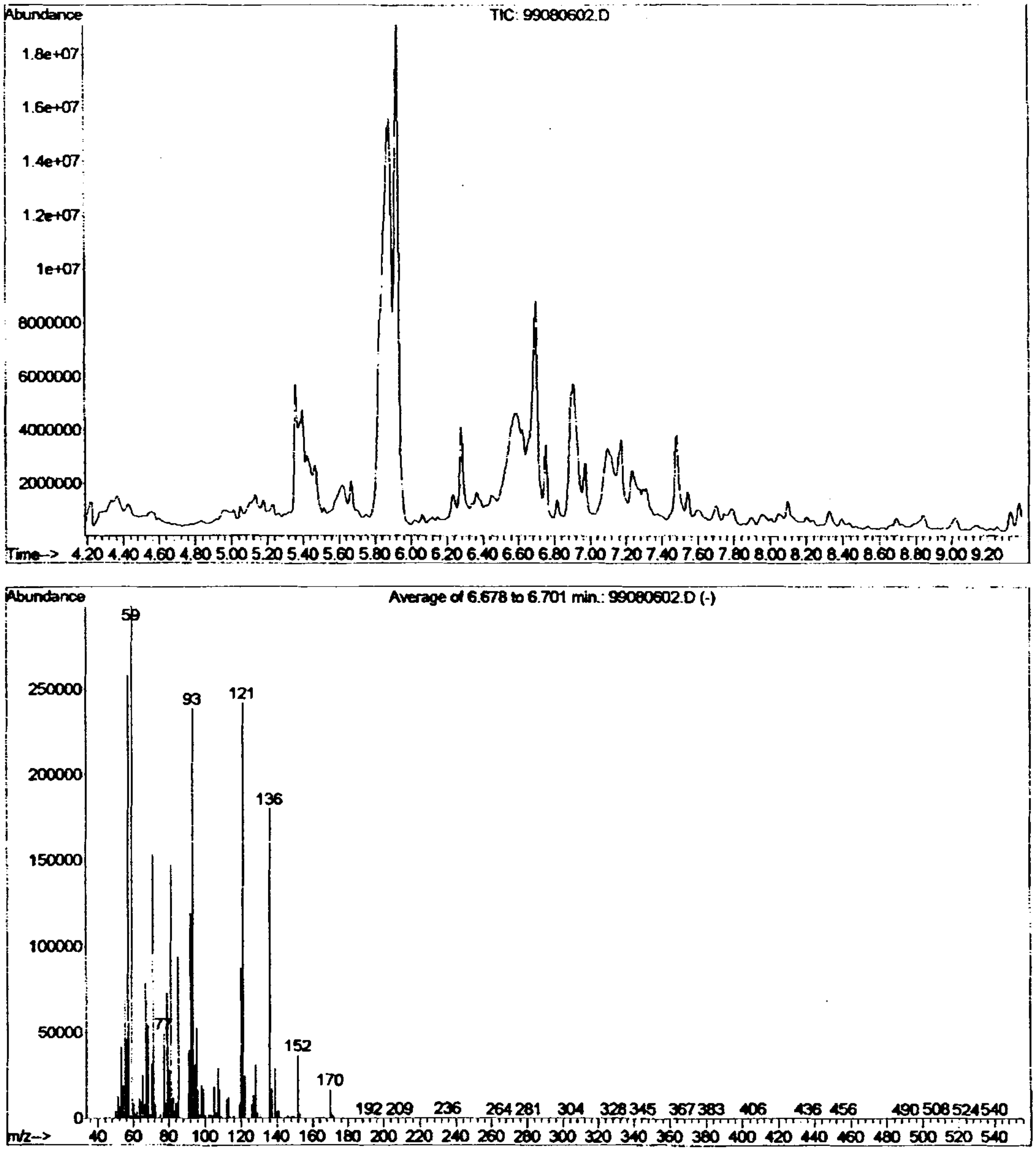

Figure 64: GC/MS spectra from the headspace of an organic blueberry sample using purge & trap concentrator.

(a) GC abundance in SIM mode vs. retention time in minutes

(b) Mass spectrum of 6.6 min. GC peak

5 SUMMARY, CONCLUSIONS AND FUTURE WORK

5.1 Summary

In this thesis, two sensing technologies have been examined in depth in order to determine whether they are capable of selectively detecting pesticides such as phosmet, which is commonly used on blueberries. The two sensing techniques were the polymer coated quartz crystal microbalance (QCM), where the polymer film used was polyepichlorohydrin (PECH) and the semiconductor metal oxide (SMO) sensor, with tungsten trioxide (WO_3) used as the sensing film. The polymer coated QCM sensing technique is based on the relationship between the resonant frequency shift of the QCM and the mass and liquid loading phenomena occurring on its sensing surface when exposed to a target analyte either in air or liquid. The SMO sensing technique is based on the change of electrical conductivity, which is caused by the interactions between the analyte and SMO film.

In the case of the QCM sensor, the Sauerbrey and Kanazawa's equations, which describe the behavior of the QCM in air and liquid respectively, were derived. The Sauerbrey equation relates the change in the resonant frequency of the QCM to the mass loading on the sensing surface when the QCM is in air. Kanazawa's equation describes the change in resonant frequency of the QCM when the QCM's sensing surface is immersed in a Newtonian liquid. Kanazawa's equation shows that the resonant frequency shift caused by immersing the sensing face of a quartz crystal in a viscous fluid is a function of the material parameters of the fluid and the quartz crystal.

Experimentally, it is shown that the QCM sensor can be electrically excited into resonance by applying a voltage across the electrodes of the quartz crystal disk. A standing shear wave, which is an integral number of half wavelengths, is set up between the two surfaces of the crystal disk. The frequency response mechanism of the QCM is described using Butterworth-Van Dyke (BVD) type equivalent circuit models. The behaviour of the unpertubed (without any loading) QCM in air driven by an AC voltage was also presented and then followed by the effect of mass loading and liquid loading simultaneously. The admittance of the QCM near resonance was obtained and the modified BVD equivalent circuit elements were explicitly related to the physical properties of the QCM and the perturbing mass and fluid.

In order to detect phosmet sensitively and selectively, PECH was selected as the coating film for the 5 MHz commercial QCM sensors. The possible response mechanism between phosmet and the polymer coating was also qualitively discussed. A frequency measurement system based on an oscillating circuit was built to measure the resonant frequency shift of the bare and PECH coated QCM sensors under mass and liquid loading.

Several experiments were performed on the QCM sensor. In order to determine whether the bare QCM will sorb phosmet, a bare QCM in a water bath was exposed to phosmet solution injections. Another experiment was also performed on a PECH coated QCM to determine what effect the fluid density and viscosity changes caused by additives such as methanol may have. The response of the PECH coated

QCM sensor was then investigated in a water bath consisting of various concentrations of phosmet. After the PECH coated crystal was rinsed and stored at ambient temperature for several days, another experiment was performed where the water bath was flushed with distilled water following a series of phosmet solution injections. Experiments were also performed to detect phosmet in blueberry juice. The response of the PECH coated QCM sensor was first investigated in organic blueberry juice, which contained various concentrations of phosmet (treated blueberry juice). Then another experiment was performed with the same PECH coated QCM where a water bath was flushed with treated blueberry juice and organic blueberry juice respectively. In order to detect the phosmet in treated blueberry juice, an experiment was performed where a PECH coated crystal and a bare crystal were placed sequentially in a water bath and then were flushed treated blueberry juice and water, the difference between the two frequency responses of the PECH coated and bare QCM was measured. The effect of the PECH film and gold electrodes on the device response exposed to the treated blueberry juice is discussed in detail, particularly relative to the selectivity of the QCM sensor.

For the SMO sensing technique, electron band theory was first presented to gain an understanding of the conductivity change when the WO_3 film is in contact with a reducing target gas. Three spillover models were also presented to obtain an understanding of the Au catalyst. Gold-doped WO_3 and pure WO_3 films were selected as the sensing elements. A positive pressure gas delivery system was set up to deliver the phosmet gas to determine the response between the WO_3 film and phosmet. The resistance of the gold-doped and pure WO_3 films was measured in compressed air under various exposures of phosmet gas. The surfaces of some of the WO_3 sensors were analyzed by using Auger electron spectroscopy (AES) to qualitively determine the poisoning phenomena, which relates to the dramtic decrease of the film conductivity response observed in the SMO experiments after several exposures of target gas.

In order to detect phosmet dissolved in organic solvent, phosmet residues on blueberries and also to determine possible interferent molecules present in the blueberries, another common analytical method called gas chromatography/mass spectrometry (GC/MS) was used in this thesis. The operating principle of the GC/MS was first presented, then phosmet dissolved in organic solvent and phosmet residues on blueberries were detected via GC/MS. The thermal stability of phosmet was also explored via the GC/MS. A purge and trap concentrator was connected to the GC/MS to collect and concentrate the phosmet residue on the surface of the blueberry samples and make it detectable by the GC/MS.

5.2 Conclusions

The experimental results obtained using the QCM sensor in this thesis indicate that the phosmet solution injected in water or organic blueberry juice can be detected by the PECH coated QCM with at least 1ppm sensitivity. However, it is still difficult to detect the phosmet dissolved in treated blueberry juice using the differential setup only with one PECH coated QCM and one bare QCM due to the shielding phenomena of the PECH film. The shielding phenomena is used to describe the phenomena that the frequency shift obtained when the bare QCM immersed in water is flushed by treated blueberry juice is larger than the corresponding frequency shift obtained using the PECH coated QCM. This may due to the fact that the gold surface of the bare QCM could sorb other organic compounds in blueberry juice forming an amalgation. In order to make the QCM work at its series resonant frequency, the phase shift of the oscillating circuit should be $2n\pi(n = 0,1,2K)$, however, due to the series and parallel added impedance term shown as $Z(\omega)$ in figure 18, the oscillating circuit used in this thesis operates at a constant nonzero phase of -60°. This results in a discrepancy between the observed experimental results and the results predicted by the theory, which was discussed in detail in section 4.1.1.

The experimental results obtained using the SMO sensing technique in this thesis indicate that the gold-doped and pure WO_3 sensors can detect phosmet in compressed air, down to at least 10ppb. However, the fast poisoning phenomenon observed due possibly to the interaction between gold and the sulfur component of phosmet also indicates that the gold-doped WO_3 sensor cannot be repeatedly used. On the other hand, the strong interaction between gold and the sulfur component of phosmet may indicate the possible selectivity of gold doped WO_3 film in phosmet detection. The 2 hours response time of the pure WO_3 film to phosmet exposure makes it unclear whether the response observed is due to the phosmet exposures or something else.

Generally, the advantage of the polymer coated QCM sensor is that it can be used in both a gas and liquid environment, while the SMO sensor only can be used in a gas environment. Since the concentration of phosmet in the liquid phase detection will be higher than in gas phase detection, the polymer coated QCM sensors have much more potential in the detection of the phosmet.

From the experimental results obtained using the QCM sensor, the following specific conclusions can be drawn,

1. The sensing area of the bare QCM does not absorb phosmet within the detectable limit. The PECH coating also does not absorb methanol within the detectable limit.
2. The PECH coated QCM sensor displays almost a linear response to injections of phosmet solution in distilled water up to 25ppm. During the injection process the solution first becomes supersaturated until a total of 75 μl phosmet solution have been added. At that point there was an increase in the QCM frequency, which is most likely due primarily to precipitation of phosmet from the supersatured solution and the subsequent phosmet desorption from the PECH film.
3. The detectable concentration of phosmet is 1ppm and the sensitivity of the PECH coated QCM is 15±2 Hz/ppm.
4. The PECH coated QCM sensor displays good reproducibility to injections of phosmet solution up to 25ppm.
5. The phosmet sorbed on the PECH coating can be washed off by flushing with distilled water.
6. When the PECH coated QCM is submerged in organic blueberry juice, phosmet still can be absorbed on the PECH coating and detected by the QCM.
7. The PECH coated QCM displays a nearly linear response to injections of phosmet solution in organic blueberry juice in the low phosmet concentration range and the response curve becomes quadratic in the high phosmet concentration range.

8. The observed solubility limit of phosmet in organic blueberry juice is 39g/ml, which is higher than 25mg/l limit in water.
9. The resonant frequency shift of the PECH coated QCM submerged in blueberry juice is due to the mass loading and liquid loading.
10. The sensing area of the bare QCM, which has gold electrodes, may sorb other organic compounds from the blueberry juice forming an amalgation. This causes the frequency shift obtained for the bare QCM immersed in water and flushed by treated blueberry juice to be larger than the corresponding result obtained with the PECH coated QCM, even though the bare QCM does not sorb phosmet within the detectable limit.
11. It may be feasible to utilize this sensor to detect phosmet residue on blueberries if all other interferences are removed by a pretreatment process, or by using an array of variously coated QCMs.
12. When the QCM is working at its series resonant frequency, the phase shift of the oscillating circuit should be $2n\pi(n = 0,1,2K)$, however, the working point of the oscillating circuit for the frequency measuring system shown in figure 17 is determined as -60°.
13. In the experiment done by Dr. Chao Zhang [62], the frequency shift of a 5MHz bare QCM operating at -60° phase in air and water is three times higher than the frequency shift predicted by the Kanazawa's equation, which is derived based on the QCM operating at zero phase. Another experimental result obtained by Yihe Hu from LASST [63] shows that the resonant frequency shift of a 5MHz bare

QCM measured by a zero phase oscillator is 621Hz when it was immersed in water. Considering the approximations made during the derivation, this result is in reasonable agreement with the shift of 709Hz calculated using Kanazawa's equation.

From the experimental results obtained using the SMO sensing technique, the following specific conclusions related can be drawn,

1. The conductivity of gold doped WO_3 films and pure WO_3 films is increased after phosmet exposures.
2. The gold doped WO_3 film at 350 °C is very sensitive to phosmet gas with 50% humidity, even though the concentration of phosmet gas within the gas delivery system is estimated to be lower than 10ppb.
3. The gold doped WO_3 at 350 °C is poisoned by repeated exposures to phosmet gas. It is likely that sulfur, which is the break down component of heated phosmet, is responsible for the poisoning. Sensitivity can't be recovered even following heating the film up to 500 °C.
4. The sensitivity of the pure WO_3 film to phosmet gas exposures is higher than the sensitivity of the gold-doped WO_3 film.
5. The sensitivity of the pure WO_3 film may be the maximum at 350 °C or higher.
6. The response time of the pure WO_3 film is about 2 hours, which is longer than the 15 minutes response time of the gold-doped WO_3 film.

From the experimental results obtained using GC/MS sensing technique, the following specific conclusions related can be drawn,

1. Phosmet dissolved in organic solvent can be detected by GC/MS.
2. The common break down components of phosmet as verified by GC/MS are ions with mass 93, 125 160 and 172.
3. The abundance of the mass 172 peak of the head space in samples increased with the environment temperature.
4. The concentration of phosmet gas within the gas delivery system is less than the detectable limit of the GC/MS with the method used.
5. Phosmet residues on blueberries are too low to be directly detected by GC/MS.
6. The purge and trap concentrator can concentrate the phosmet compounds on blueberries and make them detectable by GC/MS.
7. Phosphordithioic acid, ion 172 can be used as an indicator to detect phosmet in treated blueberry samples.

5.3 Future Work

Two sensing technologies, QCM and SMO have been examined theoretically and experimentally in this thesis. From the experimental and theoretical results obtained and conclusions drawn, numerous theoretical and /or experimental problems can be identified.

In the case of the QCM sensor, all the experimental results presented in section 4.1 and 4.2 were obtained by measuring the resonant frequency using oscillator circuit with a nonzero phase term introduced by $Z(\omega)$ shown in figure 18. These experiments need to be repeated by using a QCM oscillator configuration in which $Z(\omega)=0$ to determine the mass and liquid sensitivity of the PECH coated QCM operating in blueberry juice. The experimental results can then be directly compared to the theory presented in the appendices. Further work is also needed using the impedance analyzer to separate the mass loading from liquid loading responses.

The preliminary result shows that the liquid sensitivity constant of a 5MHz bare QCM operating at -60° phase in distilled water is much higher than that obtained operating at zero phase. This is due to the impedance term $Z(\omega)$ shown in figure 19. It is still unclear how this impedance term affects the sensitivity of the QCM, hence it needs to be examined both experimentally and theoretically in an equivalent circuit model to get the explict relationship between the mass sensitivity and phase shift of the QCM. Theoretically, an analytical equation for the resonant frequency shift, Δf_s, can be obtained from the circuit in figure 19 which can be expressed as follows,

$$\Delta f_s = f[C_0, C_1, L_1, R_1, L_2, R_2, L_3, Z(\omega)]. \tag{20}$$

The resonant frequency shift Δf_s in equation (20) could be different by manuipulating the phase term ϕ_1, associated with $Z(\omega)$. Hence, sensitivity of the QCM could be increased or decreased depending upon the value of the phaseterm, ϕ_1. Experimentally, various new oscillating circuits can be built with various phases of $Z(\omega)$ and the experiments repeated, using the same QCM driven by the various oscillators. The sensitivity of the QCM sensor may be optimized both theoretically and experimentally by a juditious choice of the phase term.

Since the sensing area of the bare QCM, which has a gold electrode, may absorb other organic compounds from the blueberry juice, other electrode materials such as aluminum, platinum, or non-adsorbing coatings should be investigated, which may not sorb organic compounds needs to be tested.

The selection of a polymer coating for specific analytes or classes of analytes is a key step in determining sensitivity and selectivity when using the QCM sensing technique. The response mechanism between PECH and phosmet is a hydrogen-bonding interaction. Improving the hydrogen bonding interactions can potentially lead to large improvements to sensitivity. Therefore, since phosmet that has strong hydrogen bond basic properties, the sensitivity should be enhanced by choosing a complementary polymer with strong hydrogen bond acidic properties, such as SXFA and P4V. Figure 65 shows the structure of PECH, SXFA and P4V. Because SXFA and P4V are not commercially available, they would need to be synthesized.

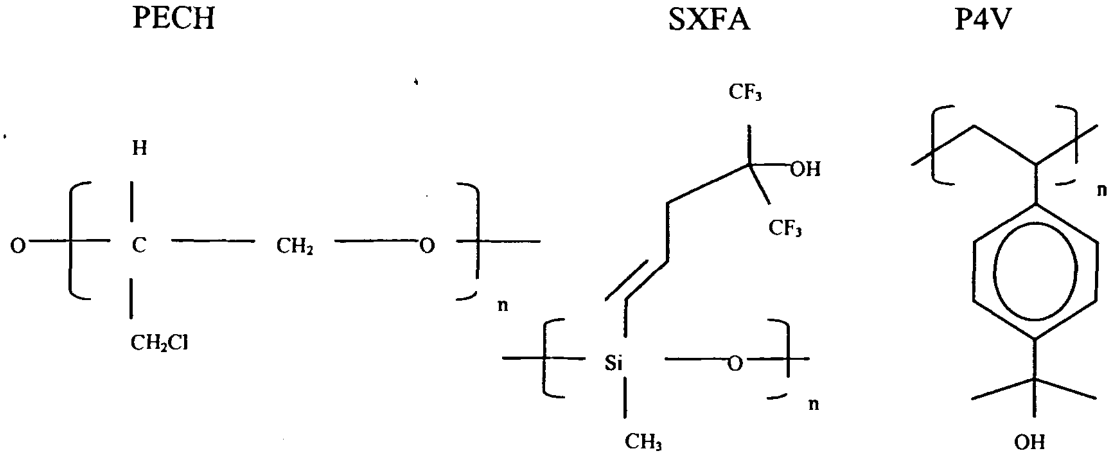
PECH
SXFA
P4V

Figure 65: Polymer structure for PECH, SXFA and P4V.

In order to understand the relationship between the thickness of the polymer coating and its sensing properties, more experiments should be performed for coatings of different thickness. The sensitivity can be enhanced through utilizing higher frequency sensing crystals such as commercially available 9 MHz crystals. Modifying the sensing electrode structure of the QCM also may result in increased sensitivity to analytes over the AT-cut QCM with the standard electrode structure, shown in figure 1[52]. QCMs with small sensing electrodes, or open or closed ring structures should be tested in the future. Lateral field excitation (LE) has been applied for oscillators and resonators instead of thickness excitation (TE) recently, because of its reduced aging and higher Q values etc. It is worth investigating the use of QCM sensors with LE configurations in pesticide detection.

Generally, the polymeric coatings are not uniquely selective toward one analyte but are selective toward a particular class of analyte. To achieve high selectivity and avoid false alarms, QCM sensor systems should be designed around arrays of QCM devices. The array gives a pattern of responses depending on the solubility properties of the coatings used [53] and the solubility properties of the targets being analyzed [54]. The analyte or mixture of analytes can then be identified using pattern recognition techniques such as neural network algorithms. Sample pretreatment and filtering techniques are another approach that needs to be explored to decrease the magnitude of interactions between interferents and the polymer coating.

In the case of SMO sensors, because the gold catalyst will be poisoned by the break down components of phosmet, the use of other catalyst such as platinum should be explored. Since more time is required to reach the equilibrium state between the sensing film and the target gas for thick sensing films, the use of thinner undoped WO_3 films needs to be explored to speed up the response between undoped WO_3 and phosmet gas. In order to increase the concentration of the phosmet gas through the gas delivery system, a purge and trap concentrator can be put into the system. The phosmet gas concentration within the gas delivery system also needs to be quantified. In order to understand the kinetic mechanism of the interactions between phosmet gas and WO_3 film, experiments should be done within a vacuum chamber and XPS or Auger also should be used to examine the surface of the films. The use of other SMO films such as ZnO or SnO_2 also needs to be explored to obtain the optimum sensing film for phosmet gas. In the case of sensing phosmet residues in blueberries, pre-filtering technique should be explored to decrease the influence of interferes.

Since phosmet also has been widely used to control pests in the agriculture industry, phosmet applied on other fruits and vegetables such as grapes and apples may also be detected using the QCM sensing technique. Other organophosphorous pesticides, which have the similar chemical and physical properties, such as guthion, parathion etc., are also widely used. It would be worthwhile to try detecting them using the QCM sensing technique presented in this thesis in the future.

REFERENCES

[1] Pesticide in food: A look at the issues. *The National Database*. Washington D.C., (1992).

[2] Beusen, J.M. and Neven, B. *Bull. Environ. Contam. Toxicol.* 42, P. 26-133 (1989).

[3] Gucciardo, L.S. *Pesticide Applicator Training Manual.* P. 1-1 (1992).

[4] Cremlyn, R.J. *Agrochemicals, John Wiley & Sons.* P. 123 (1991).

[5] Lathrop, F.H. and C.B. Nickels. *USDA Tech. Bull.* 275, P. 77 (1932).

[6] Crozier, L. *Lowbush Blueberry Fact Sheet.* Nova Scotia Blueberry Institute P. 6 (1995).

[7] International Chemical Safety Cards. ICSC:0543. Siri.uvm.edu/msds/mf/cards/file/0543.html.

[8] Oh, S.W., Y.H. Kim, D.J. Yoo, S.M. Oh and S.J. Park. *Sensors and Actuators B*, 13-14, P. 400-403.

[9] Biros, F.J. *Advances in Chemistry Series*, 104, Washington D.C., (1971).

[10] Sherma, J. and Zweig, G. *Analytical Chemistry* 55, (1983).

[11] Stan, H.J., Abraham, B. Jung, J. Kellert, M. and Steinland, K. *Analytical Chemistry* 287, P. 271(1977).

[12] Schedie, E.P. and Guilbault, G.G. *Analytical Chemistry*, 44, P. 1764(1972).

[13] Tomita, Y. and Guibault, G.G. *Analytical Chemistry* 52, P. 1484(1980).

[14] Guibault, G.G., Affolter, J. and Tomita, Y. *Analytical Chemistry*, Vol. 53, P. 2057(1981).

[15] Ngeh-Ngwaibhi, J., Foley, P.H., S.S., and Guilbault, G.G., *J. Am. Chem. Soc.*, 108, P. 5444-5447(1986).

[16] Yuan, Z.Y., Zhou, T.M., Li, S.Y., Ti, X.S., Li, D.Y. and Wlodarski, W.B., *1st World Biosensor's Congress*, Singapore, May 1990.

[17] Sauerbrey, G. *Z. Phys.*, 155, P. 260(1959).

[18] Mecea, V.M. *Sensors and Actuators* A, 40, P. 1-27 (1994)

[19] Kanazawa, K.K. and Gordan II, J.G. *Anal. Chem. Acta* 175, P. 99-105(1985).

[20] Kanazawa, K.K. and Gordan II, J.G. *Anal. Chem.* 57, P. 1770-1771(1985).

[21] Tiersten, H. *Linear Piezoelectric Plate Vibrations*, New York & Plenum, (1969).

[22] Martin, S. J., Granstaff, Victo.Ed.and Frye, Greg. C. *Anal. Chem.* 63, P. 2272-2281(1991).

[23] McGill, R.A., Abraham, M.H. and Grate, J.W. *Chemitech*, 27 September (1994).

[24] Ref. 23, P.30.

[25] Bloor, D. M.Chemistry Department, School of Sciences, Salford, UK. www.sciences.salford.ac.uk/chemist/Lecnotes/Bloor%20DM/Colloids/Lect7.pdf

[26] Zarzycki, R. *Absorption: fundamentals & applications* Oxford, New York & Pergamon Press, 1993 1st Edition.

[27] Heiland, G. *Sensors and Actuators*, 2, P. 345(1982).

[28] Morrison, S. R. *Sensors and Actuators*, 2, P. 333(1982).

[29] Chang, S.C. *J. Vac. Sci.Technol*, 17, P. 366(1980).

[30] Ref. 28, P.349.

[31] Fruhberger, B. Ph.D. thesis, University of Ruprecht Karls, Heidelberg, Germany, *Interface Chemistry of Gold Doped Tungsten Trioxide Films in the reaction with hydrogen Sulfide*, P. 120(1994).

[32] Bertoni, G. and Liberti, A. *Annali di chimca, Societa Chimica Italiana*, 76, P. 24(1986)

[33] (ed.) Imelik et al., B. *Metal-Support and Metal-Additive Effects in Catalysis,* Elsevier, Amsterdam (1982).

[34] Khoobiar, S.*The Journal of Physical Chemistry*, 68, No.2, P. 411(1964).

[35] Matsushima, S., Teraoka, Y., Miura, N., and Yamazoe, N.*Japanese Journal of Applied Physics*, 27, No. 10, P. 1798(1988).

[36] David Thompson, " New advances in Gold Catalasis" *Gold Bulletin*, 32 (1) P. 12 (1999).

[37] Hartley, D. *The Agrochemicals Handbook*, Royal Socity of Chemistry, England, P. 26(1987).

[38] *The pesticide manual* 6th edition, The British Crop Protection council P. 423

[39] *Tolerances and Exemptions from Tolerances for Pesticide Chemicals in or on Raw Agricultural Commodities*, 40 CFR 180, subpart A, B, and C, In Code of Federal Regulations, P. 273~434 USEPA (1998).

[40] Hallenbeck, W.H. *Pesticides and Human Health*. Springer-Verlag New York Inc., NY., P. 97(1985).

[41] Ishida, S.*Bull. of the Chem. Soc. Of Japan*, 33, No.6, P. 728(1960).

[42] Reid, R.C., Prausnitz J.M. and Sherwood, T.K. *The Properties of Gases and Liquids*, 3rd ed., New Yok: McGraw-Hill (1977).

[43] Braithwaite, A. Chromatographic Methods. Chapman and Hall Ltd., NY. 2, (1985).

[44] Martin, S. J., Spates, J. J., Wessendof, K. O., and Schneider, T. W. *Anal. Chem.*, 69, P. 2050-2054(1997)

[45] Company files of CHROMADEX, Inc. http://www.chromadex.com/Phytochemicals/Blueberry

[46] Kariis, H. "Adsorption of Organic Phosphines and Thiols on Metal Surfaces" Department of Physics and Measurement Technology, Linköping University, S-581 83 Linköping, Sweden http://www.bibl.liu.se/liupubl/disp/disp98/tek523s.htm

[47]] Company files of Q-SENSE, Inc

http://www.q-sense.com/qPages/sub/applic/qsense_adsorption_fibrinogen.PDF

[48] Tian, L. Thesis of the degree of Master of Science in Food Science and Human Nutrition, University of Maine at Orono, 21(1994).

[49] Ed. King, D. A. and Woodruff, D. P. *The Chemical Physics of Sold Surfaces*, 6, Elsevier P. 289 (1993)

[50] Handbook of Auger electron spectroscopy.

[51] Bertoni, G., Liberti, A., Bellina Agostinone, C. *Annali di Chimica* 76, 1986 Societa Chica Italiana.

[52] Zhang, C., and Vetlino, J. F. *IEEE transactions on Ultrosonics, Ferroelectrics and Frequency control,* 48 No. 3, (2001).

[53] M.H.Abraham, Grellier, P.L., McGill, R.A., Doherty, R.M. *Polymer* 28, P. 1363(1987)

[54] Abraham, M.H. *Chem. Soc. Revs.*73 (1987).

[55] Schmitt, R. F., Allen, John W., and Vetelino, J.F. *Sensors and Actuators,* B76, P. 95-102(2001).

[56] Rosenbaum, J. F. *Bulk Acoustic Wave Theory and Devices*, Artech: Boston, Chapter 6, 1988.

[57] Salt, D. *High-Q Handbook of Quartz Crystal Devices*, Van Nostrand Reinhold, New York, 1987.

[58] Auld, B.A. *Acoustic Fields and Waves in Solids*, Wiley: New York, Chapter 3, 1973.

[59] Hu, B., Vetelino, J. F. " New Mechanism of Spillover Chemistry: Gold Catalyzed Reduction of WO3", 7th International Chemical Sensors Conference P.767-769

[60] CRC Handbook of Chemistry and Physics, 55th edition.

[61] Tiersten, H.F. *Linear Piezoelectric Plate Vibrations*, Plenum Press: New York, 1969.

[62] Private communication with Dr. Chao Zhang, Sawyer research center, University of Maine, Orono ME 04469

[63] Private communication with Mr. Yihe Hu, Sawyer research center, University of Maine, Orono ME 04469.

[64] Private communication with Dr. Todd Mlsna, Sensor Research & Development Inc., Orono ME 04469

[65] Robertson, R.E. *Fresh produce Potential implications of Country-of Origin Labeling* , United States General Accounting Office, 1999.

http://www.gao.gov/archive/1999/rc99200t.pdf

APPENDIX A: Derivation of Sauerbrey Equation (Equation 1)

Sauerbrey [17] has shown that the decrease in the resonant frequency of a thickness shear vibrating quartz crystal, Δf, having either an AT or BT cut, is proportional to the accumulated mass on the sensing surface of the crystal. In this appendix, this relationship is derived in detail.

The velocity of a shear wave propagating in AT cut quartz can be expressed as [17],

$$V_{shear} = \sqrt{\frac{\mu_q}{\rho_q}}, \tag{A-1}$$

where μ_q is the stiffened shear modulus of quartz and defined as

$\mu_q = \overline{C_{66}} = C_{66} + e_{26}^2 / \varepsilon_{22}$, C_{66}, e_{26} and ε_{22} are the quartz elastic, piezoelectric and permittivity constants of quartz crystal respectively, and ρ_q is the density of quartz. For the AT cut in quartz μ_q ==2.947x10^{11} dyne cm^{-2} and ρ_q=2.648 g cm^{-3} [17]. It should be noted that C_{66}, e_{26} and ε_{22} are the rotated constants corresponding to the AT-cut in quartz.

Since there is a standing wave generated across the quartz crystal disc when the crystal is electrically excited into resonance, the wavelength of the shear wave at the fundamental resonant frequency is $\lambda = 2h_q$, where h_q is the thickness of the quartz disc. Using equation (A-1), the fundamental resonant frequency can be expressed as,

$$f_q = \frac{V_{shear}}{\lambda} = \frac{V_{shear}}{2h_q} = \frac{\sqrt{\mu_q}}{2h_q\sqrt{\rho_q}}. \qquad \text{(A-2)}$$

Since the mass of the quartz crystal may be expressed as,

$$M_q = \rho_q h_q S, \qquad \text{(A-3)}$$

where S is the surface area of the quartz, solving (A-3) for h_q and substituting into (A-2) yields,

$$f_q = \frac{\sqrt{\mu_q \rho_q} S}{2M_q}. \qquad \text{(A-4)}$$

The addition of a mass, M_f, to the surface of the quartz crystal causes a change in resonant frequency, Δf, which may be expressed as follows,

$$f_q + \Delta f = \frac{\sqrt{\mu_q \rho_q} S}{2(M_q + M_f)}. \qquad \text{(A-5)}$$

Substituting equation (A-4) into (A-5) yields the following relation for Δf,

$$\Delta f = \frac{-\sqrt{\mu_q \rho_q} M_f S}{2M_q^2(1 + \frac{M_f}{M_q})}. \qquad \text{(A-6)}$$

Introducing f_q from equation (A-4) into (A-6) yields,

$$\Delta f = \frac{-f_q M_f}{M_q\left(1+\frac{M_f}{M_q}\right)}. \tag{A-7}$$

For a thin deposit, where M_f ππ M_q, equation (A-7) becomes,

$$\Delta f \approx \frac{-f_q M_f}{M_q} = \frac{-f_q M_f}{\rho_q h_q S}. \tag{A-8}$$

This is one form of Sauerbrey's equation, which indicates that the resonant frequency shift is proportional to the mass deposited on the quartz crystal.

Another common form of Sauerbrey's equation, which is often used, may be obtained by eliminating h_q using equation (A-2), which yields,

$$\Delta f = -\frac{f_q^2}{N \cdot \rho_q \cdot S} M_f, \tag{A-9}$$

where N is called the frequency constant of the specific crystal cut and is defined as,

$$N = \frac{V_{shear}}{2}. \tag{A-10}$$

For the shear mode in AT-cut in quartz, N is 1670m/sec. Equation (A-9) can be further simplified to get the relative frequency shift, $\Delta f / f_q$, by using equations (A-2), (A-3) and (A-10) to obtain,

$$\frac{\Delta f}{f_q} = -\frac{M_f}{Mq}. \tag{A-11}$$

APPENDIX B: Deviation of Kanazawa Expression (Equation 3)

In appendix A, we have shown that the resonant frequency change of the QCM is directly proportional to the mass accumulated on the sensing surface of the crystal, when the QCM is operated in vacuum or air. However, the resonant frequency of the QCM also changes, when one of its sensing surfaces is immersed in a viscous fluid. In this appendix, we will show that the resonant frequency shift caused by immersing the sensing face of a quartz crystal in a viscous fluid is a function of the material parameters of the fluid and quartz. The following derivation is based on Kanazawa's paper [19].

In writing the constitutive equations of the quartz crystal, Voigt indices are used. These indices are described in table B1,

ij or kl	x, y or z	p or q
11	xx	1
22	yy	2
33	zz	3
23 or 32	yz or zy	4
31 or 13	zx or xz	5
12 or 21	xy or yx	6

Table B1: Voigt indices defnition

The constitutive equations of the piezoelectric quartz crystal in matrix form are,

$$[T]=[C']\cdot[S]-[e']^{T}\cdot[E], \tag{B-1a}$$

and

$$[D]=\lfloor e'\rfloor\cdot[S]+\lfloor \varepsilon'\rfloor\cdot[E]. \tag{B-1b}$$

where $\lfloor C'\rfloor$ is a 6×6 quartz elastic constant matrix with C'_{pq} being its components, $\lfloor e'\rfloor$ is a 3×6 quartz piezoelectric constant matrix with e'_{kp} being its components, and $\lfloor \varepsilon'\rfloor$ is a 3×6 quartz permittivity constant matrix with ε'_{ik} being its components. $[D]$ and $[E]$ are 3×3 electric displacement and the electric field matrix with D_i and E_k being their components respectively, generated by an applied potential, ϕ, across the quartz disc. $[T]$ is a 1×6 stress matrix and T_{ij} is the stress component generated by applying the potential across the disc, on the j plane along the i direction, which is shown in figure 66. Since there is no net moment within this cube, one obtains,

$$T_{ij}=T_{ji}\ (i\neq j). \tag{B-1c}$$

$[S]$ is a 1×6 strain matrix with S_{ij} being its component as follows,

$$S_{ij}=\frac{\partial U_i}{\partial j}+\frac{\partial U_j}{\partial i}. \tag{B-1d}$$

where $U_{i,j}$ is the mechanical displacement in the i or j direction.

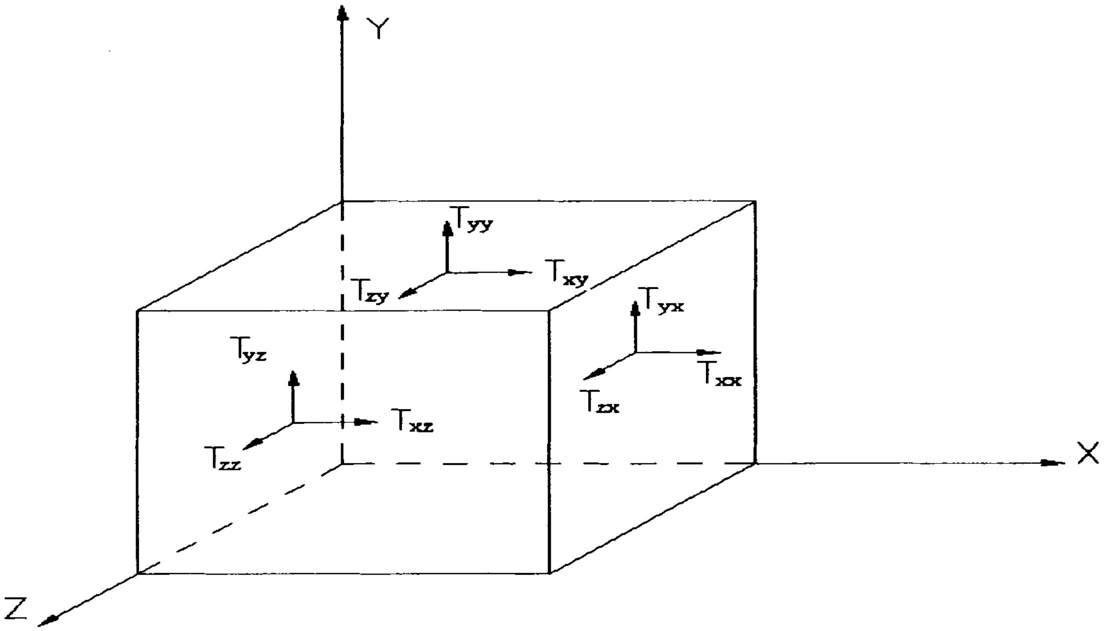

Figure B1: Stress components acting on the surfaces of an infinitesimal cube.

The elastic and piezoelectric constant as well as dielectric constants of quartz crystal can be expressed in matrix form as follows,

$$C'_{pq} = \begin{bmatrix} C'_{11} & C'_{12} & C'_{13} & C'_{14} & 0 & 0 \\ C'_{12} & C'_{11} & C'_{13} & -C'_{14} & 0 & 0 \\ C'_{13} & C'_{13} & C'_{33} & 0 & 0 & 0 \\ C'_{14} & -C'_{14} & 0 & C'_{44} & 0 & 0 \\ 0 & 0 & 0 & 0 & C'_{44} & C'_{14} \\ 0 & 0 & 0 & 0 & C'_{14} & C'_{66} \end{bmatrix}, \tag{B-2a}$$

$$e'_{kp} = \begin{bmatrix} e'_{11} & -e'_{11} & 0 & e'_{14} & 0 & 0 \\ 0 & 0 & 0 & 0 & -e'_{14} & -e'_{11} \\ 0 & 0 & 0 & 0 & 0 & 0 \end{bmatrix}, \tag{B-2b}$$

and

$$\varepsilon'_{ik} = \begin{bmatrix} \varepsilon'_{11} & 0 & 0 \\ 0 & \varepsilon'_{11} & 0 \\ 0 & 0 & \varepsilon'_{33} \end{bmatrix}. \qquad \text{(B-2c)}$$

The quartz crystal is an AT-cut sample, which is a member of the family of quartz cuts known as rotated Y-cuts. An AT-cut is a singly rotated cut, created by starting with Y-cut quartz shown in figure B1 and then rotating about the crystallographic axis, which is the z-axis in figure B1, through an angle, $\theta=-35.25^{\circ}$. This will result in differences in the elastic, piezoelectric and permittivity constants of quartz before and after the quartz crystal is cut (or the coordinate system rotated). The coordinate system associated with the AT-cut quartz disc after rotation is defined such that the y axis is normal to the quartz's interfaces and the shear stresses lies along x direction in the $x-z$ plane as shown in figure B1. Hence a coordinate transformation needs to be applied to go from the coordinate systems in figure B1 to figure B2.

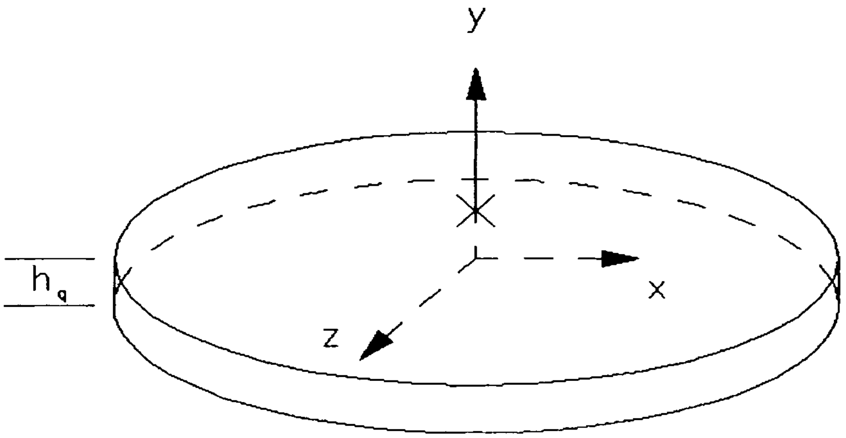

Figure B2: The coordinate system associated with the quartz disc and used in Appendices B and C.

The rotated elastic, piezoelectric and permittivity constants of y cut quartz crystal in matrix formcan be written as follows [57],

$$[C]=[M]^{-1}\cdot[C']\cdot[M], \tag{B-3a}$$

$$[e]=[A]^{-1}\cdot[e']\cdot[M], \tag{B-3b}$$

and

$$[\varepsilon]=[A]^{-1}\cdot[\varepsilon']\cdot[A], \tag{B-3c}$$

$[M]$ and $[A]$ are the transformation matrixes [57], given as.

$$[M]=\begin{bmatrix} 1 & 0 & 0 & 0 & 0 & 0 \\ 0 & \cos\theta^2 & \sin\theta^2 & -\cos\theta\sin\theta & 0 & 0 \\ 0 & \sin\theta^2 & \cos\theta^2 & \cos\theta\sin\theta & 0 & 0 \\ 0 & 2\cos\theta\sin\theta & -2\cos\theta\sin\theta & \cos\theta^2-\sin\theta^2 & 0 & 0 \\ 0 & 0 & 0 & 0 & \cos\theta & \sin\theta \\ 0 & 0 & 0 & 0 & -\sin\theta & \cos\theta \end{bmatrix} \tag{B-3d}$$

and

$$[A]=\begin{bmatrix} 1 & 0 & 0 \\ 0 & \cos\theta & -\sin\theta \\ 0 & \sin\theta & \cos\theta \end{bmatrix}, \tag{B-3e}$$

where θ, shown in figure B3, is the cutting angle with respect to the optical axis for the rotated Y-cut quartz crystal. For AT-cut, $\theta=-35.25^\circ$.

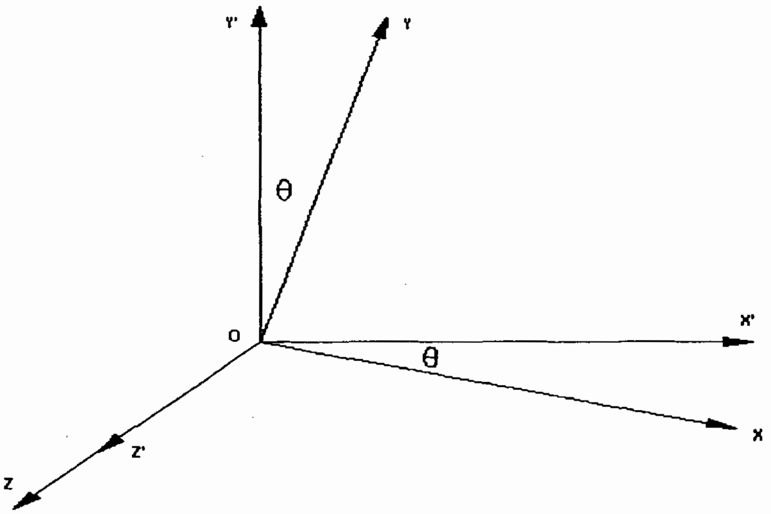

Figure B3: The unrotated and rotated coordinate systems.

Substituting equations (B-3d, 3e) into (B-3a, 3b, 3c), one obtains the rotated elastic, piezoelectric and permittivity constant matrixes,

$$[C]=\begin{bmatrix} C_{11} & C_{12} & C_{13} & C_{14} & 0 & 0 \\ C_{12} & C_{22} & C_{23} & C_{24} & 0 & 0 \\ C_{13} & C_{23} & C_{33} & C_{34} & 0 & 0 \\ C_{14} & C_{24} & C_{34} & C_{44} & 0 & 0 \\ 0 & 0 & 0 & 0 & C_{55} & C_{56} \\ 0 & 0 & 0 & 0 & C_{56} & C_{66} \end{bmatrix}, \qquad \text{(B-4a)}$$

$$[e]=\begin{bmatrix} e_{11} & e_{12} & e_{13} & e_{14} & 0 & 0 \\ 0 & 0 & 0 & 0 & e_{25} & e_{26} \\ 0 & 0 & 0 & 0 & e_{35} & e_{36} \end{bmatrix}, \qquad \text{(B-4b)}$$

and

$$[\varepsilon]=\begin{bmatrix} \varepsilon_{11} & 0 & 0 \\ 0 & \varepsilon_{22} & \varepsilon_{23} \\ 0 & \varepsilon_{23} & \varepsilon_{33} \end{bmatrix}. \qquad \text{(B-4c)}$$

Substituting equations (B-4a, 4b and 4c) into equations (1a, 1b), the constitutive equations of AT-cut quartz crystal becomes,

$$[T]=[C]\cdot[S]-e^{T}\cdot[E], \tag{B-5a}$$

and

$$[D]=e\cdot[S]+[\varepsilon]\cdot[E]. \tag{B-5b}$$

Noting that $Force = stress \times area$, the net force acting on the cube $\Delta x\Delta y\Delta z$, shown in figure 65, along the x direction can be expressed as,

$$Force = \delta T_{xx}\Delta y\Delta z + \delta T_{xy}\Delta x\Delta z + \delta T_{xz}\Delta x\Delta y\,, \tag{B-6a}$$

where the δT_{xx}, δT_{xy}, and δT_{xz} are net stress acting on the surfaces $\Delta y\Delta z$, $\Delta x\Delta z$, and $\Delta x\Delta y$ respectively, one obtains,

$$\delta T_{xx} \approx T_{xx}x + \frac{\partial T_{xx}}{\partial x}(x+\Delta x - x) - T_{xx}x = \frac{\partial T_{xx}}{\partial x}\Delta x \tag{B-6b}$$

$$\delta T_{xy} \approx T_{xy}y + \frac{\partial T_{xy}}{\partial y}(y+\Delta y - y) - T_{xy}y = \frac{\partial T_{xy}}{\partial y}\Delta y \tag{B-6c}$$

and

$$\delta T_{xz} \approx T_{xz}z + \frac{\partial T_{xz}}{\partial z}(z+\Delta z - z) - T_{xz}z = \frac{\partial T_{xz}}{\partial z}\Delta z\,. \tag{B-6d}$$

Substituting equations (B-6b, 6c, 6d) into (B-6a), noting that the mass, m, of the cube $\Delta x\Delta y\Delta z$, is given as $m = \rho_q\Delta x\Delta y\Delta z$ and using Newton's second law, $Force = mass \times accelaration$, one obtains,

$$\rho_q\frac{\partial^2 U_x}{\partial t^2} = \frac{\partial T_{xx}}{\partial x} + \frac{\partial T_{xy}}{\partial y} + \frac{\partial T_{zx}}{\partial z}\,, \tag{B-6e}$$

where ρ_q is the density of quartz and t is time.

The equations of motion in general form become,

$$T_{ij,i} = \rho_q \ddot{U}_j \, . \tag{B-7a}$$

where the comma followed by an index denotes differentiation with respect to the space coordinate i, $\ddot{U}_j$ is the second derivative of displacement U_j with respect to time t.

Since the piezoelectric crystal is a dielectric, there are no free charges, therefore Gauss's law may be expressed as,

$$D_{i,i} = 0 \, . \tag{B-7b}$$

The relationship between the electric field E_k generated by an applied potential ϕ can be expressed as follows,

$$E_k = -\phi_{,j} \, . \tag{B-7c}$$

Taking the derivative on both sides of equation (B-5a, 5b) and substituting (B-7a, 7b and 7c) and (B-1d) into equations (B-5a, 5b) yields,

$$\begin{aligned} &C_{11}U_{1,11} + (C_{12} + C_{66})U_{2,12} + (C_{13} + C_{55})U_{3,13} + (C_{14} + C_{56})U_{2,13} \\ &+ (C_{14} + C_{56})U_{3,12} + 2C_{56}U_{1,23} + C_{66}U_{1,22} + C_{55}U_{1,33} + e_{11}\phi_{,11} \\ &+ e_{26}\phi_{,22} + (e_{36} + e_{25})\phi_{,23} + e_{35}\phi_{,33} = \rho_q \ddot{U}_1 , \end{aligned} \tag{B-8a}$$

$$\begin{aligned} &C_{56}U_{3,11} + (C_{56} + C_{14})U_{1,13} + (C_{66} + C_{12})U_{1,12} + C_{66}U_{2,11} + C_{22}U_{2,22} \\ &+ (C_{23} + C_{44})U_{3,23} + 2C_{24}U_{2,23} + C_{24}U_{3,22} + C_{34}U_{3,33} + C_{44}U_{2,33} \\ &+ (e_{26} + e_{12})\phi_{,12} + (e_{36} + e_{14})\phi_{,13} = \rho_q \ddot{U}_2 , \end{aligned} \tag{B-8b}$$

$$\begin{aligned} &C_{55}U_{3,11} + (C_{55} + C_{13})U_{1,13} + (C_{56} + C_{14})U_{1,12} + C_{56}U_{2,11} + C_{24}U_{2,22} \\ &+ (C_{44} + C_{23})U_{2,23} + 2C_{34}U_{3,23} + C_{44}U_{3,22} + C_{33}U_{3,33} + C_{34}U_{2,33} \\ &+ (e_{25} + e_{14})\phi_{,12} + (e_{35} + e_{13})\phi_{,13} = \rho_q \ddot{U}_3 , \end{aligned} \tag{B-8c}$$

and

$$\begin{aligned} &e_{11}U_{1,11}+(e_{12}+e_{26})U_{2,12}+(e_{13}+e_{35})U_{3,13}+(e_{14}+e_{36})U_{2,13} \\ &+(e_{14}+e_{25})U_{3,12}+(e_{25}+e_{36})U_{1,23}+e_{26}U_{1,22}+e_{35}U_{1,33} \\ &-\varepsilon_{11}\phi_{,11}-\varepsilon_{22}\phi_{,22}-\varepsilon_{33}\phi_{,33}=0. \end{aligned} \tag{B-8d}$$

Assuming the wave propagating in the y direction only, one obtains,

$$\frac{\partial f}{\partial x}=\frac{\partial f}{\partial z}=f_{,1}=f_{,3}=0. \tag{B-9}$$

where the function $f=U,\phi$.

If a potential, ϕ, is applied along the y direction, E_y is finite and $\phi_{,1}=\phi_{,3}=0$.

Substituting equation (B-9) into equation equations (B-8a, 8b, 8c, 8d), one obtains,

$$C_{66}U_{1,22}+e_{26}\phi_{,22}=\rho_q\ddot{U}_1, \tag{B-10a}$$

$$C_{22}U_{2,22}+C_{24}U_{3,22}=\rho_q\ddot{U}_2 \tag{B-10b}$$

$$C_{24}U_{2,22}+C_{44}U_{3,22}=\rho_q\ddot{U}_3, \tag{B-10c}$$

and

$$e_{26}U_{1,22}-\varepsilon_{22}\phi_{,22}=0. \tag{B-10d}$$

Equations (B-10a-d) explicitly indicate that only U_1 is coupled to the applied electric potential ϕ across the quartz disc and $U_2=U_3=0$. Hence, for the QCM configured with electrodes on both sides of a thin disc of AT-cut quartz, the application of a voltage between these electrodes, which is along the y direction only excites one shear wave propagating along y direction with only the displacement, U_x, (see figure 66). Therefore, only the shear acoustic mode, which is termed as the thickness shear mode (TSM), associated with the propagation in the direction of the disc normal [55], will result.

Writing the time and spacial dependences out in equations (B-10a and 10d), one obtains

$$C_{66}\frac{\partial^2 U_x}{\partial y^2}+e_{26}\frac{\partial^2 \phi}{\partial y^2}=\rho_q\frac{\partial^2 U_x}{\partial t^2}, \tag{B-11a}$$

and

$$e_{26}\frac{\partial^2 U_x}{\partial y^2}-\varepsilon_{22}\frac{\partial^2 \phi}{\partial y^2}=0, \tag{B-11b}$$

Substituting equation (B-11b) into equation (B-11a) yields,

$$(C_{66}+\frac{e_{26}^2}{\varepsilon_{22}})\frac{\partial^2 U_x}{\partial y^2}=\rho_q\frac{\partial^2 U_x}{\partial t^2}. \tag{B-12}$$

Defining the stiffened quartz elastic constant as, $\mu_q=\overline{C_{66}}=C_{66}+\frac{e_{26}^2}{\varepsilon_{22}}$, equation (B-12) may be expressed as,

$$\mu_q\frac{\partial^2 U_x}{\partial y^2}=\rho_q\frac{\partial^2 U_x}{\partial t^2}. \tag{B-13}$$

Substituting equation (B-13) into equation (B-11a) and integrating with respect to y, one obtains the following equation for the x directed stress on the y plane,

$$T_{xy}=\mu_q\frac{\partial U_x}{\partial y}. \tag{B-13a}$$

The general solution of the partial differential equation (B-13) represents the superposition of two shear waves traveling in the +y and –y directions and is given as follows,

$$U_x = U_+ e^{jky} e^{j\omega t} + U_- e^{-jky} e^{j\omega t}. \tag{B-14}$$

Substituting (B-14) into (B-13), the wave number, k, describing shear wave propagation in AT-cut quartz may be expressed as follows,

$$k = \omega\sqrt{\rho_q / \mu_q}. \tag{B-15a}$$

Noting that since $V = \omega / k$, the velocity of the shear mode is given as,

$$V = \sqrt{\mu_q / \rho_q}. \tag{B-15b}$$

When the quartz crystal is excited in air, the upper and lower surface of this crystal can be considered to be stress free surfaces, therefore,

$$T_{xy}(0,t) = 0. \tag{B-16a}$$

and

$$T_{xy}(h_q,t) = 0. \tag{B-16b}$$

Evaluating the boundary condition given in (B-16a) by substituting (B-14) into (B-13a), one obtains,

$$U_+ = U_- = U_0. \tag{B-17}$$

Using equation (B-17), equation (B-14) can be expressed as,

$$U_x = 2U_0 \cos(ky) e^{j\omega t}. \tag{B-18}$$

Applying the boundary condition given in equation (B-16b) for the upper surface of the quartz crystal, by using equations (B-13a and 18), one obtains the following,

$$kh_q = n\pi . \tag{B-19}$$

Noting that for the fundamental mode of oscillation, $n = 1$, and using equation (B-15), the resonant frequency of the unloaded crystal for the fundamental mode of oscillation becomes,

$$f_q = \frac{1}{2h_q}\sqrt{\mu_q / \rho_q} . \tag{B-20}$$

When the upper surface of the quartz crystal is in contact with a Newtonian fluid, the stress free boundary condition is not valid. There will be a stress applied on the upper surface of quartz, which acts like a friction force between the quartz disc and the fluid layer, and also between the adjacent layers in the fluid. Hooke's law indicates that stress is proportional to strain in solids. This is logical since a solid undergoes only a finite amount of deformation when a stress is applied to it. This approach does not work for a fluid because a fluid continuously deforms when a shear stress is applied. It is this characteristic that distinguishes a fluid from a solid. Newton postulated (since then experimentally verified) that the shear stress needed to deform the fluid is linearly proportional to the strain rate.

Since only T_{xy} is excited with the applied electrical potential, the stress transmitted by the upper surface of the quartz disc to the fluid can be expressed as,

$$T_{xy}^{f} \propto \frac{\partial S_{xy}^{f}}{\partial t} . \tag{B-21}$$

The proportional factor is assumed to be a constant with temperature, and is called the viscosity constant, η. Fluids that have a linear relationship between stress and strain rate are called Newtonian fluids. In this case, the stress transmitted by the upper surface of the quartz disc to the fluid may be expressed using equations (B-21) and (B-5c) as,

$$T_{xy}^{f} = \eta \frac{\partial S_{xy}^{f}}{\partial t} = \eta \frac{\partial}{\partial t}\left[\frac{\partial U_{x}^{f}}{\partial y}\right] = \eta \frac{\partial}{\partial y}\left[\frac{\partial U_{x}^{f}}{\partial t}\right] = \eta \frac{\partial V_{x}^{f}}{\partial y}, \tag{B-22}$$

where V_x^f is the particle velocity in the fluid along the x direction.

For a fluid slab of thickness *dy*, the shear stress acting on the fluid slab attached to the upper surface of quartz disc gives rise to an acceleration as described by Newton's law (equation B-11) as,

$$\frac{\partial T_{xy}^{f}}{\partial y} = \rho \frac{\partial V_{x}^{f}}{\partial t}, \tag{B-23}$$

where ρ is the density of the Newtonian fluid.

Substituting (B-22) into (B-23) yields,

$$\eta \frac{\partial^2 V_{x}^{f}}{\partial y^2} = \rho \frac{\partial V_{x}^{f}}{\partial t}. \tag{B-24}$$

The general solution of the partial differential equation (B-24) is given as follows,

$$V_{x}^{f} = V_{+}^{f} e^{-\gamma(y-h_q)} e^{j\omega t} + V_{-}^{f} e^{\gamma(y-h_q)} e^{j\omega t} \tag{B-25}$$

Since V_x^f must go zero as $y \to \infty$, $V_{-}^{f} = 0$. Equation (B-25) then reduces to the following,

$$V_{x}^{f} = V_{+}^{f} e^{-\gamma(y-h_q)} e^{j\omega t} \tag{B-26}$$

Substituting equation (B-26) into equation (B-24), one obtains,

$$\gamma = \left({\omega\rho}/{2\eta} \right)^{1/2} (1+j). \qquad \text{(B-26a)}$$

Thus, equation (B-26) represents a damped shear wave radiating into the liquid from the oscillating QCM surface.

The velocity on the quartz side of the interface, can be obtained by taking the time derivative of equation (B-18) yielding,

$$V_x = \frac{\partial U_x}{\partial t} = j\omega 2U_0 \cos(ky) e^{j\omega t}. \qquad \text{(B-27)}$$

There are two boundary conditions at the fluid/solid interface, namely the continuity of the velocity and the stress. The continuity of the particle velocity $(V_x = V_x^f)$ at $y = h_q$ yields the following,

$$V_+^f = j\omega 2U_0 \cos(kh_q). \qquad \text{(B-28)}$$

Substituting equation (B-28) into (B-26) yields,

$$V_x^f = V_+^f e^{-\gamma(y-h_q)} e^{j\omega t} = j\omega 2U_0 \cos(kh_q) e^{-\gamma(y-h_q)} e^{j\omega t}. \qquad \text{(B-29)}$$

Substituting equation (B-18) into (B-13a) yields the shear stress on the quartz side of the interface,

$$T_{xy} = \mu_q \frac{\partial U_x}{\partial y} = -2U_0 \mu_q k \sin(ky) e^{j\omega t}. \qquad \text{(B-30)}$$

Substituting equation (B-29) into (B-22) and using (B-26a) yields the shear stress on the fluid side of the interface,

$$T_{xy}^{f} = \eta \frac{\partial V_x^f}{\partial y} = -2U_0 j\omega\eta\gamma \cos(kh_q)\, e^{-\gamma(y-h_q)}\, e^{j\omega t}$$
$$= 2U_0\omega\eta\cos(kh_q)\left({\omega\rho}/{2\eta}\right)^{1/2}(1-j)\, e^{-\sqrt{\left({\omega\rho}/{2\eta}\right)}(1+j)(y-h_q)}\, e^{j\omega t}. \qquad \text{(B-31)}$$

The second boundary condition requires that the stress should be continuous at solid/fluid surface, $y = h_q$. Therefore equating equation (B-30) and (B-31), one obtains,

$$-2U_0\mu_q k\sin(kh_q) = 2U_0\omega\eta\cos(kh_q)\left({\omega\rho}/{2\eta}\right)^{1/2}(1-j). \qquad \text{(B-32)}$$

Equating the real part of equation (B-32), one obtains,

$$-2U_0\mu_q k\sin(kh_q) = 2U_0\omega\eta\cos(kh_q)\left({\omega\rho}/{2\eta}\right)^{1/2}. \qquad \text{(B-33)}$$

Substituting the expression for k in equation (B-15a) into (B-33) yields,

$$\tan\left[\omega h_q\left(\sqrt{\frac{\rho_q}{\mu_q}}\right)\right] = -\left({\omega\rho\eta}/{2\rho_q\mu_q}\right)^{1/2}. \qquad \text{(B-34)}$$

The resonant angular frequency of the crystal in the liquid can be written as,

$$\omega = \omega_q + \Delta\omega, \qquad \text{(B-35)}$$

where ω_q is the angular resonant frequency of quartz in air and $\Delta\omega$ is the change in frequency caused by the fluid. Noting that $f_q = \frac{1}{2\pi}\omega_q$ and then using equation (B-20), one obtains,

$$h_q\sqrt{{\rho_q}/{\mu_q}} = {\pi}/{\omega_q}. \qquad \text{(B-36)}$$

Substituting equation (B-35) and (B-36) into equation (B-34) yields,

$$\begin{aligned}\tan\left[\left(\frac{\omega_q+\Delta\omega}{\omega_q}\right)\pi\right]&=\tan\left[\pi+\left(\frac{\Delta\omega}{\omega_q}\right)\pi\right]=\tan\left[\left(\frac{\Delta\omega}{\omega_q}\right)\pi\right]\\&=-\left(\omega_q+\Delta\omega\right)^{1/2}\left(\rho\eta/2\rho_q\mu_q\right)^{1/2}.\end{aligned}\tag{B-37}$$

When $\Delta\omega\ \pi\pi\ \omega_q$, one obtains,

$$\tan\left[\left(\frac{\Delta\omega}{\omega_q}\right)\pi\right]\approx\left(\frac{\Delta\omega}{\omega_q}\right)\pi\tag{B-38}$$

Substituting equation (B-38) into (B-37), one obtains,

$$\frac{\Delta\omega}{\omega_q}\pi=-\left(\omega_q+\Delta\omega\right)^{1/2}\left(\rho\eta/2\rho_q\mu_q\right)^{1/2}.\tag{B-39}$$

Solving for $\Delta\omega$, one obtains,

$$\Delta\omega=\frac{\omega_q^2}{2\pi^2}\left[\frac{\rho\eta}{2\rho_q\mu_q}-\sqrt{\frac{\rho\eta}{2\rho_q\mu_q}\left(\frac{\rho\eta}{2\rho_q\mu_q}+\frac{4\pi^2}{\omega_q}\right)}\right].\tag{B-40}$$

Using $\mu_q=2.947\times10^{10}kgm^{-1}s^{-2}$, $\rho_q=2648kgm^{-3}$, $\rho=1kgm^{-3}$ and

$\eta=0.001kgm^{-1}s^{-1}$ [60], one obtains,

$$\Delta\omega\approx\pm\frac{\omega_q^{\frac{3}{2}}}{\pi}\sqrt{\frac{\rho\eta}{2\rho_q\mu_q}}.\tag{B-41}$$

Using $\omega_q=2\pi f_q$, equation (B-41) can be expressed in terms of frequency,

$$\Delta f=\pm f_q^{3/2}\left(\rho\eta/\pi\rho_q\mu_q\right)^{1/2}.\tag{B-42}$$

Note that both equations (B-41) and (B-42) correspond to either an increase or decrease in the resonant frequency. This is contrast to the Kanazawa expression, which represents the change in frequency of the AT-cut quartz crystal when exposed to a Netownian fluid.

APPENDIX C: Derivation of the Expressions for the Circuit Elements of the Modified BVD Model under Simultaneous Mass and Liquid Loading (Equation 7)

Kanazawa theoretically showed that a QCM operating in a Newtonian fluid is sensitive to liquid loading, in particular the viscosity density product of the fluid. The relationship between the resonant frequency change of the QCM and the fluid characteristics has been derived in appendix B. However, the QCM operating in Newtonian fluid is not only sensitive to the liquid loading, but also to the mass loading. Martin presented an equivalent circuit model, which is given in figure 6 in chapter 2, describing the QCM simultaneously loaded by a thin surface mass layer and a Newtonian fluid. The admittance of the QCM near resonance will be derived in this appendix, based on Martin's paper [22], and the circuit elements will be explicitly related to the physical properties of the QCM and the perturbing mass and fluid.

Figure 5 in chapter 2 shows the cross sectional geometry of the QCM operating in a viscous fluid, which results in both mass loading and liquid loading on the upper sensing surface. The coordinate system is given in figures 65 and 66 in appendix B.

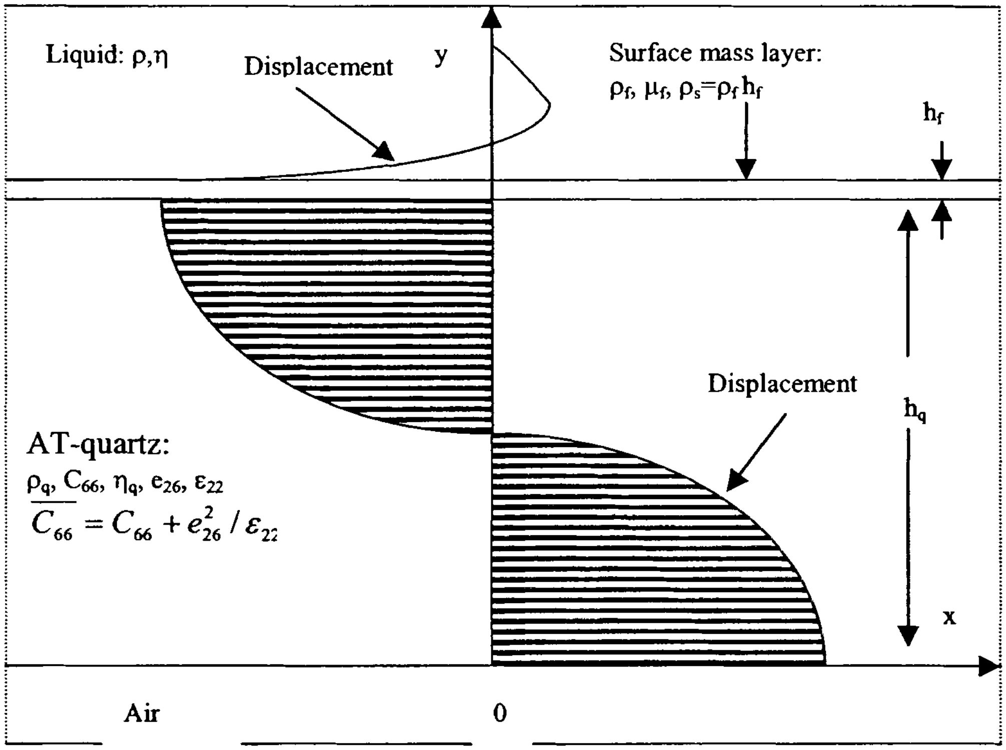

Figure 5: Shear displacement profile and cross sectional view of a QCM simultaneously loaded on one side by a surface mass layer and a contacting Newtonian liquid.

The constitutive equations of the AT-cut quartz crystal has been obtained in appendix B (B-5a, 5b) as follows,

$$[T]=[C]\cdot[S]-e^{T}\cdot[E], \tag{C-1a}$$

and

$$[D]=e\cdot[S]+[\varepsilon]\cdot[E]. \tag{C-1b}$$

where $[C]$ is a 6×6 quartz elastic constant matrix with C_{pq} being its components, $[e]$ is a 3×6 quartz piezoelectric constant matrix with e_{kp} being its components, and $[\varepsilon]$ is a 3×6 quartz permittivity constant matrix with ε_{ik} being its components. $[D]$ and $[E]$ are 3×3 electric displacement and the electric field matrix with D_i and E_k being their components respectively, generated by an applied potential, ϕ, across the quartz disc. $[T]$ and $[S]$ are 1×6 stress and strain matrixes with T_{ij} and S_{ij} being their component.

The amplitude of acoustic waves propagating in the quartz crystal will attenuate gradually due to its elastic damping property. Hence, the constitutive equations (C-1a) for the loss less quartz crystal needs to be modified. The elastic damping usually depends, in a rather complicated manner, upon temperature, as well as the frequency and type of vibration. However, the acoustic attenuation in the quartz crystal may be adequately described by a viscous damping term [58]. The form of the viscous damping term in the constitutive equation may be introduced by considering the physical analogue of the viscosity of the Newtonian fluid in appendix B (equation B-21), $\eta_{pq} \frac{\partial S_{ij}}{\partial t}$, where η_{pq} is the viscosity constant matrix of the quartz crystal instead of the Newtonian fluid. Assuming harmonic time variation $e^{j\omega t}$, the constitutive equation (C-1a) becomes,

$$T_{ij} = C_{pq} S_{ij} + i\omega\eta_{pq} S_{ij} - e_{kp}{}^{T} E_k, \tag{C-2}$$

where t is time.

Following the same derivation process in appendix B, one obtains equation (B-11a, 11b) with shear viscosity term $\eta_{66} = \eta_q$,

$$(C_{66} + j\omega\eta_q)\frac{\partial^2 U_x}{\partial y^2} + e_{26}\frac{\partial^2 \phi}{\partial y^2} = \rho_q \frac{\partial^2 U_x}{\partial t^2}, \tag{C-3a}$$

and

$$e_{26}\frac{\partial^2 U_x}{\partial y^2} - \varepsilon_{22}\frac{\partial^2 \phi}{\partial y^2} = 0, \tag{C-3b}$$

The shear quartz elastic constant becomes complex and can be expressed as,

$$C_{66}^{*} = C_{66} + j\omega\eta_q. \tag{C-3c}$$

Assuming harmonic time variation $e^{j\omega t}$, substituting equation (C-3b) into equation (C-3a) yields,

$$\overline{\overline{C_{66}}}\frac{\partial^2 U_x}{\partial y^2} = -\omega^2 \rho_q U_x, \tag{C-4a}$$

where $\overline{\overline{C_{66}}} = C_{66} + \frac{e_{26}^2}{\varepsilon_{22}} + j\omega\eta_q$. Equation (C-4a) is analogous to equation (B-12) with the viscosity constant introduced along with a $e^{j\omega t}$ time variation. $\overline{\overline{C_{66}}}$, the stiffened complex quartz elastic constant may be written as,

$$\overline{\overline{C_{66}}} = \overline{C_{66}}(1 + j\xi), \tag{C-4b}$$

where ξ is defined as the quartz loss parameter and given as follows,

$$\xi = \frac{\omega\eta_q}{\overline{C_{66}}}. \tag{C-4c}$$

The quartz shear displacement U_x can be expressed by the solution of equation (C-4a), which shows the superposition of two shear waves propagating in opposite directions along the y axis,

$$U_x = \left(A e^{jky} + B e^{-jky}\right) e^{j\omega t}, \tag{C-5}$$

where A and B are amplitudes of the two shear waves and ω is the angular excitation frequency $(\omega = 2\pi f)$. Substituting (C-5) into (C-4a), the wave number, k, describing shear wave propagation in AT-cut quartz may be expressed as follows,

$$k = \omega \sqrt{\rho_q / C_{66}} . \tag{C-6}$$

The relationship between the potential, ϕ, and the displacement U_x is the same as equation (B-9b) and is given as follows,

$$0 = e_{26} \frac{\partial^2 U_x}{\partial y^2} - \varepsilon_{22} \frac{\partial^2 \phi}{\partial y^2} . \tag{C-7a}$$

Integrating equation (C-7a) twice over y, one obtains the electrical potential, ϕ, in the piezoelectric quartz as follows,

$$\phi = \left(\frac{e_{26}}{\varepsilon_{22}} U_x + Cy + D \right) e^{j\omega t}, \tag{C-7b}$$

where C and D are integration constants.

The fluid velocity, V_x^f, is similarl to equation (B-26) in appendix B and is given as,

$$V_x^f = E e^{-\gamma (y - h_q)} e^{j\omega t} . \tag{C-8}$$

E is the amplitude of V_x^f and γ is a complex decay constant for the liquid velocity field, given as,

$$\gamma = \left(\frac{\omega\rho}{2\eta} \right)^{1/2} (1+j). \tag{C-9}$$

where ρ and η are the fluid mass density and shear viscosity, respectively.

Figure 5 shows a four-layer problem with air, the quartz disc, the mass layer and the fluid respectively. The addition of a finite thickness layer between the quartz disc and the fluid introduces an extra interface with two associated boundary conditions, which are at the upper and bottom surface of the mass layer. When the thickness of the mass layer, h_f, is much smaller compared to the acoustic wavelength in it, the mass of the mass layer can be considered to be concentrated in an infinitesimally thin sheet at the quartz/liquid interface, $y = h_q$. Thus the four layer problem reduces to a three layer problem.

The **first** boundary condition is that the displacement should be continuous across the solid/fluid interface (the non-slip condition), $y = h_q$, hence the particle velocity across the interface also should be continuous. Substituting $V_x = j\omega U_x$ into equation (C-5), one obtains,

$$V_x = j\omega \left(A e^{jky} + B e^{-jky} \right) e^{j\omega t}, \tag{C-10}$$

Equating equation (C-8) and (C-10) at the upper quartz surface, $y = h_q$, yields the following relation for the **first** boundary condition,

$$A e^{jkh_q} + B e^{-jkh_q} + j\frac{E}{\omega} = 0. \tag{C-11}$$

Since the thickness of the mass layer is very thin, the shear stress component T_{xy} acting on the thin mass sheet by the quartz disc and the fluid can be considered to vary linearly across the mass sheet, h_f, one obtains,

$$\frac{\partial T_{xy}}{\partial y} = \frac{T_L - T_Q}{h_f}, \tag{C-12}$$

Where T_L is the shear stress imposed in the x direction on the mass layer by the liquid, T_Q is the shear stress exerted on the mass layer by the quartz disc. In this case, the Newton's one-dimensional continuum equation of motion, (B-11)

$\frac{\partial T_{xy}}{\partial y} = \rho_f \frac{\partial^2 U_x}{\partial t^2}$, reduces to,

$$T_L - T_Q = \rho_f h_f \frac{\partial^2 U_x}{\partial t^2} = \rho_s \frac{\partial V_x}{\partial t}, \tag{C-13}$$

where ρ_f is the density of the mass layer and $\rho_S = \rho_f h_f$.

From the piezoelectric constitutive equation (C-3), and using equations B-8 and B-5c, the shear stress T_Q exerted by the quartz on the mass layer is,

$$T_Q = C_{66}^{*} \frac{\partial U_x}{\partial y}\bigg|_{y=h_q} + e_{26} \frac{\partial \phi}{\partial y}\bigg|_{y=h_q}. \tag{C-14}$$

Substituting equation (C-5) and (C-7) into equation (C-14) yields,

$$T_Q = \left[jk\left(A e^{jkh_q} - B e^{-jkh_q}\right)\left(C_{66}^{*} + \frac{e_{26}^2}{\varepsilon_{22}}\right) + e_{26} C \right] e^{j\omega t}. \tag{C-15}$$

The shear stress exerted on the mass layer by the liquid can be obtained from equation B-22 in appendix B as follows,

$$T_L = \eta \frac{\partial V_x^f}{\partial y}\Bigg|_{y=h_q}. \tag{C-16}$$

Substituting equation (C-8) in to equation (C-16) and the right side of equation (C-13), one obtains,

$$T_L = -\eta\gamma E e^{j\omega t} \tag{C-17}$$

and

$$\rho_s \frac{\partial V_x}{\partial t} = \rho_s j\omega E e^{j\omega t}. \tag{C-18}$$

Substituting equations (C-15, 17 and 18) into equation (C-13) yields the following expression for the **second** boundary condition,

$$jk\overline{\overline{C_{66}}}\left(A e^{jkh_q} - B e^{-jkh_q}\right) + e_{26}C + (\eta\gamma + j\omega\rho_s)E = 0. \tag{C-19}$$

The **third** boundary condition is that the stress at the quartz/air interface, $y = 0$ is zero. This condition may be obtained by setting $h_q = 0$, in equation C-15, which yields,

$$jk\overline{\overline{C_{66}}}(A - B) + e_{26}C = 0. \tag{C-20}$$

The **fourth** and **fifth** boundary conditions require that the electrical potential at the upper ($y = h_q$) and lower ($y = 0$) quartz surfaces match the applied potential, which is $-\phi_0 e^{j\omega t}$ and $\phi_0 e^{j\omega t}$ respectively. Substituting equation (C-5) into (C-7) and applying the electrical potential boundary conditions at $y = 0$ and $y = h_q$ one obtains,

$$\frac{e_{26}}{\varepsilon_{22}}(A e^{jkh_q} + B e^{-jkh_q}) + Ch_q + D = -\phi_0 \tag{C-21}$$

and

$$\frac{e_{26}}{\varepsilon_{22}}(A+B)+D=\phi_0. \tag{C-22}$$

The boundary condition equations (C-11, and 19-22) constitute five linear equations with the five unknowns A through E. These five unknowns can be obtained by solving these equations simultaneously, where the quartz shear displacement field U_x in equation C-5 can be expressed by the solution of A and B, the applied potential field ϕ in equation C-7b can be expressed by the solution of C and D, the particle velocity field of the fluid V_x^f in equation C-8 can be expressed by the solution of E. Solving these equations by a full Gauss-Jordan elimination is quite tedious.

Fortunately, the following analysis of the admittance of the QCM will indicate that only the constant C is needed.

From Gauss' law and using equation (C-7), the surface charge density induced on the lower ($y=0$) electrode can be expressed as follows,

$$q_s=-\varepsilon_{22}\left.\frac{\partial\phi}{\partial y}\right|_{y=0}=-\varepsilon_{22}\left(\frac{e_{26}}{\varepsilon_{22}}\left.\frac{\partial U_x}{\partial y}\right|_{y=0}+C\right)e^{j\omega t}. \tag{C-23}$$

Since the electrodes can be assumed infinitesimally thin and part of the quartz substrate, the lower surface of the quartz disc becomes a stress-free surface, one can observe from equation (B-13a) that $\frac{\partial U_x}{\partial y}\big|_{y=0}=0$, equation (C-23) reduces to,

$$q_s=-\varepsilon_{22}Ce^{j\omega t}. \tag{C-24}$$

The current flow out of the lower electrode (and into the upper electrode) can be expressed as,

$$I=\frac{\partial q_s}{\partial t}S=j\omega q_sSe^{j\omega t}, \tag{C-25}$$

where S is the electrode area.

Noting that the applied voltage, V, across the quartz crystal can be expressed as,

$$V = \phi_0 e^{j\omega t} - (-\phi_0 e^{j\omega t}) = 2\phi_0 e^{j\omega t} \tag{C-26}$$

The admittance, defined as the ratio of terminal current I to applied potential V can be expressed from equations C24-26 as,

$$Y = \frac{I}{V} = \frac{\frac{\partial q_s}{\partial t} S e^{j\omega t}}{2\phi_0 e^{j\omega t}} = \frac{-j\omega\varepsilon_{22} SC}{2\phi_0}. \tag{C-27}$$

It is obvious that the admittance of the QCM is only dependent on the constant C. Solving the boundary condition equations for C, one obtains,

$$\begin{aligned} C = {} & 2\phi_0 \overline{\overline{\overline{C_{66}}}} \varepsilon_{22} k \left[jk\overline{\overline{\overline{C_{66}}}} \sin kh_q + \omega(\eta\gamma + j\omega\rho_s)\cos kh_q \right] / \\ & \left\{ \begin{matrix} e_{26}^2 \left[jk\overline{\overline{\overline{C_{66}}}}(2 - 2\cos kh_q) + \omega(\eta\gamma + j\omega\rho_s)\sin kh_q \right] - \\ \overline{\overline{\overline{C_{66}}}} \varepsilon_{22} kh_q \left[jk\overline{\overline{\overline{C_{66}}}} \sin kh_q + \omega(\eta\gamma + j\omega\rho_s)\cos kh_q \right] \end{matrix} \right\}. \end{aligned} \tag{C-28}$$

Substituting equation (C-28) into equation (C-27), one obtains,

$$\begin{aligned} Y = {} & -j\omega S\varepsilon_{22}^2 \overline{\overline{\overline{C_{66}}}} k \left[jk\overline{\overline{\overline{C_{66}}}} \sin kh_q + \omega(\eta\gamma + j\omega\rho_s)\cos kh_q \right] / \\ & \left\{ \begin{matrix} e_{26}^2 \left[jk\overline{\overline{\overline{C_{66}}}}(2 - 2\cos kh_q) + \omega(\eta\gamma + j\omega\rho_s)\sin kh_q \right] - \\ \overline{\overline{\overline{C_{66}}}} \varepsilon_{22} kh_q \left[jk\overline{\overline{\overline{C_{66}}}} \sin kh_q + \omega(\eta\gamma + j\omega\rho_s)\cos kh_q \right] \end{matrix} \right\}. \end{aligned} \tag{C-29}$$

Referring to figure 6 in chapter 2, the admittance of the modified BVD model can be expressed as,

$$Y(\omega) = j\omega C_0' + \frac{1}{Z_m} \tag{C-30}$$

where $C_0' = C_0 + C_p$, and

$$Z_m = (R_1 + R_2) + j\omega(L_1 + L_2 + L_3) + \frac{1}{j\omega C_1}. \tag{C-30a}$$

The circuit elements $C_0^{'}$, C_1, R_1, R_2, L_1, L_2, and L_3 may be obtained by comparing equation (C-29) to equation (C-30). Since equation (C-29) is quite complicated, it needs to be simplified before the comparison with equation (C-30) is made. Using equation (C-6), the frequency dependent phase shift undergone by the shear wave in propagating across the lossy quartz disc can be defined as,

$$\varphi = kh_q = \omega h_q \left(\rho_q \big/ \overline{\overline{C}}_{66} \right)^{1/2}, \tag{C-31a}$$

Using equation (C-4c), the frequency dependent phase shift undergone by the shear wave in propagating across a loss less quartz disc can be expressed as,

$$\varphi_0^2 = \varphi^2 (1 + j\xi). \tag{C-31b}$$

The electromechanical coupling constant, which is a measure of the degree of the coupling between the electrical and mechanical energy in an AT-cut quartz crystal, can be defined as [58],

$$K^2 = e_{26}^2 \big/ \left(\overline{\overline{C}}_{66} \varepsilon_{22} \right). \tag{C-32a}$$

Using equation (C-4c), the electromechanical coupling constant, K_0^2, for the loss less quartz can be obtained as,

$$K_0^2 = K^2 (1 + j\xi) = e_{26}^2 \big/ \left(\overline{C}_{66} \varepsilon_{22} \right). \tag{C-32b}$$

Examination of equation (C-29) reveals that the influence of the mass and liquid perturbation can be incorporated into a single complex factor, Λ, which can be expressed follows,

$$\Lambda = \frac{\omega(\eta\gamma + j\omega\rho_s)}{jk\overline{\overline{C}}_{66}} = \Lambda_r - j\Lambda_i \tag{C-33}$$

Substituting equations (C-6) and (C-9) for k and γ into equation (C-33), one obtains,

$$\Lambda_r = \frac{\omega\rho_s + \sqrt{\omega\rho\eta/2}}{\sqrt{\overline{\overline{C}}_{66}\rho_q}}, \tag{C-33a}$$

and

$$\Lambda_i = \left(\frac{\omega\rho\eta}{2\overline{\overline{C}}_{66}\rho_q}\right)^{1/2}. \tag{C-33b}$$

Dividing the numerator and denominator of C-29 by $jk\overline{\overline{C}}_{66}$, and substituting the expressions of φ and Λ, one obtains,

$$\textit{numerator} = -j\omega S\varepsilon_{22}^2\overline{\overline{C}}_{66}k[\sin\varphi + \Lambda\cos\varphi] \tag{C-34a}$$

and

$$\textit{denominator} = e_{26}^2(2 - 2\cos\varphi + \Lambda\sin\varphi) - \overline{\overline{C}}_{66}\varepsilon_{22}\varphi(\sin\varphi + \Lambda\cos\varphi). \tag{C-34b}$$

Dividing equations (C-34a, b) by $\overline{\overline{C}}_{66}\varepsilon_{22}$, and substituting the expressions of K^2, one obtains,

$$\textit{numerator} = -j\omega S\varepsilon_{22}k[\sin\varphi + \Lambda\cos\varphi] \tag{C-34c}$$

$$\textit{denominator} = K^2(2 - 2\cos\varphi + \Lambda\sin\varphi) - \varphi(\sin\varphi + \Lambda\cos\varphi) \tag{C-34d}$$

Dividing equations (C-34c, d) by h_q, and noting that $C_0 = \frac{\varepsilon_{22}S}{h_q}$, one obtains,

$$\textit{numerator} = -j\omega C_0k[\sin\varphi + \Lambda\cos\varphi] \tag{C-34e}$$

$$\textit{denominator} = \frac{K^2}{h_q}(2 - 2\cos\varphi + \Lambda\sin\varphi) - \frac{\varphi}{h_q}(\sin\varphi + \Lambda\cos\varphi) \tag{C-34f}$$

Substituting equations C-34e, f and C-31a into equation (C-29), the admittance for a QCM under simultaneous mass and liquid loading becomes,

$$Y(\omega)=-j\omega\frac{C_0\varphi(\sin\varphi+\Lambda\cos\varphi)}{K^2(2-2\cos\varphi+\Lambda\sin\varphi)-\varphi(\sin\varphi+\Lambda\cos\varphi)}. \tag{C-35}$$

where $C_0=\varepsilon_{22}S/h_q$ is the static capacitance of the quartz disc.

Since $Y(\omega)$ in equation (C-35) is the admittance of quartz crystal itself and C_p in equation (C-30) is the parasitic capacitance of the test fixture, neglecting of C_p will not influence the accuracy of analysis. Equating equations (C-30) and (C-35), one obtains follows,

$$j\omega C_0+\frac{1}{Z_m}=-j\omega\frac{C_0\varphi(\sin\varphi+\Lambda\cos\varphi)}{K^2(2-2\cos\varphi+\Lambda\sin\varphi)-\varphi(\sin\varphi+\Lambda\cos\varphi)}, \tag{C-36}$$

After further simplification, equation (C-36) becomes,

$$\frac{1}{Z_m}=-j\omega C_0\left[1+\frac{\varphi(\sin\varphi+\Lambda\cos\varphi)}{K^2(2-2\cos\varphi+\Lambda\sin\varphi)-\varphi(\sin\varphi+\Lambda\cos\varphi)}\right]. \tag{C-37}$$

Dividing the numerator and denominator of the right side of (C-37) by $\sin\varphi$, and noting that $\tan\frac{\varphi}{2}=\frac{1-\cos\varphi}{\sin\varphi}$, one obtains,

$$\frac{1}{Z_m}=-j\omega C_0\left[\frac{K^2(2\tan\frac{\varphi}{2}+\Lambda)}{K^2(2\tan\frac{\varphi}{2}+\Lambda)-\varphi(1+\Lambda\cot\varphi)}\right]. \tag{C-38}$$

Solving equation (C-38) for Z_m, one obtains,

$$Z_m = \frac{j}{\omega C_0}\left(1 - \frac{\varphi(1+\Lambda\cot\varphi)}{K^2(2\tan\frac{\varphi}{2}+\Lambda)}\right). \qquad \text{(C-39)}$$

For loss less QCM without a mass or liquid perturbation, $\Lambda = 0$, $\varphi = \varphi_0$ and $K = K_0$, equation (C-39) reduces to the follows,

$$Z_m = \frac{j}{\omega C_0}\left(1 - \frac{\varphi_0}{K_0{}^2 2\tan\frac{\varphi_0}{2}}\right), \qquad \text{(C-39a)}$$

The series resonant frequency can be defined by requiring that, $Z_m = 0$. Therefore one obtains from equation (C-39a) the following,

$$1 = \frac{K_0{}^2\tan\frac{\varphi_0}{2}}{\varphi_0/2}, \qquad \text{(C-39b)}$$

Equation (C-39b) is a transcendental equation and generally does not have a simple closed form solution. For AT cut quartz crystal, $C_{66} = 2.901\times10^{10} N*m^{-2}$, $e_{26} = -0.095 Coulomb*m^{-2}$, and $\varepsilon_{22} = 39.82\times10^{-12} F*m^{-1}$, which are given by Tiersten [61], the coupling constant, K_0^2, given in equation (C-32b) with $\eta_q = 0$ can be calculated to be 0.0176. Substituting K_0 into equation (C-39b) and solving for φ_0, one obtains $\varphi_0 = 0.9937n\pi(n = 1,3,5...)$. The trigonometric functions in equation (C-39) can then be expanded as follows,

$$\tan(\varphi/2) \approx \frac{4\varphi}{(n\pi)^2 - \varphi^2} \qquad \text{(C-40a)}$$

and

$$\cot\varphi \approx \frac{-2\varphi}{(n\pi)^2-\varphi^2}. \tag{C-40b}$$

The detailed derivation of equations (C-40a, b) is given in appendix D.

Substituting equations (C-40a, 40b) into equation (C-38), one obtains

$$Z_m = \frac{j}{\omega C_0}\left(1-\frac{\varphi\left[(n\pi)^2-\varphi^2-2\varphi\Lambda\right]}{K^2\left[8\varphi+\Lambda\left((n\pi)^2-\varphi^2\right)\right]}\right), \tag{C-41}$$

Since $\varphi = 0.9937n\pi(n=1,3,5...)$, the term $(n\pi)^2-\varphi^2$ is very small. On the other hand, the mass (ρ_s) and liquid loading $(\rho\eta)$ are assumed very small compared to the product of density and elasticity of quartz crystal $(\mu_q\rho_q)$, the perturbation factor Λ in equation (C-33) also is a very small quantity. Therefore, the product $\Lambda[(n\pi)^2-\varphi^2]$ is a term up to the second order in very small quantities compared to Λ and $(n\pi)^2-\varphi^2$, hence, it can be neglected. Equation (C-41) becomes,

$$Z_m \approx \frac{j}{\omega C_0}\left(1-\frac{(n\pi)^2-\varphi^2-2\varphi\Lambda}{8K^2}\right). \tag{C-41a}$$

Since the electrically excited resonance (i.e., maximum electrical admittance or minimum impedance) occurs near the series resonance frequency of the QCM [56], the phase shift across the QCM can be approximated when the numerator of equation (C-41a) equals zero,

$$\varphi^2(\omega_s) = (n\pi)^2-8K^2-2\varphi(\omega_s)\Lambda, \tag{C-42a}$$

For loss less QCM without perturbation, $\rho_s = 0$ and $\rho = 0$. Therefore, $\Lambda = 0$, equation (C-42a) becomes,

$$\varphi_0{}^2(\omega_s) = (n\pi)^2 - 8K_0{}^2 \tag{C-42b}$$

where $\omega_s = 2\pi f_s$ is the angular series resonant frequency of the unperturbed QCM.

Substituting equation (C-42b) into equation (C-31b), the phase shift of the lossy QCM at series resonant frequency can be expressed as follows,

$$\varphi^2(\omega_s) = \frac{\varphi_0^2(\omega_s)}{1+j\xi} = \frac{(n\pi)^2 - 8K_0^2}{1+j\xi}. \tag{C-42c}$$

From equation (C-31a), the ratio of the phase shift of the lossy QCM at any frequency to the phase shift of the lossy QCM at series resonant frequency can be expressed as follows,

$$\frac{\varphi^2(\omega)}{\varphi^2(\omega_s)} = \frac{(\omega)^2 h_q^2 \left(\rho_q \Big/ \overline{\overline{C}}_{66} \right)}{(\omega_s)^2 h_q^2 \left(\rho_q \Big/ \overline{\overline{C}}_{66} \right)} = \frac{(\omega)^2}{(\omega_s)^2}. \tag{C-42d}$$

Substituting equation (C-42c) into (C-42d), the phase shift of the lossy QCM at any frequency can be expressed as follows,

$$\varphi^2(\omega) = \frac{(n\pi)^2 - 8K_0^2}{1+j\xi} \left(\frac{\omega}{\omega_s} \right)^2. \tag{C-43}$$

Substituting $\varphi^2(\omega)$ into equation (C-41a) and using equation (C-32b), one obtains,

$$
\begin{aligned}
Z_m &= \frac{j\left[8K^2-\left((n\pi)^2-\varphi^2\right)+2\varphi\Lambda\right]}{8K^2\omega C_0} \\
&= \frac{j}{\omega C_0 8K_0^2}\left\{8K_0^2-(1+j\xi)\left[(n\pi)^2-\varphi^2\right]+2\varphi(1+j\xi)\Lambda\right\}
\end{aligned}
\tag{C-44a}
$$

Since $(n\pi)^2-\varphi^2$, ξ (see C-4c) and Λ (see C-33) are very small quantities, the product of any two of them is a second order term, these quantities can be neglected. Equation (C-44a) then simplifies to the following,

$$
\begin{aligned}
Z_m &= \frac{j}{\omega C_0 8K_0^2}\left\{8K_0^2-(1+j\xi)\left[(n\pi)^2-\varphi^2\right]+2\varphi(1+j\xi)\Lambda\right\} \\
&\approx \frac{j}{\omega C_0 8K_0^2}\left\{8K_0^2-\left[(n\pi)^2-\varphi^2\right]+2\varphi\Lambda\right\} \\
&= \frac{1}{j\omega}\left(\frac{(n\pi)^2}{8K_0^2C_0}\right)+\frac{j}{\omega C_0 8K_0^2}\left[8K_0^2+\varphi^2+2\varphi\Lambda\right],
\end{aligned}
\tag{C-44b}
$$

Substituting equation (C-33) into equation (C-44b) and rearrange term, one obtains,

$$
\begin{aligned}
Z_m &= \frac{1}{j\omega}\left(\frac{(n\pi)^2}{8K_0^2C_0}\right)+\frac{j}{\omega C_0 8K_0^2}\left[8K_0^2+\varphi^2+2\varphi\Lambda\right] \\
&= \frac{1}{j\omega}\left(\frac{(n\pi)^2}{8K_0^2C_0}\right)+\frac{j}{\omega C_0 8K_0^2}\left[8K_0^2+\varphi^2+2\varphi\Lambda_r\right]+\frac{\varphi\Lambda_i}{\omega C_0 4K_0^2}.
\end{aligned}
\tag{C-44c}
$$

Comparing between equation C-44c and C-30a shows that the sum of second and third term in C-44c equals to the sum of the first and second term, which is $R_1+R_2+j\omega(L_1+L_2+L_3)$, in equation (C-30a) and needed to be further simplified. Equating the second and third term of equation (C-44c) to Z_{m1}, Z_{m2} and Z_{m3} respectively, one obtains,

$$
Z_{m1}=\frac{j}{\omega C_0 8K_0^2}\left(8K_0^2+\varphi^2\right), \tag{C-45a}
$$

$$Z_{m2} = \frac{j\varphi\Lambda_r}{\omega C_0 4K_0^2}, \qquad \text{(C-45b)}$$

and

$$Z_{m3} = \frac{\varphi\Lambda_i}{\omega C_0 4K_0^2}. \qquad \text{(C-45c)}$$

Noting that ξ^2 and $K_0^2\xi$ are terms up to the second order in very small quantities, which can be neglected, equation (C-43) can be simplified as,

$$\begin{aligned}\varphi^2(\omega) &= \frac{(n\pi)^2 - 8K_0^2}{1+j\xi}\left(\frac{\omega}{\omega_s}\right)^2 = \frac{(1-j\xi)\left[(n\pi)^2 - 8K_0^2\right]}{1+\xi^2}\left(\frac{\omega}{\omega_s}\right)^2 \\ &\approx \left[(n\pi)^2 - 8K_0^2\right]\left(\frac{\omega}{\omega_s}\right)^2 - j\xi(n\pi)^2\left(\frac{\omega}{\omega_s}\right)^2,\end{aligned} \qquad \text{(C-46a)}$$

Substituting equation (C-46a) into equation (C-45a), one obtains,

$$Z_{m1} = \frac{j}{\omega C_0 8K_0^2}\left\{8K_0^2 + \left[(n\pi)^2 - 8K_0^2\right]\left(\frac{\omega}{\omega_s}\right)^2 - j\xi(n\pi)^2\left(\frac{\omega}{\omega_s}\right)^2\right\}, \qquad \text{(C-46b)}$$

When the QCM operates near its series resonant frequency, $\omega \approx \omega_s$ and noting that $8K_0^2 \approx 0.14$, one may obtain $8K_0^2\left[1-\left(\frac{\omega}{\omega_s}\right)^2\right] \approx 0$. Equation (C-46b) can be simplified as,

$$Z_{m1} \approx \frac{j\omega(n\pi)^2}{8K_0^2\omega_s^2 C_0} + \frac{\omega\xi(n\pi)^2}{8K_0^2\omega_s^2 C_0}, \qquad \text{(C-46c)}$$

Using equations (C-42b) and noting that $8K_0^2 \approx 0.14$, which is much smaller than $n\pi$, one obtains $\varphi(\omega_s) \approx n\pi$. Equation (C-42d) can be expressed as,

$$\varphi(\omega) = n\pi\left(\frac{\omega}{\omega_s}\right), \tag{C-47a}$$

Substituting equation (C-47a) into equations (C-45b, c), one obtains,

$$Z_{m2} = \frac{jn\pi\Lambda_r}{4K_0^2\omega_s C_0}, \tag{C-47b}$$

and

$$Z_{m3} = \frac{n\pi\Lambda_i}{4K_0^2\omega_s C_0}. \tag{C-47c}$$

Substituting Z_{m1}, Z_{m2} and Z_{m3} into equation (C-44c), one obtains,

$$Z_m \approx \left(\frac{(n\pi)^2\omega\xi}{8K_0^2\omega_s^2C_0} + \frac{n\pi\Lambda_i}{4K_0^2\omega_s C_0}\right) + j\omega\left(\frac{(n\pi)^2}{8K_0^2\omega_s^2C_0} + \frac{n\pi\Lambda_r}{4K_0^2\omega_s\omega C_0}\right) + \frac{1}{j\omega}\left(\frac{(n\pi)^2}{8K_0^2C_0}\right). \tag{C-48}$$

Comparing equation (C-48) and equation (C-30a), one may obtain,

$$\frac{1}{C_1} = \frac{(n\pi)^2}{8K_0^2C_0}, \tag{C-49a}$$

$$R_1 = \frac{(n\pi)^2\omega\xi}{8K_0^2\omega_s^2C_0}, \tag{C-49b}$$

$$L_1 = \frac{(n\pi)^2}{8K_0^2\omega_s^2C_0}, \tag{C-49c}$$

$$R_2 = \frac{n\pi\Lambda_i}{4K_0^2\omega_s C_0}, \tag{C-49d}$$

and

$$L_2 + L_3 = \frac{n\pi\Lambda_r}{4K_0^2\omega_s\omega C_0}. \tag{C-49e}$$

From equation (C-49a), one may obtains,

$$C_1 = \frac{8K_0^2 C_0}{(n\pi)^2}, \tag{C-50a}$$

Substituting equation (C-50a) into equation (C-49b) and noting that $\xi = \frac{\omega\eta_q}{\bar{\bar{C}}_{66}}$, (C-4c), one obtains,

$$R_1 = \frac{(n\pi)^2\omega\xi}{8K_0^2\omega_s^2 C_0} = \frac{\omega\xi}{C_1\omega_s^2} = \frac{\eta_q}{\bar{\bar{C}}_{66}C_1}\left(\frac{\omega}{\omega_s}\right)^2, \tag{C-50b}$$

Substituting equation (C-50a) into equation (C-49c), on obtains,

$$L_1 = \frac{(n\pi)^2}{8K_0^2\omega_s^2 C_0} = \frac{1}{\omega_s^2 C_1}, \tag{C-50c}$$

Substituting equation (C-50c) into equation (C-49d) and using equation (C-33b), one may obtains,

$$R_2 = \frac{n\pi\Lambda_i}{4K_0^2\omega_s C_0} = \frac{2}{\omega_s C_1 n\pi}\left(\frac{\omega\rho\eta}{2\bar{\bar{C}}_{66}\rho_q}\right)^{1/2} = \frac{\omega_s L_1}{n\pi}\left(\frac{2\omega\rho\eta}{\bar{\bar{C}}_{66}\rho_q}\right)^{1/2}, \tag{C-50d}$$

Substituting equation (C-50c) in to equation (C-49e) and using equation (C-33a), one may obtains,

$$L_2 + L_3 = \frac{n\pi\Lambda_r}{4K_0^2\omega_s\omega C_0} = \frac{2L_1\omega_s}{n\pi\omega}\left(\frac{\omega\rho_s + \sqrt{\omega\rho\eta/2}}{\sqrt{\bar{\bar{C}}_{66}\rho_q}}\right), \tag{C-50e}$$

The modified BVD model in figure 6 indicates that L_2 represents the liquid loading and L_3 represents the mass loading, therefore equation (C-50e) can be split into two equations as follows,

$$L_2 = \frac{\omega_s L_1}{n\pi}\left(\frac{2\rho\eta}{\omega\overline{\overline{C}}_{66}\rho_q}\right)^{1/2}, \tag{C-50f}$$

and

$$L_3 = \frac{2\omega_s L_1 \rho_s}{n\pi\sqrt{\overline{\overline{C}}_{66}\rho_q}}. \tag{C-50g}$$

Circuit elements in the modified BVD model now are explicitly related to the physical properties of the QCM and the perturbing mass and fluid in equations (C-45a, b, c, d, f, g). For the bare QCM, ρ_s, ρ and η are zero, hence $L_2 = R_2 = L_3 = 0$, and the modified BVD model in figure 6 reduces to the BVD equivalent circuit for the unloaded QCM, shown in figure 3.

APPENDIX D: Derivation of Equation C-40a, b

The following is a derivation of equation (C-40b).

The $\sin(x)$ and $\cos(x)$ may be expressed as,

$$\sin(x) = \sin(x - n\pi + n\pi) = \sin(x - n\pi)\cos(n\pi) + \cos(x - n\pi)\sin(n\pi)\,, \tag{D-1a}$$

and

$$\cos(x) = \cos(x - n\pi + n\pi) = \cos(x - n\pi)\cos(n\pi) - \sin(x - n\pi)\sin(n\pi)\,. \tag{D-1b}$$

If n is odd, one obtains,

$$\cot(x) = \frac{\cos(x - n\pi)}{\sin(x - n\pi)}\,. \tag{D-2}$$

If x is near $n\pi$, the term $x - n\pi$ is small. Therefore, neglecting the third and higher order terms in the expansion for $\sin(x - n\pi)$, $\cos(x - n\pi)$, equation (D-2) becomes,

$$\cot(x) = \frac{\cos(x - n\pi)}{\sin(x - n\pi)} \approx \frac{1 - \frac{1}{2!}(x - n\pi)^2}{(x - n\pi) - \frac{1}{3!}(x - n\pi)^3} \approx \frac{1}{(x - n\pi)}, \tag{D-3}$$

Multiplying the numerator and denominator on the right side of equation (D-3) by $(x + n\pi)$, one obtains,

$$\cot(x) = \frac{(x + n\pi)}{(x - n\pi)(x + n\pi)} = -\frac{(x + n\pi)}{(n\pi)^2 - x^2}\,. \tag{D-4}$$

Since x is approximated as $n\pi$ and equals to φ, the numerator in equation (D-4) can be approximated as 2φ and equation (D-4) becomes,

$$\cot(\varphi) \approx -\frac{2\varphi}{(n\pi)^2 - \varphi^2}\,, \tag{D-5}$$

Comparing the above two equations (D-4 and 5) under same $n = 1,3,5...$ values, and noting that $x = \varphi = 0.9937n\pi$, one may obtain following table,

n	$-(x + n\pi)/\left[(n\pi)^2 - x^2\right]$	$-2x/\left[(n\pi)^2 - x^2\right]$
1	-50.2066	-50.0469
3	-16.7355	-16.6823
5	-10.0413	-10.0094
7	-7.1724	-7.1496
9	-5.5785	-5.5608

Table D1: Calculation result in equation (D-4) and (D-5).

This table further justifies the equivalence of equations (D-4) and (D-5).

Relative to equation (C-40a), the following results a justification for this equation. The $\sin(x)$ and $\cos(x)$ may be expressed as,

$$\sin(x) = \sin(x - \frac{n\pi}{2} + \frac{n\pi}{2}) = \sin(x - \frac{n\pi}{2})\cos(\frac{n\pi}{2}) - \cos(x - \frac{n\pi}{2})\sin(\frac{n\pi}{2}), \qquad \text{(D-6)}$$

and

$$\cos(x) = \cos(x - \frac{n\pi}{2} - \frac{n\pi}{2}) = \cos(x - \frac{n\pi}{2})\cos(\frac{n\pi}{2}) + \sin(x - \frac{n\pi}{2})\sin(\frac{n\pi}{2}). \qquad \text{(D-7)}$$

Noting that n is an odd, one obtains,

$$\tan(x) = -\frac{\cos\left(x - \frac{n\pi}{2}\right)}{\sin\left(x - \frac{n\pi}{2}\right)}. \qquad \text{(D-8)}$$

Expanding the numerator and denominator of equation (D-8) and neglecting the third and higher order terms, one obtains,

$$\tan(x) \approx -\frac{1-\frac{1}{2!}\left(x-{}^{n\pi}\!/_{2}\right)^2}{\left(x-{}^{n\pi}\!/_{2}\right)-\frac{1}{3!}\left(x-{}^{n\pi}\!/_{2}\right)^3} \approx -\frac{1}{\left(x-{}^{n\pi}\!/_{2}\right)}, \tag{D-9}$$

Multiplying the numerator and denominator at the right side of equation (D-10) by $\left(x+{}^{n\pi}\!/_{2}\right)$, one obtains,

$$\tan(x) = -\frac{\left(x+{}^{n\pi}\!/_{2}\right)}{\left(x-{}^{n\pi}\!/_{2}\right)\left(x+{}^{n\pi}\!/_{2}\right)} = \frac{\left(x+{}^{n\pi}\!/_{2}\right)}{\left({}^{n\pi}\!/_{2}\right)^2-x^2}. \tag{D-10}$$

Letting $x=\frac{\varphi}{2}$, and noting that $x \approx {}^{n\pi}\!/_{2}$, one obtains,

$$\tan(\varphi/2) \approx \frac{4\varphi}{(n\pi)^2-\varphi^2}, \tag{D-11}$$

If one evaluates equations (D-10) and (D-11) as was done for equations (D-4) and (D-5), it may be shown that equation (D-10) and (D-11) yield approximately the same result.

BIOGRAPHY OF THE AUTHOR

Guang Chen was born in Jinan, Shandong Province, the People's Republic of China, on January 18, 1967. After graduation from Shandong Experimental High School in 1984, he enrolled at the North China Electric Power University, Baoding, China, and graduated in 1988 with a Bachelor's degree in Electrical Engineering. He began his graduate study at the University of Maine in January 2000.

Guang Chen is a candidate for the Master of Science degree in Electrical Engineering from The University of Maine in August 2002.